

Studies of Nanocrystalline SnO₂ Doped with Titanium (Ti), Yttrium (Y), and Aluminium (Al)

MSc

J.N. Ntimane

2015

Studies of Nanocrystalline SnO₂ Doped with Titanium (Ti), Yttrium (Y), and Aluminium (Al).

by

James Nduma Ntimane

DISSERTATION

Submitted in (partial) fulfilment of the requirements for the degree of

Master of Science

in

Physics

in the

FACULTY OF SCIENCE AND AGRICULTURE

(School of physical and Mineral Sciences)

at the

UNIVERSITY OF LIMPOPO

Supervisor: Dr T. E Mosuang

Co-Supervisor: Prof K.E Rammutla

2015

DECLARATION

I declare that the dissertation hereby submitted to the University of Limpopo, for the degree of MSc in Physics has not previously been submitted by me for a degree at this or any other university; that it is my work in design and in execution, and that all material contained herein has been duly acknowledged.

Ntimane J. N (Mr)

Date

ACKNOWLEDGMENTS

I wish to express my sincere gratitude to my supervisors, Dr T. E Mosuang and Prof. K. E. Rammutla for their excellent guidance and support during the execution of this research. I would like to thank my numerous friends at the University of Limpopo especially my fellow students. Acknowledgements are also in order for financial assistance received from National Research Foundation. I am grateful to my family for always being there for me. They were a constant source of encouragement and I dedicate this dissertation to my mother, younger brother and my partner.

Abstract

Nanocrystalline materials of defect free anatase and rutile SnO₂ together with Ti and Y in anatase SnO₂ have been modelled successfully using classical molecular dynamics simulations together with Buckingham potential. The structural properties of these SnO₂ phases were analysed using radial distribution functions (RDFs). The effect of increasing temperature in pure SnO₂ and doped SnO₂ were studied. In both pure and doped materials, RDFs suggest phase transition at higher temperature, where anatase SnO₂ transforms to rutile SnO₂. Rutile SnO₂ was found to be more stable than anatase SnO₂. The results showed that the dopants have different effects on the SnO₂ material. Ti defect is found to lower the transformation temperature of anatase to rutile SnO₂. Y defect is found not to have any effect on the anatase to rutile SnO₂ transformation. Thermodynamic properties such as volume thermal expansion coefficient and specific heat capacity were also calculated from above Debye temperature. Volume thermal expansion coefficient was obtained from volume versus temperature curves. Volume thermal expansion coefficient for rutile and Ti-anatase SnO₂ were found to be not of the same order with the calculated results. Specific heat capacity calculated from energy versus temperature curves was found to be in agreement with the Dulong and Petit law of solids.

Nanocrystalline Al/Y co-doped SnO₂ powders were successfully synthesized using the sol-gel method. The samples were subjected to different temperatures 100 (as prepared) 200, 400, 600, 800 and 1000 °C. The effects of co-doping and temperature on the structural and optical properties of Al/Y co-doped SnO₂ nanoparticles as well as morphology were investigated. The characterization techniques used were X-ray powder diffraction (XRD), Raman spectroscopy, Scanning electron microscopy (SEM) and UV-visible spectroscopy (UV-vis). The average particle sizes were found to be in the range between 2.5–8 nm and the strains were calculated to be 2.76–0.53 with increasing temperature for as prepared and the sample sintered at different temperatures. The Raman bands were found to correspond with the literature. At a higher temperature of about 800 °C the materials were found to contain the second phase which is yttrium stannate. However no information about aluminium was found. The optical band gap were found to be between 3.3–3.99 eV in the temperature range 200–1000 °C.

List of Figures

Figure 2.1: The rutile phase of tin dioxide (SnO_2).....	8
Figure 2.2: The anatase phase of tin dioxide (SnO_2).....	9
Figure 2.3: The variation of grain size with calcination temperatures.....	11
Figure 2.4: The structure of a manufactured sensor element	15
Figure 2.5: The reflectance spectra of pure SnO_2	18
Figure 2.6: The transmittance spectra of pure SnO_2	19
Figure 2.7: The absorbance spectra of pure SnO_2	20
Figure 2.8: The refractive index vs wavelength of Y doped SnO_2 films.....	22
Figure 2.9: The extinction coefficient vs wavelength of Y doped SnO_2 films.....	23
Figure 2.10: $(\alpha h\nu)^2$ versus photon energy ($h\nu$) of SnO_2	24
Figure 4.1: The unit cell of crystal structure of anatase SnO_2	38
Figure 4.2: The supercell of crystal structure of anatase SnO_2	39
Figure 4.3: The unit cell of crystal structure of rutile SnO_2	40
Figure 4.4: The supercell of crystal structure of rutile SnO_2	41
Figure 4.5: RDF plots for Sn-Sn, Sn-O, and O-O coordination in anatase SnO_2 at 300 K.....	44
Figure 4.6: RDF plots for Sn-Sn, Sn-O, and O-O coordination in anatase SnO_2 at 3000 K.....	44
Figure 4.7: RDFs plots for Sn-Sn, Sn-O and O-O coordination for rutile SnO_2 at 300 K.....	45
Figure 4.8: RDFs plots for Sn-Sn, Sn-O and O-O coordination for rutile SnO_2 at 3000 K.....	45

Figure 4.9: Volume as a function of temperature for anatase and rutile SnO ₂	49
Figure 4.10: Energy as a function of temperature for anatase and rutile SnO ₂	49
Figure 5.1 (a): RDF of Ti-anatase SnO ₂ at 300 K.....	54
Figure 5.1 (b): RDF of Ti-anatase SnO ₂ at 300 K without O-Ti bond.....	54
Figure 5.2(a): RDF of Ti-anatase SnO ₂ at 3000 K.....	55
Figure 5.2(b): RDF of Ti-anatase SnO ₂ at 3000 K without O-Ti bond.....	55
Figure 5.3: The crystal structure of Ti-anatase SnO ₂ at 300 K.....	57
Figure 5.4: The crystal structure of Ti-anatase SnO ₂ at 3000 K.....	57
Figure 5.5 (a): RDF of Y-anatase SnO ₂ at 300 K.....	58
Figure 5.5 (b): RDF of Y-anatase SnO ₂ at 300 K without O-Y bond.....	58
Figure 5.6 (a): RDF of Y-anatase SnO ₂ at 3000 K.....	59
Figure 5.6 (b): RDF of Y-anatase SnO ₂ at 3000 K without O-Y bond.....	59
Figure 5.7: The crystal structure of Y-anatase SnO ₂ at 300 K.....	61
Figure 5.8: The crystal structure of Y-anatase SnO ₂ at 3000 K.....	61
Figure 5.9: Volume as a function of temperature for Ti-anatase SnO ₂ and Y-anatase SnO ₂	64
Figure 5.10: Energy as a function of temperature for Ti-anatase SnO ₂ and Y-anatase SnO ₂	64
Figure 6.1: The diagram of a usual x-ray powder diffractometer	68
Figure 6.2: Raman events (a) Stokes scattering (b) Anti-stokes scattering.....	70
Figure 6.3: The single monochromator (spectrograph) mode.....	70

Figure 6.4: A diagram of typical Scanning Electron Microscope (SEM)	71
Figure 6.5: A typical sketch of UV-vis spectroscopy.....	73
Figure 6.6: XRD patterns of SnO ₂ nanoparticles sintered at different temperatures..	75
Figure 6.7: XRD profile of the as prepared Al/Y co-doped SnO ₂	76
Figure 6.8: XRD profiles of Al/Y co-doped SnO ₂ at different temperatures.....	77
Figure 6.9: Raman spectra of Al/Y co-doped SnO ₂ at different temperatures.....	81
Figure 6.10: SEM images of Al/Y co-doped SnO ₂ at different temperatures.....	83
Figure 6.11: Absorption spectra of Al/Y co-doped SnO ₂ at different temperatures.....	85

List of Tables

Table 3.1: Schematic of different time – and length-scales, occurring from microscopic to macroscopic dimensions due to recent developments of techniques like Stochastic Rotation Dynamics (SRD) or Lattice Boltzman techniques, which are designed to simulate the mesoscopic scales, there is the potential to combine different methods in a multiscale approach to cover a broad spectrum of times and lengths.....	32
Table 4.1: Lattice parameters and relative sites for anions and cations in anatase and rutile SnO ₂ crystal Structures.....	42
Table 4.2: Buckingham potential parameters used for SnO ₂	42
Table 4.3: The bond-lengths in angstroms (Å) of anatase and rutile SnO ₂ at 300 K.....	46
Table 4.4: The bond-lengths in angstroms (Å) of anatase and rutile SnO ₂ at 3000 K.....	46
Table 4.5: The volume thermal expansion coefficient and specific heat of anatase and rutile SnO ₂	48
Table 5.1: Buckingham potential parameters used for Ti and Y in SnO ₂	52
Table 5.2: The bond-length (Å) of Y-anatase SnO ₂ and Ti-anatase SnO ₂ at 300 K.....	60
Table 5.3: The bond-length (Å) of Y-anatase and Ti-anatase SnO ₂ at 3000 K.....	60
Table 5.4: The values for volume thermal expansion coefficient and specific heat capacity for doped anatase SnO ₂ and undoped SnO ₂	65
Table 6.1: Electromagnetic radiation used in the UV-vis spectroscopy	72
Table 6.2: Lattice parameters of pure and calculated lattice parameters, strain and grain size Al/Y co-doped SnO ₂ annealed at different temperatures.....	79

Table 6.3: The absorption edges and the associated optical energy band gaps
of Al/Y co-doped SnO₂ calcined at different temperatures.....84

Table of contents

Declaration	i
Acknowledgements	ii
Abstract	iii
List of Figures	iv
List of Tables	vii
Chapter 1	1
General introduction	1
1.1 Introduction.....	1
Chapter 2	5
Literature review	5
2.1 Introduction.....	5
2.2 Structural properties of SnO ₂	6
2.3 SnO ₂ for semiconducting devices.....	12
2.4 SnO ₂ for gas sensing.....	13
2.5 The effect of particle size on SnO ₂	16
2.6 Optical properties of SnO ₂	16
Chapter 3	25
Computational method	25
3.1 Introduction.....	25
3.2 Molecular Dynamics.....	26
3.2.1 Boundary condition.....	27
3.2.1.1 Isolated boundary condition.....	27
3.2.1.2 Periodic boundary condition.....	27
3.2.2 Initial condition.....	28
3.2.3 Force calculation.....	28

3.2.4 Integrator.....	29
3.2.4.1 Leapfrog Verlet.....	29
3.2.4.2 Velocity Verlet.....	30
3.2.5 Ensemble.....	30
3.2.6 Property calculations.....	31
3.3 Interatomic potentials.....	33
3.3.1 Buckingham potential.....	33
Chapter 4.....	35
Defect free anatase and rutile SnO₂.....	35
4.1 Introduction.....	35
4.2 Structure of defect free anatase and rutile SnO ₂	37
4.3 Equilibrium properties.....	42
4.4 RDF's analysis for defect free anatase and rutile SnO ₂	43
4.5 Thermodynamic properties.....	47
4.5.1 Volume thermal expansion coefficient of SnO ₂	47
4.5.2 Specific heat capacity of SnO ₂	48
4.6 Conclusion.....	50
Chapter 5.....	51
The role of Ti and Y defects in anatase SnO₂.....	51
5.1 Introduction.....	51
5.2 Equilibrium properties.....	52
5.2.1 RDF's analysis for doped anatase SnO ₂	53
5.2.1.1 Ti-anatase SnO ₂	53
5.2.1.2 Y-anatase SnO ₂	56
5.3 Ti-anatase SnO ₂ and Y-anatase SnO ₂	62
5.4 Thermodynamic properties.....	62
5.4.1 Volume thermal expansion coefficient of doped anatase SnO ₂	63

5.4.2 Specific heat capacity of anatase SnO ₂	63
5.5 Conclusion.....	65
Chapter 6	66
6.1 Introduction.....	66
6.2 Sample Preparations.....	66
6.3 Characterisation Techniques.....	67
6.3.1 X-ray Powder Diffraction (XRPD) Studies.....	67
6.3.2 Raman Spectroscopy Studies.....	69
6.3.3 Scanning Electron Microscopy (SEM) Studies.....	71
6.3.4 UV–vis Spectroscopy Studies.....	72
6.4 Experimental Results.....	74
6.4.1 XRD Results.....	74
6.4.2 Raman Results.....	80
6.4.3 SEM Results.....	82
6.4.4 UV-vis Results.....	82
6.4.4.1 Optical properties.....	82
6.5 Conclusion.....	86
7. References	87
8. Publications and conference presentations	106
8.1 Publications.....	106
8.2 Conference Presentations.....	106

Chapter 1

General Introduction

1.1 Introduction

There is growing interest in nanocrystalline materials because of their unique physical and chemical properties in comparison to their bulk counter parts. Recently the interest in nanocrystalline material has been increased due to the possibility of producing superhard and superplastic ceramics and catalysts [1]. The possible future uses of nanocrystalline materials include: production of hydrogen, removal of pollutants and toxins, medical imaging, bio-tags for gene identification, drug manufacture, protein analysis, flat-panel displays, illumination, optical and infrared lasers and many more [2]. Currently, here in South Africa, nanomaterials are being investigated for future water purification and sensing. The metal-oxide nanocrystalline materials like tin dioxide (SnO_2) are currently of considerable technological interest as they are being used in the chemical, pharmaceutical, ceramic and electronic industries. The material speciality is on dual valency that the tin atom possessed, with tin preferably attaining an oxidation state of 2+ or 4+. This dual valency facilitates a variation of the surface oxygen composition [3]. SnO_2 is a crystalline solid with a tetragonal crystal rutile structure which is known to be stable only at high pressures and temperatures [4].

Under normal conditions SnO_2 crystallizes in tetragonal rutile structure, which belongs to the $p4_2/mnm$ space group. However there are some other phases which were found at higher temperature and pressure experiments ranging from rutile to cotunnite phases [5]. SnO_2 is an n-type semiconductor with a wide band gap of 3.6 eV [6] at room temperature which is characterised by oxygen vacancy. The intrinsic oxygen vacancies (V_o'') are compensated by electrons [7]. Its composition can be represented as $\text{SnO}_{2-\delta}$, where $10^{-5} < \delta < 10^{-3}$ characterizes the deviation from the stoichiometry [8]. Due to the following advantages: high mechanical and chemical stability, low price and stability at high temperatures and pressure and also in acidic and basic environment [9], SnO_2 became the most fascinating material to be explored. It has outstanding technological

applications which are induced by its remarkable properties such as structural, electronic, optical, electrical and chemical properties [10]. Previous studies have shown that the size, morphology and dimensionality of semiconductors have impact on those properties. Significant efforts have been dedicated to the design of nanostructured semiconductor materials in order to improve their performance in optical, sensor, electronic and electrochemical applications [11]. For example, it has been demonstrated that the gas sensitivity of nanocrystalline SnO₂ sensors increases greatly as the size of SnO₂ crystallites decreases below ~10 nm [12]. SnO₂ is known to have many applications and among them, transparent conduction oxides, catalysis and gas sensing were considered to be its main applications [3].

Transparent conducting oxides (TCO) are of great value in infrared reflective coatings and in optical displays such as active matrix liquid crystal displays. The majority of TCOs are n-type conductors such as indium tin oxide, fluorine-doped tin dioxide (SnO₂:F), or ZnO. A typical TCO is tin dioxide [13]. In chemical applications, oxides are used as support materials for dispersed metal catalysts but also often exhibit catalytical activity by themselves. Furthermore, it is becoming increasingly apparent that the active phase of some metal oxidation catalysts is in fact their oxides rather than the pure metal [3]. In the case of gas sensing, this serves as a unique material for gas sensors due to some of its fundamental chemical and physical properties [14] and its high sensitivity is also an advantage [15]. SnO₂ based gas sensors have been synthesized in various forms which include thin films, thick films and pellets [16]. In most cases sensors are used for the detection of various toxic or explosive gases in air. Many studies have shown that even though the material has interesting properties as compared to other semiconducting metal oxides, it also has some draw backs such as low selectivity and grain growth which bring poor performance [17]. Due to these draw backs, there are few studies of pure SnO₂ phases to improve its performance.

Introduction of impurities (transition metal or other metal oxides) to the material is the common way of improving the sensing properties (selectivity, sensitivity, thermal stability and working temperature) of the material [18]. This is achieved by modifying other properties and reducing grain growth at elevated temperatures [14]. Impurities can also create a large number of oxygen vacancies, increase the electrical conductivity and density of SnO₂ [7]. In addition to impurities, finding a proper synthesis method for fabrication of the material with very small particles was another way of enhancing the

performance. The conductivity of the material arises from the oxygen deficient sites and it could be modulated from normal semiconducting to a degenerate one by suitably doping the material and manoeuvring the oxygen deficient sites [19]. Nanocrystalline doped SnO₂ is an interesting subject especially in its gas sensing application to the researchers. Enormous studies carried out on this material show that not all dopants give the desirable applications for example; Padmavathy et al., [20] found that the addition of K and Ni enhance the grain growth. The performance of the dopants depends on their nature such as ionic radius. Dopants can be applied in the form of single or double doped depending on the desirable applications. However there are few studies on double doped than single doped SnO₂.

A broad range of metals and their oxides were tested as dopants in SnO₂. These impurities are generally divided into two groups: 1. Catalytic (Pt, Pd, Ru, Rh) and 2. Electroactive (In, Sb, Cu, Ni, Mn) dopants [6, 21-22]. Catalytic dopants became an interesting subject to many studies. Platinum (Pt) as an example of catalytic was used [23]. It was illustrated that platinum atoms are spread over the SnO₂ surface as clusters of size < 2 nm. It is assumed that the clusters catalyse specific chemical interactions of SnO₂ with gases according to one of two mechanisms, chemical or electronic [14]. The electroactive dopants also lead to a change in the concentration of free charge carriers in SnO₂. It is assumed that dopants metals are distributed in the bulk of SnO₂ grains and occupy tin positions in the crystal structure, with the resulting increase in the electrical resistance of the material due to compensation of intrinsic V_O²⁺ donor defects with M_{Sn}⁻ acceptor doping centers [14]. These materials can be synthesized using chemical and physical methods. In both methods, the production of qualitative materials plays a great role and is influenced by the interatomic interactions and the thermodynamic environment of the material. Various nanocrystalline SnO₂ forms have been synthesized by a number of research groups using various techniques such as spray pyrolysis [24], sol-gel [25], plasma enhanced chemical vapour deposition (PECVD) [26], and magnetron sputtering technique [27, 28]. However, among all these, it was proposed that sol-gel or solution based techniques offer a very high extent of flexibility with simplicity for tailoring crystal size and modifying the system properties. Molecular dynamics (MD) is often used together with these experimental methods to obtain the reliable method of synthesis.

In this study the focus is on exploring the properties of pure SnO₂, single doped SnO₂ (Y -anatase SnO₂, Ti -anatase SnO₂) and co-doped SnO₂ (Al/Y doped SnO₂). Pure SnO₂ and single doped SnO₂ will be studied using computational method (molecular dynamics) where the effects of dopants and temperature on structural properties, stability and phase transformation on the material will be investigated using radial distribution functions (RDFs). Thermodynamic properties (volume thermal expansion coefficient and specific heat capacity) will be calculated using volume versus temperature and energy versus temperature plots. In co-doped SnO₂ experimental method (sol-gel method) will be used to synthesize the material. The analysis will be done using X-ray powder diffraction (XRD), Raman spectroscopy, Scanning Electron Microscopy (SEM), and Ultraviolet-visible spectroscopy (UV-vis) for the effect of dopants and temperature on structural, phase transition and optical properties of SnO₂ material. The remainder of this dissertation is arranged as follows: The following chapter 2 deals with literature review. In the literature review basic structural properties, SnO₂ for semiconducting devices, SnO₂ for gas sensing, the effect of particle size and optical properties of the material are discussed. Computational methods used in this research proceeds the literature review in chapter 3. This is where classical molecular dynamics algorithms and typical potentials used in this research are being described. The results of defect free anatase and rutile SnO₂ and Ti and Y defects in SnO₂ are discussed in chapters 4 and 5, respectively. The results of the experimental studies of Al/Y co-doped SnO₂ are presented in chapter 6.

Chapter 2

Literature Review

2.1 Introduction

Few decades ago nanocrystalline materials such as SnO₂, TiO₂, VO₂, ZnO and InO₃ became the subject of increasing interest to many researchers due to their potential technological applications in many areas of research such as health, energy industry, water and environment. Amongst the family of nanocrystalline materials SnO₂ attracted a great attention due to its outstanding technological applications such as gas sensors, catalytic application, transparent conducting electrodes, liquid crystal displays, etc., [29, 30-33]. These applications are influenced by the unusual characteristics of SnO₂ such as structural, optical, magnetic and electrical properties. SnO₂ is very stable and strong at high temperature and has a very good resistance to strong bases and acid environment at room temperature [34-36]. In addition to these remarkable properties, it also has the ability to combine the low electrical resistance with high transparency in visible range and high reflectivity in infra-red range [3]. Due to this property, SnO₂ became a powerful material for transparent electrodes, anti-corrosion coatings, liquid crystal display and solar cells etc.

Recently many researchers focused much attention on gas sensing because of the following factors: SnO₂ can sense the reducing gases at the parts per million (ppm) level and it can operate at relatively low temperatures [37-38]. It is an inorganic compound and in mineral form is called cassiterite, which occurs naturally. It is known to be the main ore of tin [39]. SnO₂ is colourless and amphoteric and occurs in many forms of phases but much attention is on rutile because of its stability as mentioned above. This material has been studied in various forms ranging from powders [20, 34, 40] to thin films [41-42]. However broader studies have been carried out on this material in the form of thin films because of its useful electrical and optical properties [43-45]. The performance of this material is known to be directly dependent on particle size. In addition to particle size, other factors such as low degree of agglomeration, monogenuous size and homogenous arrangement of particles were also desirable for various

applications [46]. It is known that SnO₂ has some draw backs such as low selectivity and grain growth at higher temperatures which results in poor performance [47]. The addition of impurities and the correct selection of right synthesis methods were proven to be the only ways of enhancing the material performance as mentioned in chapter1. This literature review focuses on structural properties, SnO₂ for semi-conducting devices, SnO₂ for gas sensing, the effect of particle size and optical properties of the material.

2.2 Structural Properties of SnO₂

SnO₂ also known as the stannic oxide crystallises in various forms ranging from the stable rutile to high pressure cotunnite. Specifically under extremes of pressure the transformations is rutile → CaCl₂-type → PbO₂-type → pyrite-type → ZrO₂-type → fluorite-type and lastly cotunnite phase [10, 48-49]. Experiments [50-51] have shown another tetragonal metastable anatase phase and it also found that calculations suggest that the anatase SnO₂ is metastable relative to rutile under all temperatures and pressures, but it transforms spontaneously to rutile at extremely high temperatures [10, 48, 50, 52]. However rutile is known to occur in nature. The tetragonal rutile phase is a degenerate n-type semiconductor with a wide band gap of 3.6 eV. The two phases (rutile and anatase) differ by lattice parameters: the rutile lattice parameters of $a = b = 4.737 \text{ \AA}$ and $c = 3.186 \text{ \AA}$. Furthermore literature showed that both experimental conditions [5, 48] and theoretical predictions [53-54] of rutile tin dioxides have two Sn cations at positions $2a: (000)$ and $(\frac{1}{2}\frac{1}{2}\frac{1}{2})$, and the six O anions at positions $4f_{\pm} (u, u, 0; \frac{1}{2} + u, \frac{1}{2} - u, \frac{1}{2})$ with $u = 0.3056$ [55] at ambient conditions whilst the anatase SnO₂ has lattice parameters of $a = b = 2.832 \text{ \AA}$ and $c = 7.114 \text{ \AA}$ [10,48,50]. Both the rutile and anatase SnO₂ are in such a way that Sn⁴⁺ ion has six O²⁻ ions coordination, and the O²⁻ ion has three Sn⁴⁺ ions coordination. The difference is brought by the fact that in rutile the Sn-O octahedral shares two edges with other octahedrons whereas in anatase the Sn-O octahedral share four edges with other octahedrons. This results in rutile having the space group no.136; D_{4h}^{14} ; $P4_2/mnm$ [56] and anatase the space group no. 141; D_{4h}^{19} ; $I4_1/amd$ [56]. The illustrations are shown in the figures 2.1 and 2.2. The structures consist of tin (Sn) and oxygen (O) atoms. Tin atoms are associated with grey atoms and Oxygen atoms are associated with red atoms. In addition to the above mentioned phases of SnO₂, other phases were found. Rai [57] recently studied the structural

properties of Zn-Cu doped tetragonal perovskite type SnO₂ and discovered that substitution of ZnO and CuO dopants altered the structure of SnO₂ material. In addition to the structural changes, the new phase, orthorhombic with lattice constant $a = 23.5237 \text{ \AA}$, $b = 8.2183 \text{ \AA}$ and $c = 5.1803 \text{ \AA}$ or $a = 21.8594 \text{ \AA}$, $b = 5.3200 \text{ \AA}$ and $c = 5.1803 \text{ \AA}$ respectively were found. Some of the results, similar to the findings of Rai [57] were obtained by Keekenler et al., [41] where the effect of 7 at %Y investigated. Cubic phase of SnO₂ was found from boron doped SnO₂ at different dopants concentrations (1 at %B, 3 at %B, 5 at %B and 7 at %B) and Y doped SnO₂ at (1 at %Y, 3 at %Y, 5 at %Y). Other researchers [58, 5] found the cubic phase of SnO₂ under high pressure. However, recently hetero-phase structures (cubic, orthorhombic, tetragonal rutile crystal) were found from experimental studies based on the solutions carried out at atmospheric pressure [41, 59-61]. Another phase which is columbite SnO₂ (C-SnO₂) phase is not included in the sequence, but it belongs to the orthorhombic space group Pbcn with lattice parameters of $a = 4.714 \text{ \AA}$, $b = 5.727 \text{ \AA}$ and $c = 5.214 \text{ \AA}$ which is similar to the α -PbO₂ structure [62] and was found in higher pressure experiments [63-65] of SnO₂ powder. However, several researchers did show that C-SnO₂ can be produced through a variety of low pressure routes [66-69]. It has been considered an unstable intermediate phase in the transition from disordered SnO₂ to crystalline rutile SnO₂ [68-70]. The fluorite and pyrite-type structures of SnO₂ take place in different oxygen atomic positions [71]. In the fluorite-type oxygen atoms are located at $u = 0.25$ in the 8c Wyckoff positions with space group Fm-3m whereas in pyrite-type oxygen atoms are located at $u = 0.35$ in the 8c Wyckoff position with space group Pa-3 [71]. However many researchers concentrated much on rutile SnO₂ due to its stability in higher temperature and acidic environments as it has been mentioned above. Solid state physics emphasizes that applying heat treatment to the material may cause changes to its crystal geometry and electronic structure [72-73]. Increasing the heat, increases the oscillation frequency of lattice atoms and forces them to change their displacements. This results in distortions in the crystal structure of the material. Distortions as a result of increasing temperature weaken the bonds and alter both electronic properties and geometry of the crystal structure [42]. Moreover many researchers reported that temperature has a significant effect on the stability of the material in terms of particle growth.

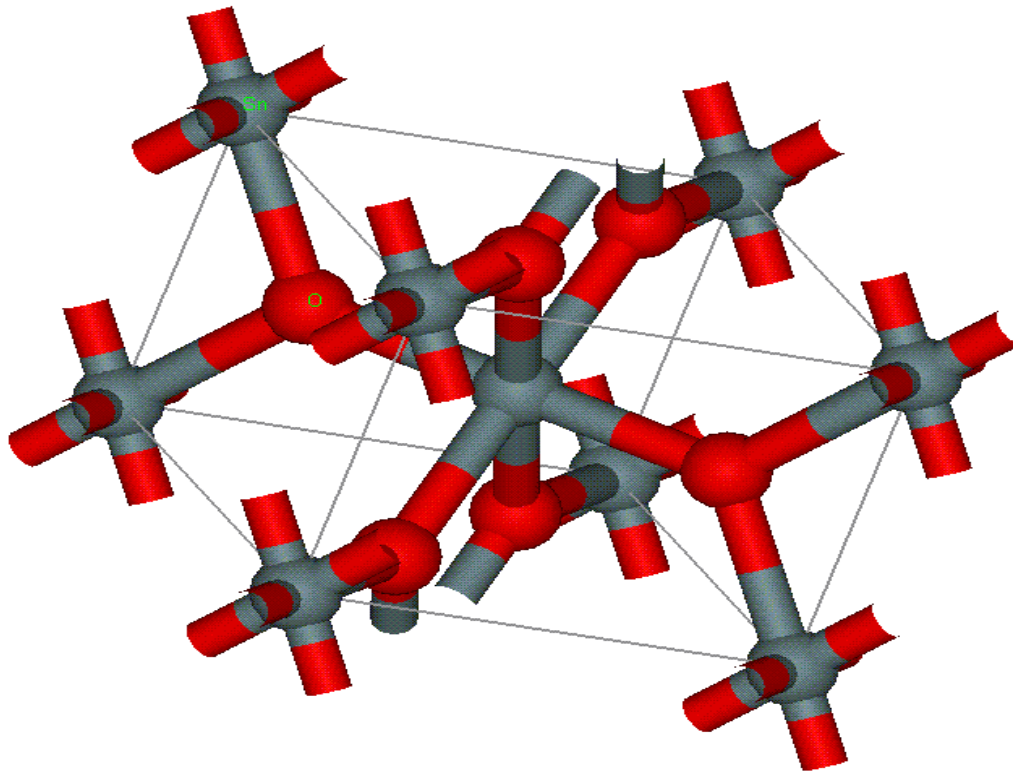


Figure 2.1: The rutile phase of tin dioxide (SnO₂).

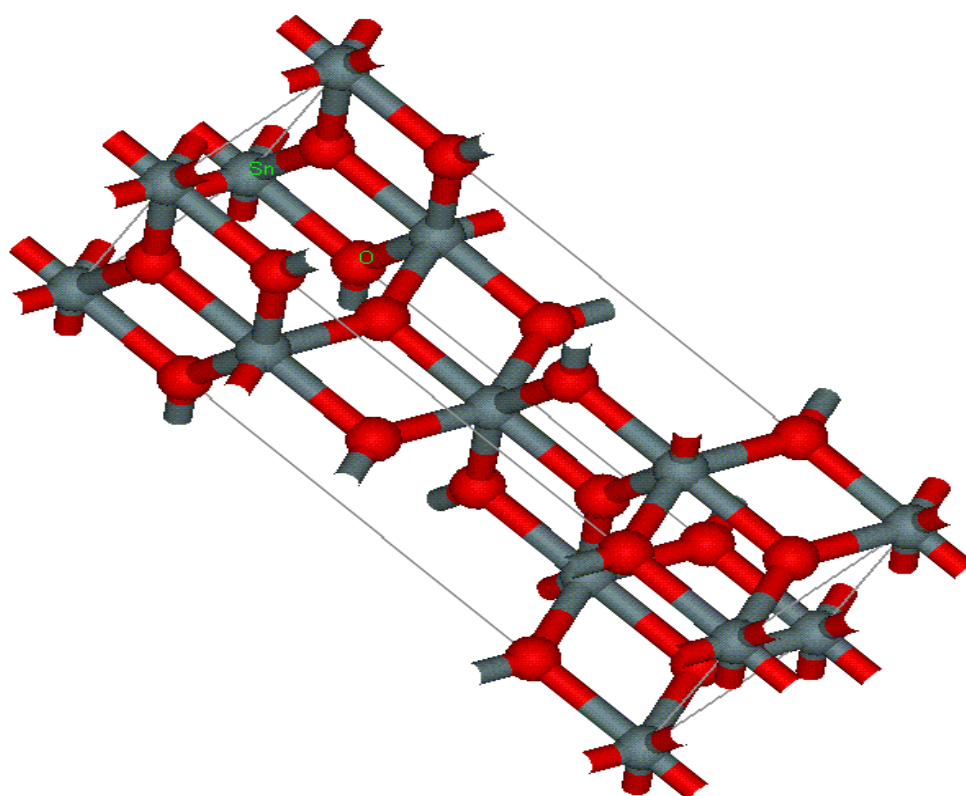


Figure 2.2: The anatase phase of tin dioxide (SnO₂).

Mishra et al., [74] investigated the effect of temperature on SnO₂ thin films and found that the best crystalline structure films can be obtained at higher temperatures. However, higher temperatures result in larger grain size. In addition to larger grain size, the good structural quality surface, the phase transition from anatase to rutile occurred at higher temperatures [10, 48, 50, 52, 75]. Karshoğlu et al., [75] investigated the effect of substrate temperature and deposition time on SnO₂ thin films and also observed the increase in grain size, porosity of the films and coating thickness when the substrate temperature and deposition time increased. However increasing temperature was observed to have more effect than deposition time and also influence the transition from SnO to orthorhombic SnO₂ at the temperature of about 600 °C [4, 75]. It is also known that temperature governs the degree of interaction between the dopants and the host which results in morphology changes and bond-length variation [76]. The effect of temperature in particle growth was minimized by adding some impurities to the material. Finally the effect of temperature on the crystal structure of the material can be analyzed by many techniques including X-ray diffraction (XRD), Scanning Electron Microscope (SEM), Transmission Electron Microscope (TEM), Atomic Force Microscopy (AFM), Radial Distribution Function (RDF) and many more. Figure 2.3 shows the variation of grain size with calcination temperature.

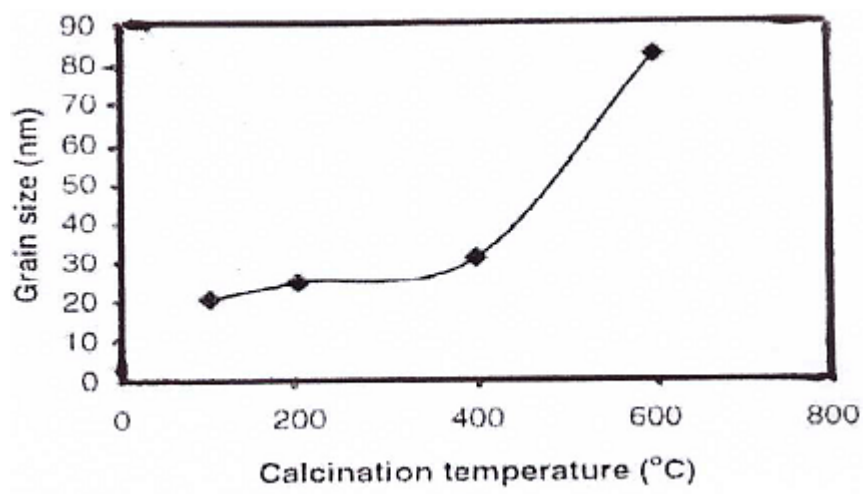


Figure 2.3: The variation of grain size with calcination temperature (°C) [74].

2.3 SnO₂ for Semiconducting Devices

As a direct band gap semiconductor, SnO₂ is a promising material for applications in short-wavelength light-emitting diode and laser diode due to its large band gap of 3.6 eV and high exciton binding energy of 130 meV at room temperature [1, 10, 48, 50]. The undoped SnO₂ thin film shows n-type conduction due to native oxygen vacancy defects. Experimentally, the p-type SnO₂ has been obtained by doping with some transition metals [48, 52, 79]. Doping has been widely studied to alter the properties of nanocrystals in desirable and controllable ways. Dopants can strongly influence electronic behavior of bulk semiconductor. The addition of impurity with one more valence electron than the host atom donates extra electron to the semiconductor (n-type doping) greatly increasing the conductivity of the intrinsic semiconductor [22]. In this sense, the development of doped nanocrystalline materials is critical for many materials. Defect solid state theory [1, 10, 16, 48, 50-52, 77-81] also emphasises how the role of defects can affect the properties of materials electronically, mechanically and chemically.

In most cases dopants were introduced in the material to improve its performance by modifying the properties of the material and lower the grain growth at elevated temperature. Dopants are introduced by reduction of oxygen or adding impurities into the materials. Dopants can be introduced in the form of single doped or double doped on the material depending on the desirable applications. However there are few studies on double doped than single doped. When the dopants are added into the material they follow two of these possible positions, substitutional or interstitial positions, in the material lattice [40]. The doping of the SnO₂ occurs by replacing Sn⁴⁺ and O²⁻ atoms with dopants [42]. The efficiency of dopants was proved to be dependent on the difference between the ionic radius of the dopants and the host atoms [82]. Theoretically, it has been found that the effective substitution of Sn⁴⁺ or O²⁻ by $\mu^{\alpha+}$ ($\alpha > 4$) and β^- elements increases the n-type conductivity [83-85]. But the substitutions of Sn⁴⁺ by $\gamma^{\Theta+}$ ($\Theta < 4$) elements can reduce n-type conductivity and induce p-type conductivity [86-88]. This process leads to trapping of free electrons at the same time eliminating free electrons. The following μ , β and γ represent possible defect atoms and α and Θ represent the possible oxidation states. When applied into a powder, they follow different path: form a new crystallographic structure or solid solution, migrate to the surface (surface additives), or nucleate to a second phase and diffuse into bulk of the

particle [89]. It is reported that the draw backs of pure SnO₂ were minimised by the introduction of dopants in the material [7] and in addition to minimization of draw backs, some physical properties such as electrical conductivity and density of the material are enhanced [90,168]. However the introduction of dopants gives the desirable and undesirable properties. For example, Ravichandran et al., [91] recently reported that Sb and F co-doping SnO₂ were found to influence the grain growth but reduced the electrical resistivity of the material, meaning applications that depend on specific surface area of the material would suffer. The substitution of Sn ions by copper or titanium ions created more oxygen vacancies in the material [7, 40] which improves the sensitivity of the material. The dopants of which their ionic radii were close to the ionic radius of the host material (SnO₂) were found to have more effect on the performance as compared to the one having higher ionic radius. For example dopants such as Al, Ti, Cu [7, 40, 92] were found to have more influence than Y due to their difference in ionic radii [89].

2.4 SnO₂ for Gas Sensing

The major applications of gas sensors are for domestic or industrial security, environmental and emission monitoring, medical and agribusiness controls, etc. The gas sensors for hydrogen are useful to leak detection in domestic appliances and industries, especially electric power station and substations. It has been reported that SnO₂ is one of the good hydrogen sensor and is also used for detecting flammable gases such as CH₄, C₃H₈ and C₄H₁₀ [50, 81] and some sensors are used to monitor toxic gases (CO, H₂S, etc.) indoor and outdoor places [93-95]. Nanocrystalline SnO₂ based gas sensors have been synthesised in various forms such as thin or thick films and pellets [4, 52, 77]. This material has shown outstanding performance in comparison to its family of semiconducting oxides such as TiO₂ and ZnO due to its ability to operate at low temperature and high sensitivity and some of its basic chemical and physical properties [96-97]. Since the first commercially available catalytic elements were developed in 1950s, the gas detection sensors have been studied by several investigators [16, 52, 77-78, 80-81]. However it was found to have some draw backs such as low selectivity and high-energy consumption that prevent its use in more sophisticated applications [17]. One of the common ways to tune the sensitivity and selectivity of the material and to reduce the consumption of energy is by introducing

impurities (normally transition metals or other oxides) to the material, which were well known to have effects on the properties of SnO₂ surface. The main advantages of using SnO₂ in gas sensing devices are because of its low cost, easy to synthesise and high sensitivity [15]. Recently high sensitivity and selective detection of various gases has become significant for the emission and environmental control. Due to its high sensitivity, SnO₂ became the material of choice for the detection of combustible and noxious gases in air [98]. Two main mechanisms are responsible for gas sensing; (1) the bulk diffusion of oxygen from outside into the oxides; (2) the low-temperature chemisorptions of environmental gases on the surface of multiple grains, charging in the surface state and charge distribution inside the grain [58]. The sensitivity is defined as the ratio of sensor resistance in air (R_a) to the sensed gas containing air (R_g) [99]

$$S = \frac{R_a}{R_g}, \quad (2.1)$$

where S is the sensitivity, R_a is the resistance of the material, R_g is the resistance of sensed gas. In addition to introducing dopants to improve gas sensitivity and reduce the operating temperature, previous studies have given their efforts to the development of the new materials and fabrication process, the addition of various catalysts, the control of grain size, pore and surface defects [51-52, 77]. When the particle sizes were controlled to a size between 8–10 nm, SnO₂ material was found to be more effective for fast response and recovery [100] and also increase the surface area of the material. Singh et al., [34] investigated pure SnO₂ based gas sensor and found that it can sense the ethanol vapours at the maximum temperature of about 250 °C due to small particle size without dopants. Figure 2.4 show the typical structure of the fabricated sensor element used to measure the gas sensitivity of SnO₂ material.

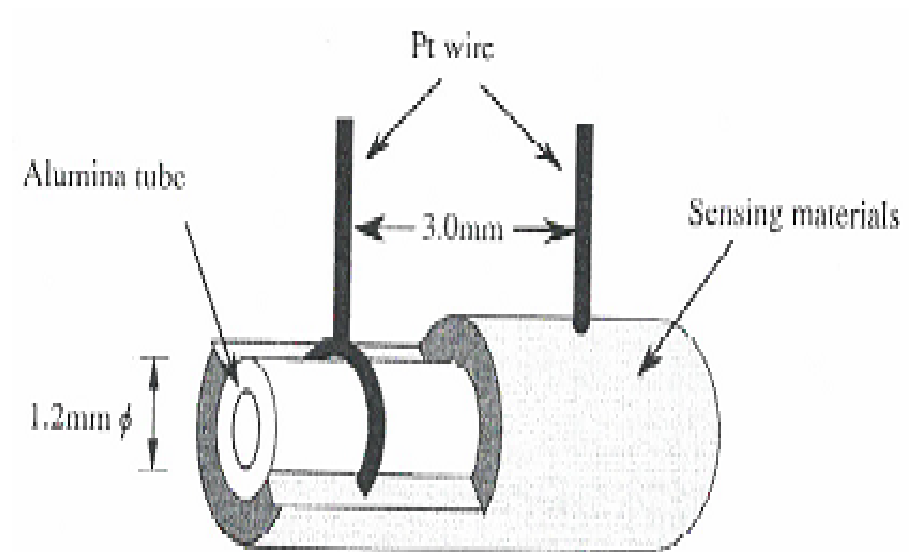


Figure 2.4: The structure of a manufactured sensor element [99].

2.5 The effect of particle size on SnO₂

Since it was found that the performance of the material is related to particle size and compositional characteristics [101-102], it is a challenge to many researchers to produce the material whose particles are on nano-scale. Lu et al., [100] studied the effect of particle size and found that the sensitivity is inversely proportional to particle size. In addition, the particle size of 8-10 nm is desirable for fast response and recovery and it also reduces the operating temperature [100]. The ability to produce the particles that are small in size and nano-sized elements alters the material properties such as electrical conductivity, refractive index, band gap, magnetic properties, strength and others [103-104]. Zhang et al., [40] studied the dependence of the energy barrier on particle size and found that when a particle is reduced to nanometers, it has more effect on energy barrier. The findings of Lu et al., [100] and Zhang et al., [40] combined showed that energy barriers have an influence on the sensitivity, because both depend on particle size. Since it is known that particle sizes have an influence on the energy barrier, it can be concluded that they have indirect influence on the temperature dependence of conductivity of a semiconductor which can be approximated by the Arrhenius equation [105]

$$\sigma = \sigma_0 \exp\left(\frac{-eV_s}{kT}\right), \quad (2.2)$$

where σ_0 is a factor that includes the bulk intragranular conductance, k the Boltzmann's constant, T the absolute temperature and $-eV_s$ the potential energy barrier at the interface between two neighbouring particles.

$$eV_s = \frac{e^2 N_t^2}{2\epsilon_r \epsilon_0 N_d}, \quad (2.3)$$

where N_t is the surface density of adsorbed oxygen ions (O_2^- or O^-), $\epsilon_r \epsilon_0$ the permittivity of the semiconductor and N_d the volumetric density of the electron donor.

2.6 Optical Properties of SnO₂.

Due to its high transparency in visible light and near infra-red region, intense research has been focused on exploring the optical properties of the undoped and doped SnO₂ thin films. The optical properties of SnO₂ material are normally analyzed by Ultra Violet-visible (UV-vis) absorption spectroscopy techniques as well as photoluminescence

techniques. The attributes of optical properties such as transmittance, absorbance, reflectance and optical band gap made this material to have interesting optical technologies. Some of these attributes of optical properties such as reflectance were obtained from the following equation.

$$R + T + A = 1, \quad (2.4)$$

where R, T and A are reflectance, transmittance and absorbance of the material respectively. Figures 2.5, 2.6 and 2.7 show the typical example of reflectance transmittance and absorbance of pure SnO₂, respectively. Serin et al., [106] reported that the value of transmittance in the visible region of undoped SnO₂ were found in the range of 75-95% in the region of 400-1100 nm wavelengths. The material was subjected to the temperatures between 300 and 500 °C. However, others [107] found the transmittance value ranging at 82-94% in the area of 254 to 1400 nm wavelengths between 400 and 500 °C. The above findings reflect that increasing temperature is directly proportional to transmittance. For fluorine doped SnO₂ the values of transmittance were found to vary from 60 to 87% in the area of 200 to 850 nm wavelengths between 450 to 525 °C [108].

Refractive index (n) of the samples is divided into two parts: the real part and the imaginary part. The real part is associated with the reflectance of the film, where n value is a dependence of wavelength and can be obtain by using the relation [109].

$$R = \frac{(n-1)^2}{(n+1)^2}, \quad (2.5)$$

where R is reflectance and n refractive index. Saikia et al., [107] calculated refractive index of pure SnO₂ and found the values to be varied from 1.6 to 3.6 which were in agreement with the findings of Chopra et al., [29]. However the small variation of the value was because of the increase in the reflectance with the film thickness. Keskenler et al., [41] studied the refractive index for B and Y doped SnO₂ in different dopant percentages (1 at %B, 3 at %B, 5 at %B, 7 at %B) and (1 at %Y, 3 at %Y, 5 at %Y, 7 at %Y), respectively, and obtained the average values to be within the range of Saikia et al., [107] findings. In addition, these values were found to be in agreement with the values reported by other researchers [110-112].

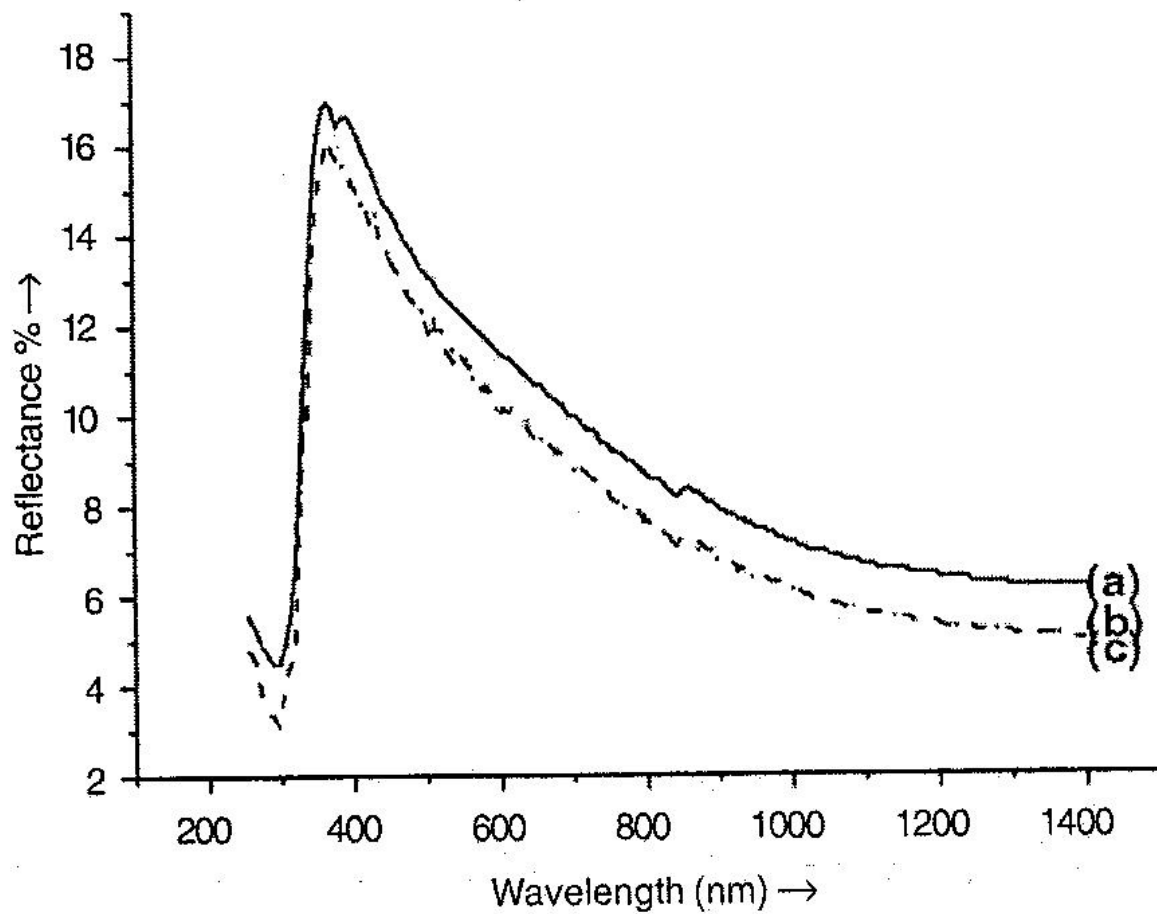


Figure 2.5: The reflectance spectra of pure SnO₂ [107].

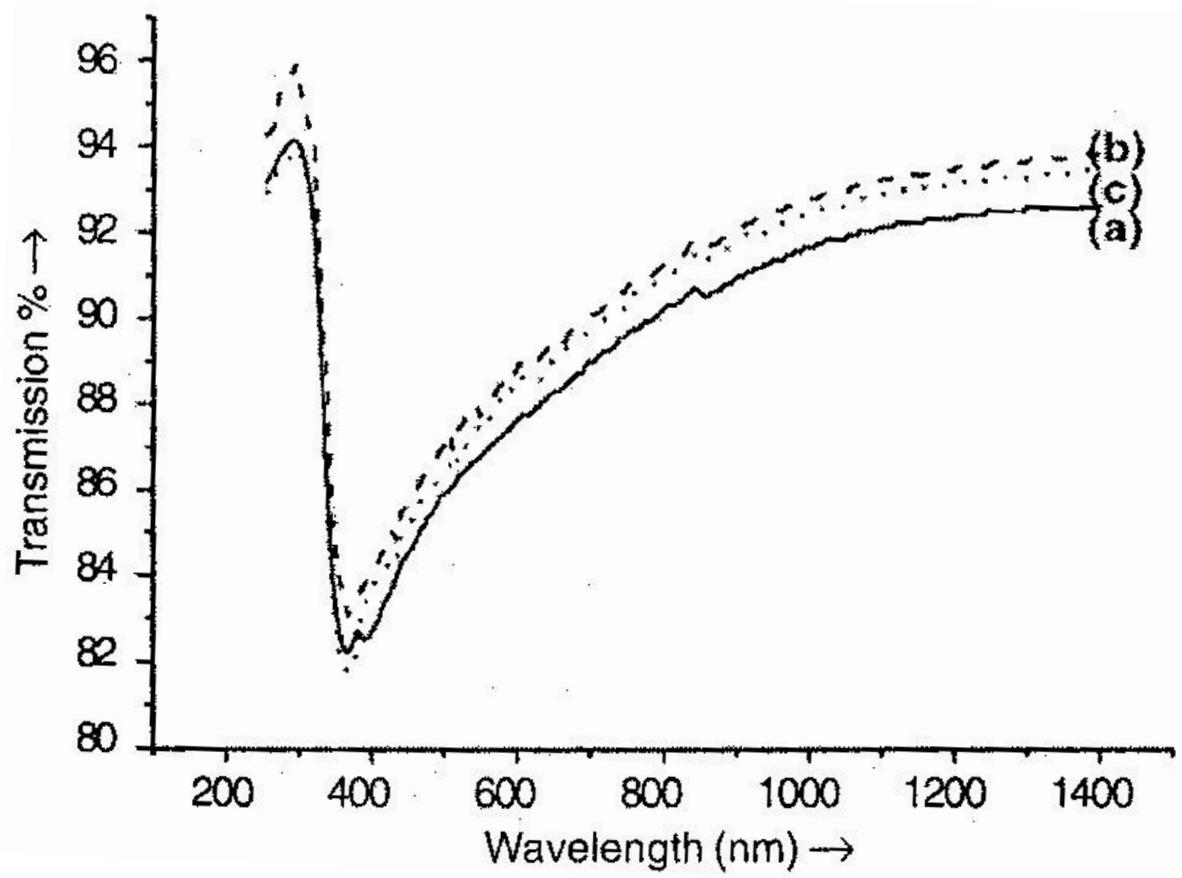


Figure 2.6: The transmittance spectra of pure SnO₂ [107].

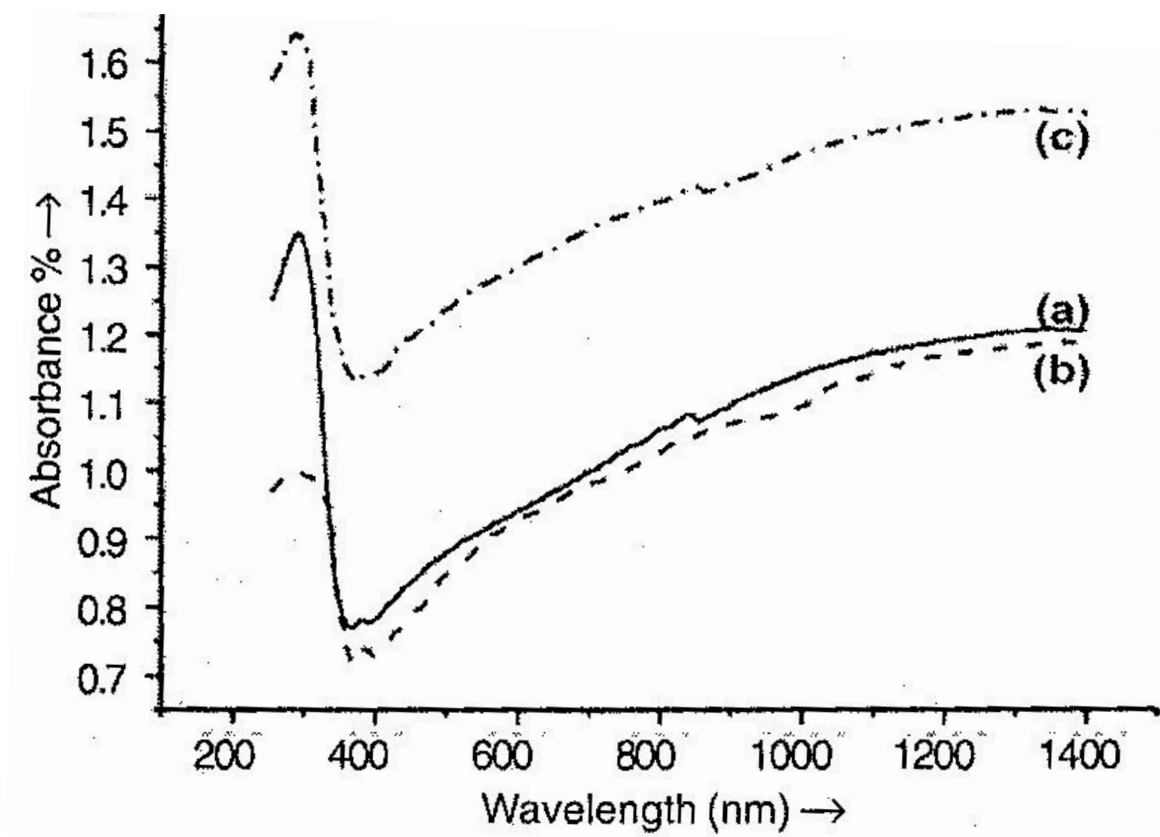


Figure 2.7: The absorbance spectra of pure SnO₂ [107].

The imaginary part of the refractive index, which is called extinction coefficient (k), is directly associated with the absorption coefficient and were calculated by relation [113]

$$\alpha = \frac{4\pi K}{\lambda}, \quad (2.6)$$

where α is absorption coefficient and λ is wavelength. From the literature it can be seen that dopants and temperature have an influence in reflectance of the material which led to an increase in refractive index. Figures 2.8 and 2.9 show the typical refractive index and extinction coefficient of Y doped SnO₂ with different dopants concentration [41]. The optical absorption coefficient α near the absorption edge for direct inter band transitions is given by the equation [114]

$$\alpha = \frac{B (hv - E_g)^{1/2}}{hv}, \quad (2.7)$$

where hv is the incident photon energy, α absorption coefficient, E_g the energy band gap and B is the characteristics parameter. It can also be calculated from transmittance (T) values at the absorption edge from the Lambert's Law [106]

$$\alpha = \ln (1/T)/t, \quad (2.8)$$

where t is the film thickness and T is the transmittance. Figure 2.10 shows the typical graph between $(\alpha hv)^2$ against hv in the visible region. The optical band gap E_g in a semiconductor was determined by extrapolating the linear portion of the respective curve to $(\alpha hv)^2 = 0$ from the plot of $(\alpha hv)^2$ vs hv , where n represent the nature of transformation. For pure SnO₂, the following values were reported 3.94-3.96 eV [106], 4.1-3.8 eV [46]. Keskenler et al., [41] studied the band gaps of B and Y doped SnO₂ and obtained 4.02-3.97 and 4.01-3.96 eV respectively. Yadav et al., [108] investigated the fluorine doped SnO₂ film and found the band gap to be 4.15 eV. Lastly for co-doping of SnO₂ band gap was reported to be very small (3.55 eV) [91] as compared to pure and single doped. From the literature it seems that the band gap decreases with the increasing temperature and also when the dopants concentration increases [41, 46].

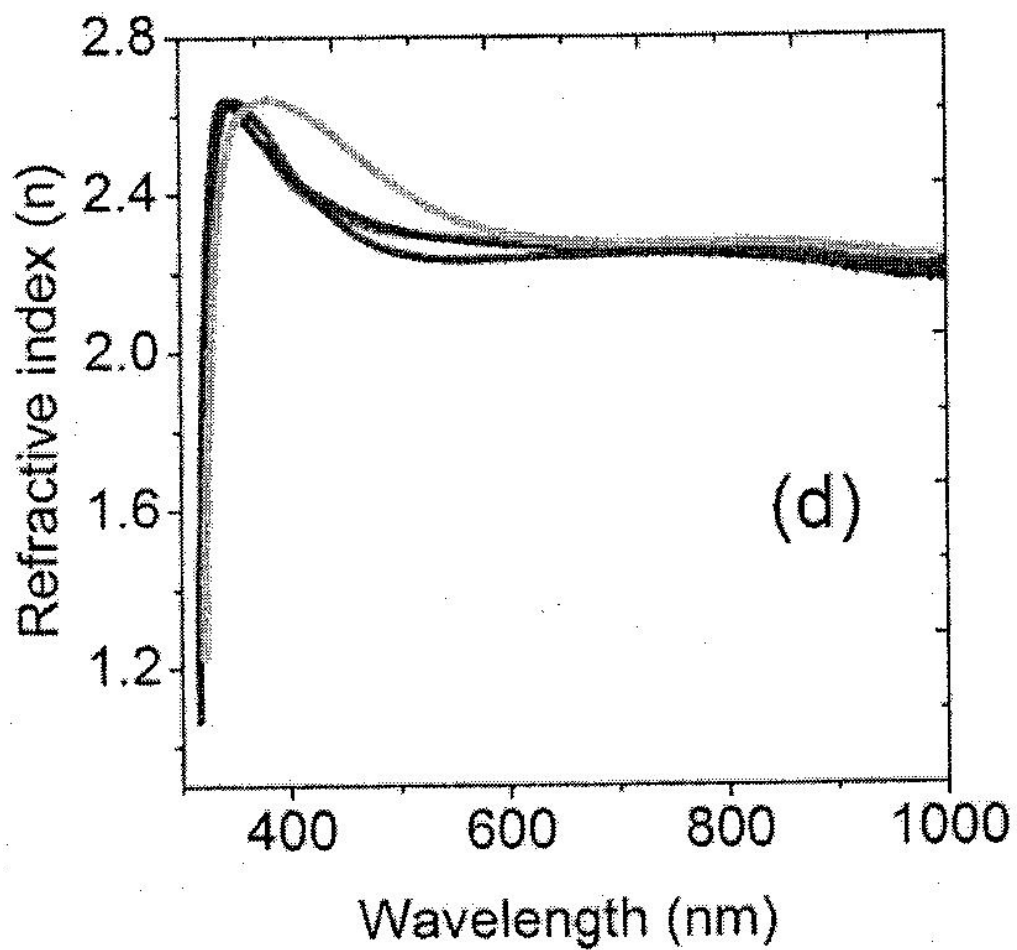


Figure 2.8: The refractive index vs. wavelength of Y doped SnO₂ films [41].

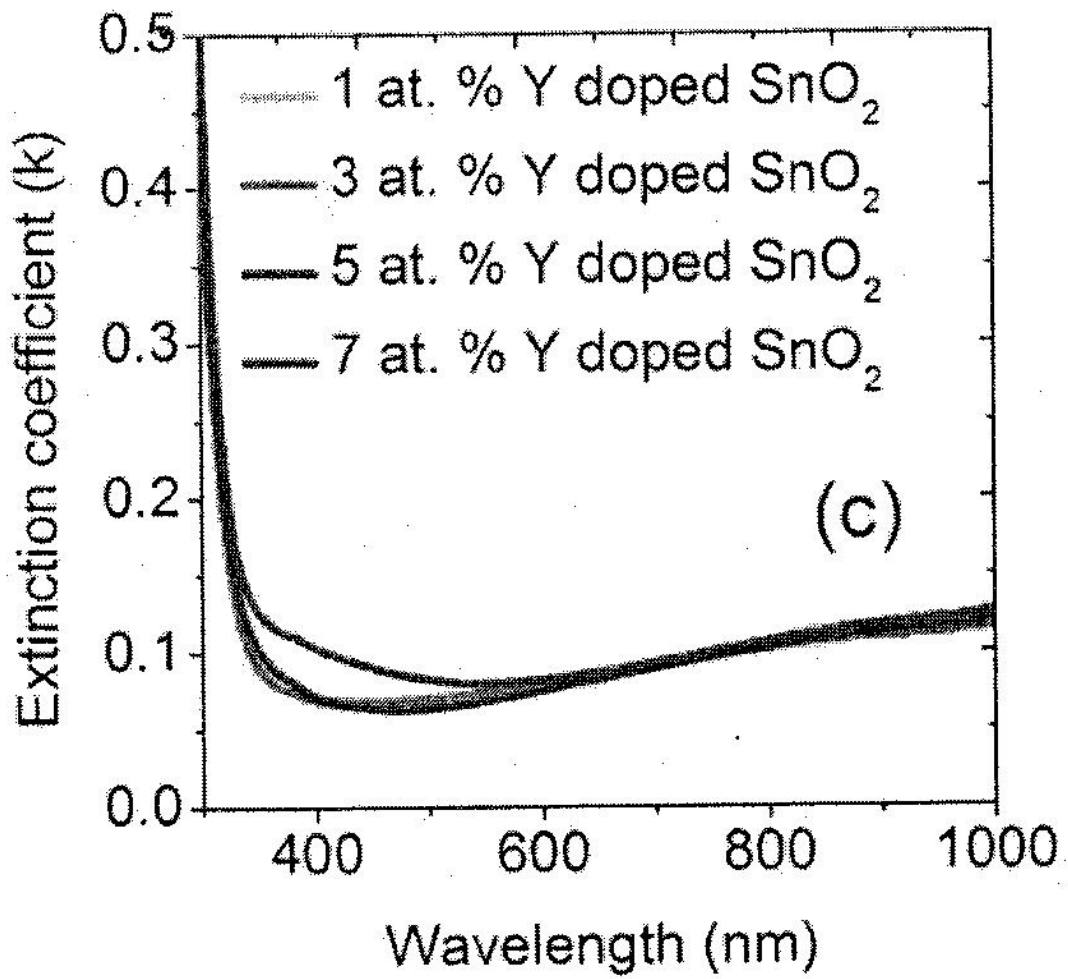


Figure 2.9: The extinction coefficient vs wavelengths of Y doped SnO₂ films [41].

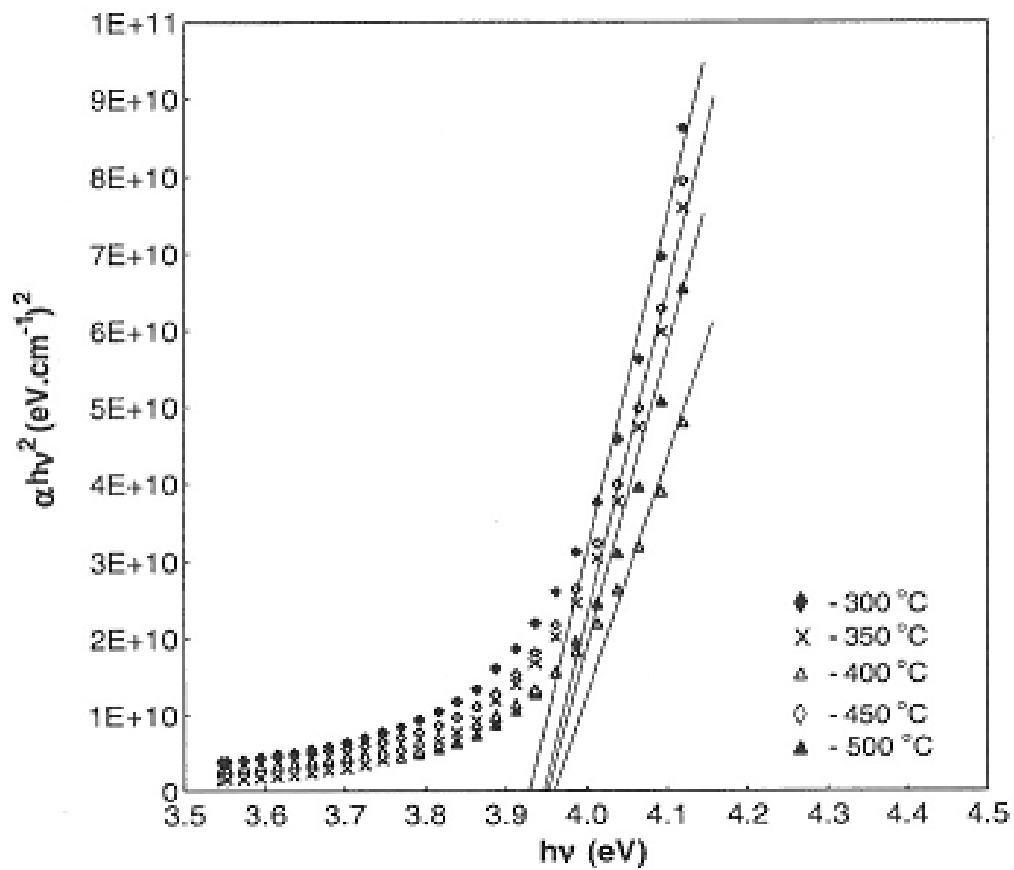


Figure 2.10: $(\alpha hv)^2$ versus photon energy(hv) of SnO₂ [106].

Chapter 3

Computational Methodology

3.1 Introduction

Computer simulation is just a branch of computational physics and chemistry in which a mathematical model of the real world is formulated and its consequences for the various physical and chemical quantities are evaluated by numerical methods [115]. Researchers carry out computer simulations in the hope of understanding the properties of assemblies of molecules in terms of their structure and the microscopic interactions between them [116]. Computer simulation is a powerful and modern tool for studying macroscopic systems by implementing microscopic models [117]. The microscopic model is specified in terms of the molecular structure and intermolecular interactions. One of the aims of computer simulation is to reproduce experiment to explain in full the invisible microscopic details and further explain experiments. On the other hand, simulation can also be used as a useful predictive tool. Results from computer simulations are compared with analytical predictions and experimental data to test the accuracy of the model [117]. So computer simulations provide a good test for theory. Moreover, they are used to test complex models that cannot be worked out analytically [117]. They are also used to study systems that are not accessible experimentally, and they help one to understand experiments on a microscopic level. In this research project, computer simulations are used to predict the properties of materials. These predictions are subject to limitations imposed by the computer (such as computer memory, speed and precision). With faster and more powerful computers, larger and more complex system may be explored using computer simulations [118]. The field of computer simulations has developed into a very important branch of science, which on one hand helps theorists and experimentalists to go beyond their inherent limitations and on the other hand is a scientific field on its own [119]. Therefore, simulation science has often been called the third pillar of science, complementing theory and experiment [119]. The important advantage of computer simulation is the ability to expand the

horizon of the complexity that separate solvable from unsolvable problems [118]. The traditional simulation methods for two-body or many-body systems can be divided into two classes, i.e. stochastic and deterministic simulations, which are largely represented by the Monte Carlo (MC) methods [120,127] and the molecular dynamics (MD) methods [121,122], respectively. These simulation methods have become a powerful tool in solving various number of body system problems in statistical physics [123], physical chemistry [124] and biophysics [125]. The most widely used simulation method for molecular systems is molecular dynamics (MD). The advantage of MD over a typical stochastic simulation is that MD can give all the information on the time dependence of the system, which is necessary for analysing the structures and dynamical properties of the system [126]. In this study Molecular dynamics will be used together with empirical Buckingham potential.

3.2 Molecular Dynamics

Molecular dynamics (MD) is the most detailed computer simulation technique for investigating the physical movements of atoms and molecules. MD methods are governed by the system's Newton's law and consequently Newton's equations of motion are integrated to move particles to new positions.

$$\vec{F} = m\vec{a}, \quad \vec{F} = -\frac{dU}{dx}, \quad (3.1)$$

where F is the resultant force, m is the mass of the particle, a is the acceleration of the particles and $-\frac{dU}{dx}$ is the potential energy. This is an advantage of MD simulations with respect to MC, since not only the configuration space is probed but the whole phase space which gives additional information about the dynamics of the system. Both methods are complementary in nature but they lead to the same averages of static quantities, given that the system under consideration is ergodic and the same statistical ensemble is used [119]. In order to characterise a given system and to simulate its complex behaviour, a model for interactions between system constituents is required. This model has to be tested against experimental results, i.e. it should reproduce or approximate experimental findings like distribution functions or phase diagrams, and theoretical constraints, i.e. it should obey certain fundamental or limiting laws like energy or momentum conservation. Molecular dynamics is a specialized discipline of

molecular modelling and computer simulation based on statistical mechanics and it is also frequently used in the study of proteins and biomolecules, as well as in material science [127]. It allows detailed time and space resolution into representative behaviour in phase space for carefully selected systems. It probes the relation between molecules structure, movement and function. It is typically applied to small systems containing thousands of particles, it is a multidisciplinary method. It employs algorithms from computer science and information theory. MD is used to examine the dynamics of atomic-level phenomena that cannot be observed directly, such as thin film, growth and ion-sub plantation [127]. There are five key ingredients to an MD simulation, which are boundary conditions, initial conditions, force calculations, intergrator, ensemble, and property calculation [128]. Overview of each is given below in the next sections.

3.2.1 Boundary condition

The choice of boundary conditions affects the properties of the sample system. There are two major types of boundary conditions: isolated boundary condition (IBC) and periodic boundary condition (PBC). IBC is perfectly appropriate for studying clusters and molecules, while PBC is appropriate for studying bulk liquids and solids.

3.2.1.1 Isolated boudary condition

In IBC, the particle system is surrounded by vacuum; these particles interact among themselves, but are presumed to be far away from everything else in the universe that no interactions with the outside occur except perhaps responding to some well-defined “external force”.

3.2.1.2 Periodic boundary condition

PBC are implemented to imitate the infinite bulk surrounding the system, the sample and so remove surface effects [117]. It is assumed that the system is surrounded by an infinite number of identical copies. When particles leave the cell, their images simultaneously enter the cell through the opposite face. Particles near the boundary of the simulation box interact with periodic images across the boundary. Periodic boundary

conditions are used in the presence of an external potential only if this potential has the same periodicity as the simulation box [129].

3.2.2 Initial condition

The initial particle positions and velocities must be chosen so that there is no noticeable overlap of atomic core. Since Newton's equations of motion are second-order ordinary differential equations (ODE), initial condition (IC) basically means $x^{3N}(t = 0)$ and $\dot{X}^{3N}(t = 0)$, the initial particle positions and velocities. Generating the IC for crystalline solids is usually quite easy, but IC for liquids needs some work, and even more so for amorphous solids. A frequent cause of MD simulation breakdown is pathological initial condition, as the atoms are too close to each other initially, leading to huge forces.

3.2.3 Force calculation

Before moving into the details of force calculation, two approximations should be considered under the use of the classical equation of motion

$$m_i \frac{d^2 x_{i(t)}}{dt^2} = f_i \equiv - \frac{\partial u}{\partial x_i}, \quad i = 1, \dots, N \quad (3.2)$$

to describe the atoms. The first is the Born-Oppenheimer approximation [130] which assumes the electronic state couples adiabatically to nuclei motion. The second is that the nucleus motion is far removed from the Heisenberg's uncertainty lower bound: $\Delta E \Delta t \gg h/2$. If we plug in $\Delta E = k_B T/2$, kinetic energy, and $\Delta t = 1/\omega$, where ω is a characteristic vibrational frequency, we obtain $k_B T \gg h\omega/2$. In solids, this means the temperature should be significantly greater than the Debye temperature, which is actually quite a stringent requirement. Large deviations from experimental heat capacities are seen in classical MD simulations of crystalline solids [131]. A variety of schemes exist to correct this error [129], for instance the Wigner-Kirkwood expansion [132] and path integral molecular dynamics [133]. The evolution of the right-hand side of equation (3.2) is the key step that usually consumes most of the computational time in a MD simulation, so its efficiency is crucial. For long-range Coulomb interactions, special algorithms exist to break them up into two contributions: a short-ranged interaction, plus

a smooth, field-like interaction, both of which can be computed efficiently in separate ways [125].

3.2.4 Intergrator

Two very simple numerical schemes that are widely used in MD are known as the Leapfrog and velocity verlet methods. They are completely equivalent algebraically. MD simulation method efficiently evaluates different configurational properties and dynamic quantities which cannot generally be obtain by other method. The algorithms for the Molecular Dynamics are discussed below.

3.2.4.1. Leapfrog Verlet

The leapfrog (LF) algorithm (134, 2) requires values of position (\vec{r}) and force (\vec{f}) at time t while the velocities (\vec{v}) are half timestep behind. The first step is to advance the velocities to $t + \frac{1}{2}\Delta t$ by integration of the force

$$\vec{v}\left(t + \frac{1}{2}\Delta t\right) \leftarrow \vec{v}\left(t - \frac{1}{2}\Delta t\right) + \Delta t \frac{\vec{f}(t)}{m}, \quad (3.3)$$

where m is the mass of a site and Δt is the time step.

The positions are then advanced using the new velocities

$$\vec{r}(t + \Delta t) \leftarrow \vec{r}(t) + \Delta t \vec{v}\left(t + \frac{1}{2}\Delta t\right). \quad (3.4)$$

These simulations normally need properties which are simultaneously position and velocity dependent

$$\vec{v}(t) = \frac{1}{2}[\vec{v}\left(t - \frac{1}{2}\Delta t\right) + \vec{v}\left(t + \frac{1}{2}\Delta t\right)]. \quad (3.5)$$

In the LF this is obtained from the average of velocities half a time step either side of time t , and we often use the time scale of 10^{-1} to 10^{-15} s in molecular dynamics processes.

3.2.4.2 Velocity Verlet

In the velocity verlet (VV) (134, 2), it is assumed that the positions, velocities, and forces are known at each full time step. Firstly a half time step velocity is calculated

$$\vec{v}\left(t + \frac{1}{2}\Delta t\right) \leftarrow \vec{v}(t) + \frac{1}{2}\Delta t \frac{\vec{f}(t)}{m}, \quad (3.6)$$

this is followed by calculating the full time step position

$$\vec{v}(t + \Delta t) \leftarrow \vec{r}(t) + \Delta t \vec{v}\left(t + \frac{1}{2}\Delta t\right). \quad (3.7)$$

Secondly, using the new positions, the forces are updated so as to get the full time step velocity using

$$\vec{v}(t) \leftarrow v\left(t + \frac{1}{2}\Delta t\right) + \frac{1}{2}\Delta t \frac{\vec{f}(t+\Delta t)}{m}, \quad (3.8)$$

So at the end of the two steps, it can be seen that the positions (\vec{r}), velocities (\vec{v}), and forces (\vec{f}) are coordinated. It calculates the velocities more accurately than the plain verlet algorithm [135] and it's more convenient to code.

3.2.5 Ensemble

Ensembles such as the micro-canonical, canonical, and grand-canonical have to be chosen, where thermodynamic quantities like pressure, temperature or the number of particles are controlled and are also concept in statistical physics that refer to the distribution of initial conditions [128]. A system, once drawn from a certain ensemble, is supposed to follow strictly the Newton's equation of motion eq. (3.1), with energy conserved. The natural choice of an ensemble in MD simulations is the microcanonical ensemble (NVE), since the system's total energy without external potentials is a conserved quantity. Nevertheless, there are extensions to the Newton's laws which also allow simulating different statistical ensembles.

3.2.6 Property calculation

A great value of MD simulation is that it is “omnipotent” at the level of classical atoms. All properties that are well-posed in classical mechanics and statistical mechanics can in principle be calculated. The issues remaining are accuracy and computational efficiency. The properties can be grouped into four categories:

- Structural characterization. e.g radial distribution function, dynamic structure factor, etc.
- Equation of state. e.g free-energy functions, phase diagrams, static response functions like thermal expansion coefficient, etc.
- Transport. e.g viscosity, thermal conductivity, correlation functions, diffusivity, etc.
- Non equilibrium response. e.g plastic deformation, pattern formation, etc.

These steps essentially form the essential framework of MD simulation. Having this tool at hand, it is possible to obtain exact results within numerical precision. Results are only correct with respect to the model which enters into the simulation and they have to be tested against theoretical predictions and experimental findings. If the simulation results differ from real system properties or if they are incompatible with solid theoretical manifestations, the model has to be refined. This procedure can be understood as an adaptive refinement which leads in the end to an approximation of a model of the real world at least for certain properties. The model itself may be constructed from plausible considerations, where parameters are chosen from neutron diffraction or NMR measurements. It may also result from first principle ab initio calculations. Although the electronic distribution of the particles is calculated very accurately, this type of model building also contains some approximations, since many-body interactions are mostly neglected (this would increase the parameter space in the model calculation enormously). However, it often provides a good starting point for a realistic model. An important issue of simulation studies is the accessible time- and length-scale which can be covered by microscopic simulations. Table 3.1 shows a Schematic of different time – and length-scales, occurring from microscopic to macroscopic dimensions. Due to recent developments of techniques like Stochastic Rotation Dynamics (SRD) or Lattice Boltzman techniques, which are designed to simulate the mesoscopic scales, there is the potential to combine different methods in a multiscale approach to cover a broad spectrum of times and lengths [119].

Table 3.1: Schematic of different time – and length-scales, occurring from microscopic to macroscopic dimensions. Due to recent developments of techniques like Stochastic Rotation Dynamics (SRD) or Lattice Boltzmann techniques, which are designed to simulate the mesoscopic scales, there is the potential to combine different methods in a multiscale approach to cover a broad spectrum of times and lengths [119].

Time scale (seconds)	10^{-12} 10^{-9} 10^{-6} 10^{-3} 10^0 		
Length scale (Angstrom)	10^0 10^1 10^2 10^3 		
	Microscale Mesoscale Macroscale Particle models $\xrightarrow{\text{upscale}}$ $\xleftarrow{\text{downscale}}$ Continuum models Model type		
Model basis	Classical mechanics	MPC/SRD	Conservation laws (energy, momentum, mass)
Mathematical model	Ordinary differential Equations Boltzmann .time discretization .moving particles	lattice equations DPD	Partial differential .time-/space discretization .field description
Simulation methods	.Molecular dynamics .Monte carlo .Brownian dynamics	SPH	.FEM .FDM .FVM

It is clear that the more detailed a simulation technique operates, the smaller is the accessibility of long times and large length scales. Therefore quantum simulations, where electronic fluctuations are taken into account, are located in the part of the diagram of very short time and length scales which are typically of the order of Å and ps. Classical molecular dynamics approximates electronic distributions in a rather coarse-grained fashion by putting either fixed partial charges on interaction sites or by adding an approximate model for polarization effects. In both cases, the time scale of the system is not dominated by the motion of electrons, but the time of intermolecular collision events, rotational motions or intramolecular vibrations, which are orders of magnitudes lower than those of electron motions. Consequently, the time step of integration is larger and trajectory lengths are of order ns and accessible lengths of order 10-100 Å. If one considers tracer particles in a solvent medium, where one is not

interested in a detailed description of the solvent, one can apply Brownian dynamics, where the effect of the solvent is hidden in average quantities. Since collision times between tracer particles are very long, one may apply larger time steps. Furthermore, since the solvent is not simulated explicitly, the length scales may be increased considerably. Finally, if one is interested not in a microscopic picture of the simulated system but in macroscopic quantities, the concepts of hydrodynamics may be applied, where the system properties are hidden in effective numbers [119], e.g. density, viscosity or sound velocity.

3.3. Interatomic potentials

Interatomic potentials form the core of any molecular dynamics simulations. A molecular dynamics simulation requires the definition of a potential function, or a description of the terms by which the particles in the simulation will interact. It is the governing equation for the interaction of the particles in the simulation. It is extensively used in the simulation of the structures, defects, dynamical properties, etc. for various materials [136]. A number of empirical interatomic pair-potential forms have been developed such as the rigid-sphere model, the Buckingham potential, the Lennard-Jones potential, the Morse potential and the Born-Mayer potential [137], which are widely used in many simulation. The importance of the interatomic potential function is indeed extensive [138]. The interatomic potentials are a powerful tool to investigate the structures and the mechanical properties [136]. When combined with the electrostatic interactions, it describes the potential energy contained in the system as well as the forces, such as Van der Waals forces and electron cloud interactions that act upon each atom, which determines their motion, and hence their kinetic energy [139]. The interatomic potential used in this study is a type called Buckingham potential function. In the next section, the potential model used will be discussed.

3.3.1 Buckingham potential

The Buckingham potential is similar to the Lennard - Jones potential and is widely used to model non-bonded interactions [140]. These potential functions are commonly used in simulation of various lattice systems (including copper, silver, gold, silicon, and carbon among others) [141-143]. A Buckingham potential is a two-body, semi-empirical

potential that consists of an exponential term to describe the repulsive potential between particles and an r^{-6} attractive term. The Buckingham potential function is of the form

$$U(r_{ij}) = \frac{1}{2} \sum_{i \neq j}^N \frac{q_i q_j}{r} + A_{ij} \exp\left(\frac{r_{ij}}{\rho}\right) - \frac{C_{ij}}{r^6}, \quad (3.9)$$

where the second term (the nearest neighbour interactions) describes the repulsive forces between the ions due to electron cloud overlap, and the third term (second-neighbour interactions) describing the attractive van der Waals interactions, with the usual $\frac{1}{r^6}$ dependence [140]. Where U is the potential energy of a pair of ions i and j separated by a distance r_{ij} , q_i and q_j are their respective charges. The parameter A_{ij} is associated to the hardness of the ions, C_{ij} is the term included to model dispersion and ρ_{ij} is related to the size of the ions. These fitting constants $-A$, C and ρ are used to match the potential function to the appropriate material by ensuring that the crystallographic data and elastic properties of the material are accurately reproduced by the potential function [144].

Chapter 4

Defect Free Anatase and Rutile SnO₂

4.1 Introduction

Research in metal-oxides is a subject of lasting interest due to their outstanding electronic properties. The chemical information and atomic arrangement can be interpreted through the electronic structure of the materials' surfaces and interfaces to measure their mechanical and electrical characteristics. Mechanical stability and electrical conductance are the essential properties in technological advancement in the chemical, pharmaceutical, ceramic, and electronic industries. These materials can be synthesized using chemical and physical methods. The chemical methods include the solution-gelation (sol-gel), whereas the physical methods involve vapor laser and deposition. In both methods, the production of qualitative materials plays a great role and is influenced by the interatomic interactions and the thermodynamics environment of the material. Computational simulations also play a crucial role in predicting the properties of these materials as mentioned in chapter1. For example, molecular dynamics (MD) is often used together with these experimental methods to obtain the reliable method of synthesis.

A great deal of experimental and computational research has been conducted on the tin dioxide (SnO₂) and its counterpart titanium dioxide (TiO₂) in bulk, surface, thin films, and nanoparticle form. A spectrum of experimental analysis ranging from the well-known X-ray diffraction (XRD) methods to the current atomic force microscopy (AFM) have been used to investigate the structural and thermodynamic properties of these oxides. Advanced computer codes based on accurate first-principles calculations and classical molecular dynamics make it possible to predict properties in line with experiments. Matthias Batzill and Ulrike Diebold [3,145] have tabled a comprehensive review of why SnO₂ and TiO₂ are highly crucial in gas sensing and semiconductor applications. These metal oxides possess low electrical resistivity and extreme optical transparency in the visible region of the electromagnetic waves. This property is needed in solar cells, light emitting diodes, flat panel displays, gas sensing, and other optoelectronic devices.

Wager [146] and Presley et al [147] demonstrated that the oxides can act as electric contacts in transparent field effect transistors without interfering with the photons path when entering or leaving the optical active area. This strength of SnO₂ and TiO₂ makes them valuable as energy saving materials.

In this chapter defect free anatase and rutile SnO₂ structures through constant pressure, high temperature environments, will be investigated using classical molecular dynamics (MD). This can be attained by exploring the energy-temperature and volume-temperature relations and the radial distribution functions (RDFs) effects in these two materials. It is apparent from Alvarez and Valladares [148] that the atomic topology also determines the electronic properties of the structured materials, and therefore any understanding of the RDFs and the atomic distribution is relevant in the nucleation and characterization of the structural and optical properties of tin dioxide. In the process, information about the nanoparticle grain size and morphology necessary for the sensor application could be obtained. Under normal conditions, SnO₂ crystallizes in tetragonal rutile structure which belongs to the P4_{2/mnm} space group as mentioned in chapter1. Majority of studies on SnO₂ are lacking the anatase of which will constantly be referred to the TiO₂ counterpart. Experiments and calculations have shown that under high different pressures SnO₂ transforms from rutile to pyrite, to fluorite and then cotunnite structures [10, 49,148]. Sverjensky [149] has theorized that the bulk crystal and interfacial dielectric constant play an important role in controlling whether hydrated ions adsorb directly onto the oxide surface or form electrostatically adsorbed outer-sphere complexes, which is crucial in gas sensing. In the following sections, structural and thermodynamic properties of defect free anatase and rutile SnO₂, using the MD simulation based on the Buckingham empirical two-body potential is being discussed. The RDF's of both structures will also be discussed, specifically how Sn-Sn, Sn-O and O-O bonds distribute and relate themselves in the two structures.

4.2 Structure of defect free anatase and rutile SnO₂

Figure 4.1 and 4.2 show the unit cell and the supercell of defect free anatase SnO₂ respectively. The oxygen parameter for anatase SnO₂ is 0.2066 Å and there are four Sn-O distance of 1.937 Å and two of 1.964 Å [150, 151]. It has a space group (no. 141; D_{4h}^{19} ; $I4_1$) [56]. Anatase SnO₂ is optically negative. This metastable structure is less dense, less studied and shows different physical and chemical behaviour than rutile structure [152]. So, most of what is described here is largely in reference to the TiO₂ anatase phase. The stability of the structure therefore resides in a different balance between attractive and repulsive interactions [153].

Figure 4.3 and 4.4 below show the unit cell and the supercell of rutile SnO₂ respectively. The oxygen parameter for rutile SnO₂ is 0.3066 Å and there are four Sn-O distance of 1.937 Å and two of 1.964 Å [150, 151]. It has a space group (no. 136; D_{4h}^{14} ; $P4_2/mnm$) [56]. Rutile is optically positive, with a dense structure. This structure has been extensively studied and is known as a gas sensor and a catalyst [154]. It is known as a stable phase of SnO₂. In all the structures, the red colour is associated with oxygen atoms and grey colour is associated with Sn atoms. Comparing the structures of anatase and rutile SnO₂ from figures (4.1-4.4), it is clearly noticeable that the anatase SnO₂ spans a larger volume compared to rutile. This is due to the fact that anatase SnO₂ is a metastable phase. The structure of rutile SnO₂ is ordered, owing to its stability.

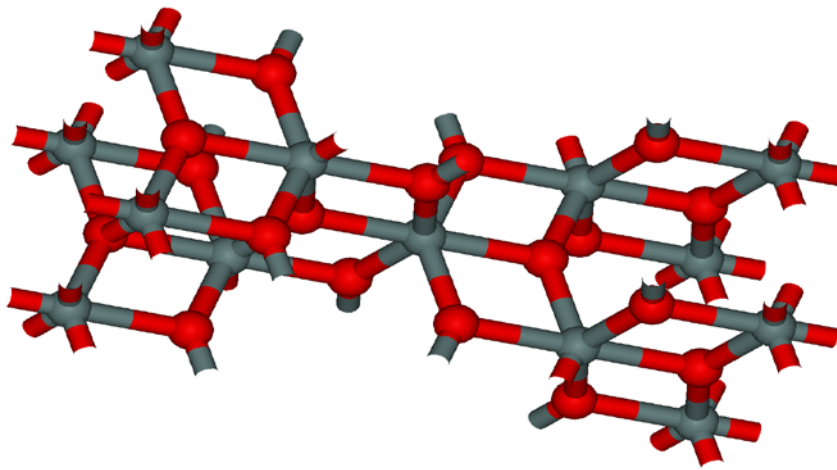


Figure 4.1: The unit cell of crystal structure of anatase SnO₂.

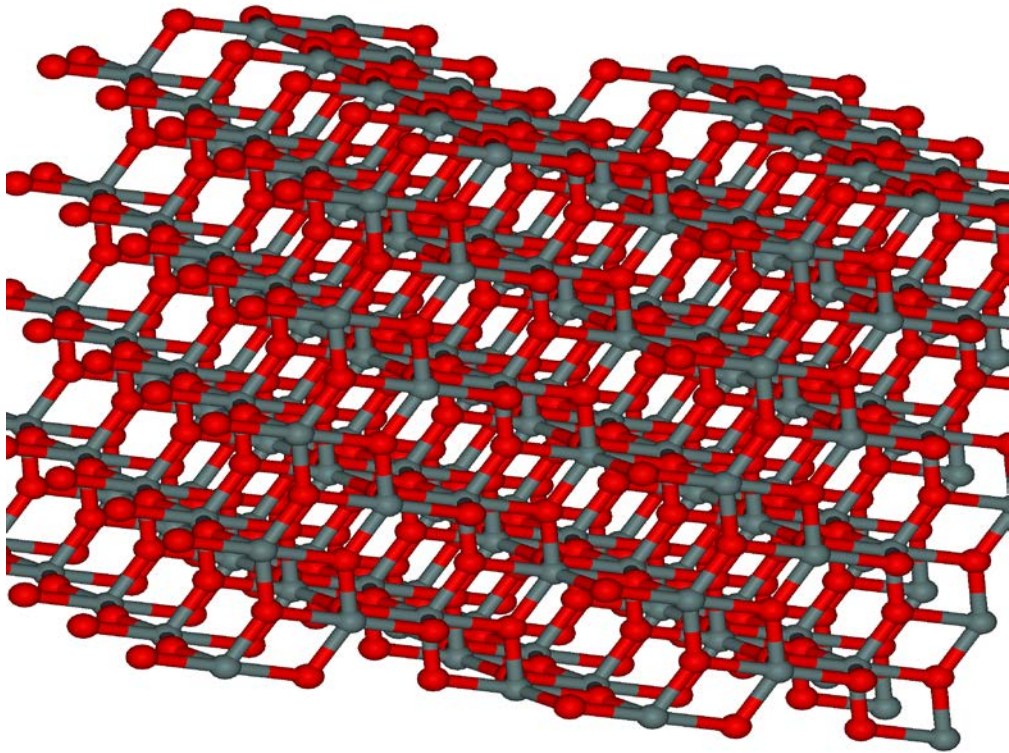


Figure 4.2: The supercell of crystal structure of anatase SnO₂.

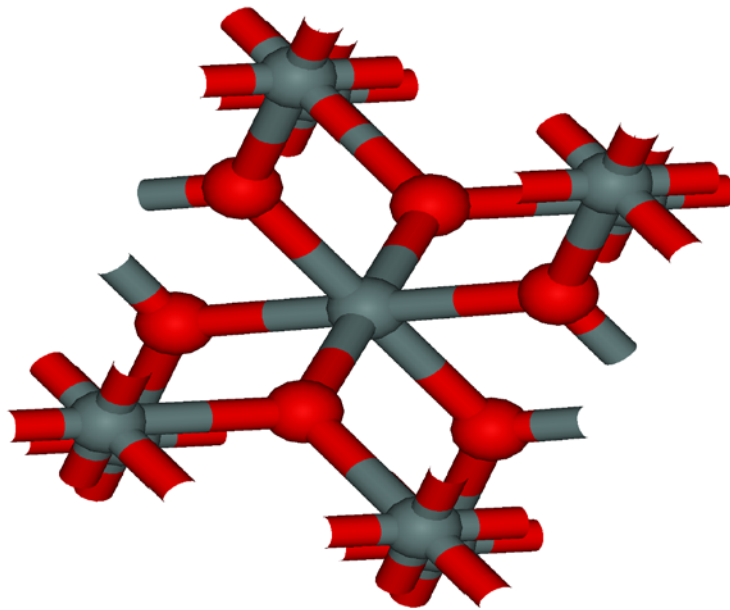


Figure 4.3: The unit cell of crystal structure of rutile SnO₂.

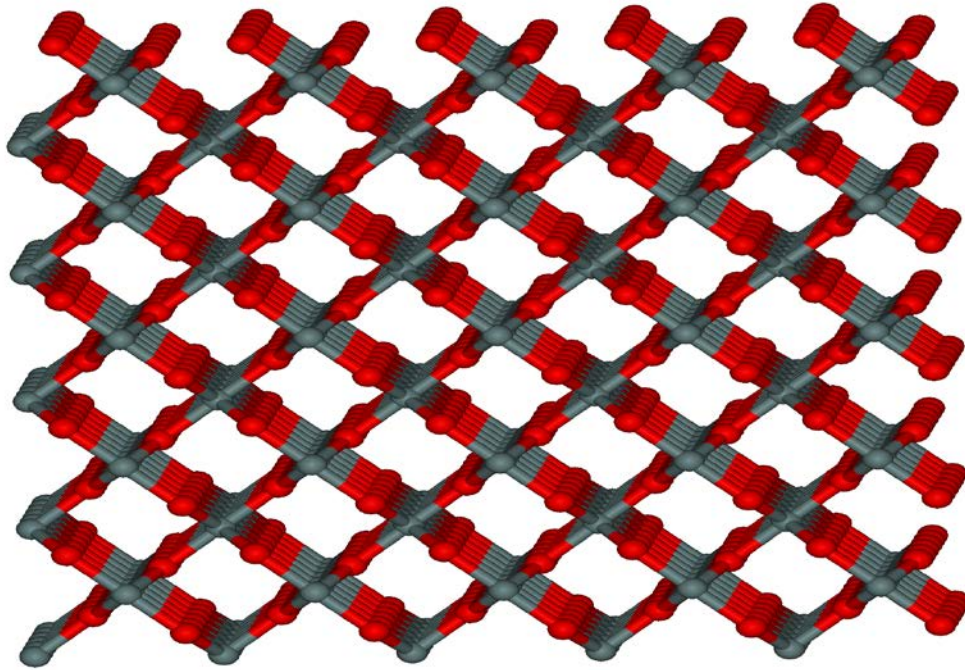


Figure 4.4: The supercell of crystal structure of rutile SnO₂.

4.3 Equilibrium properties

To test the reliability of the empirical two-body Buckingham potential in describing undoped SnO₂, the RDFs for both defect free rutile and anatase SnO₂ were calculated. From peak positions of RDFs' plots, the most probable distances between atoms can be determined. The RDFs are shown at 300 K and 3000 K for each material (anatase SnO₂ and rutile SnO₂). The DL_POLY package [134] from Daresbury Laboratory, UK, was used to perform all the empirical bond-order molecular dynamics calculations of anatase and rutile SnO₂. A supercell with a 7.29 Å cut off, 576 atoms and a very large number of grid points for the fast Fourier transformations (kmax1=6, kmax2=6, and kmax3=12) were used throughout the calculations for anatase SnO₂ whereas a 4.55 Å cut off, 480 atoms, and a sufficiently large number grid points for the fast Fourier transformations (kmax1=11, kmax2=1 and kmax3=6) were used throughout the calculations for rutile SnO₂. The ewald convergence parameter of 0.3975 and 0.6537 respectively for anatase and rutile SnO₂, on a Noose-Hoover NPT ensemble which allows the simulation supercell to change was applied. The thermostat relaxation was set at 0.1 whilst the barostat was at 0.5. The simulation was allowed to run for more than 2000 steps, with an equilibration after every 200 steps and a time steps of 0.001ps. The materials used for the MD modelling are described by its lattice parameters as listed in table 4.1 and a set of parameters required for the Buckingham potential are taken from Bandura et al. [77] and Armstrong et al. [78] as shown in table 4.2.

Table 4.1: Lattice parameters and relative sites for anions and cations in anatase and rutile SnO₂ crystal structures [55,155].

	Anatase		Rutile	
a(Å)	3.8263		4.7377	
c(Å)	11.3194		3.1863	
anions	$\pm(u,u,0)$	$\pm(\frac{1}{2}+u,\frac{1}{2}-u,\frac{1}{2})$	$\pm(u,u,0)$	$\pm(\frac{1}{2}+u,\frac{1}{2}-u,\frac{1}{2})$
cations	(0,0,0)	($\frac{1}{2},\frac{1}{2},\frac{1}{2}$)	(0,0,0)	($\frac{1}{2},\frac{1}{2},\frac{1}{2}$)

Table 4.2: Buckingham potential parameters used for SnO₂ [77, 78].

Interaction	A (eV)	ρ (Å)	C (eV)
Sn-Sn	0.0	0.1	0.0
Sn-O	938.7	0.3813	-
O-O	22764.3	0.149	27.88

4.4. RDF's analysis for defect free anatase and rutile SnO₂

Figure 4.5 and 4.6 show the RDFs of defect free anatase SnO₂ at 300 K and 3000 K respectively. Radial distribution functions (RDFs) have been used to examine the local bonding environment of atoms in SnO₂. For all the computations, anatase's RDFs are constantly compared with those for rutile SnO₂ in a temperature range 300 K to 3000 K. The RDFs show the bonding of the anatase and rutile SnO₂. This method of analysing, the crystal structure of solids gives a better understanding of the complex bonding of atoms in the material. The peaks' values are associated with the bond-lengths between the atoms. Each peak contains information about the location of atoms in the crystal structure of the material. The longer bond-lengths in the material indicate that the distance between the atoms have weaker intermolecular bonds. It can be observed that at a low temperature, 300 K the peaks are close to each other, long and sharp, indicating that the atoms are restricted in their locations, whereas at higher temperature 3000 K the peaks are short and broad, indicating that the atoms are not restricted in their locations. At the long range of RDFs in both Figures 4.5 and 4.6, the reductions of the peaks sizes were observed. The peaks at very long range suggest amorphous behaviour. The Sn-O bond-length remains constant with the increasing temperature. A shift of Sn-Sn and O-O bond-lengths with increasing temperature is observed, suggesting a possible structural deformation from the third nearest neighbour atoms and phase transformation, which might occur in agreement with first principle calculations of Yanlu Li et al. [10] and the experiments of Bachmann et al. [156] and Fan and Reid [157]. Figure 4.7 and 4.8 show the RDFs of defect free rutile SnO₂ at 300 K and 3000 K respectively. At the long distance the peaks of rutile looks disordered and they show similar behaviour as anatase SnO₂, meaning that at long distance, the bond-lengths of the source and neighbouring atoms become weaker with the increase in distance, suggesting amorphous behaviour. The shift of all bond lengths was observed at 3000 K. The peaks at 3000 K are broader than the ones at 300 K indicating that at higher temperature atoms have freedom of movement. The increase of the broadness of the peaks from 300 K to 3000 K is very small possibly due to the fact that rutile SnO₂ is known to be a stable phase of SnO₂.

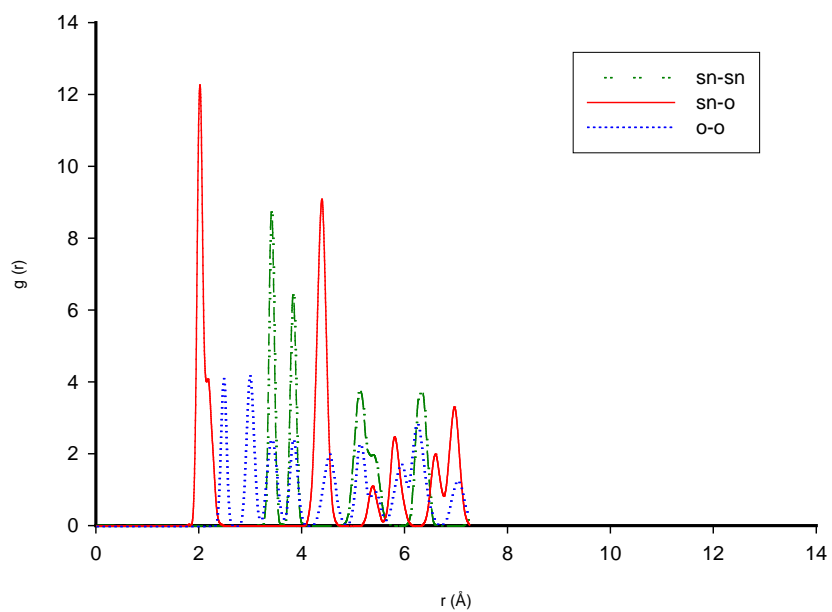


Figure 4.5: RDF plots for Sn-Sn, Sn-O, and O-O coordination in anatase SnO_2 at 300 K.

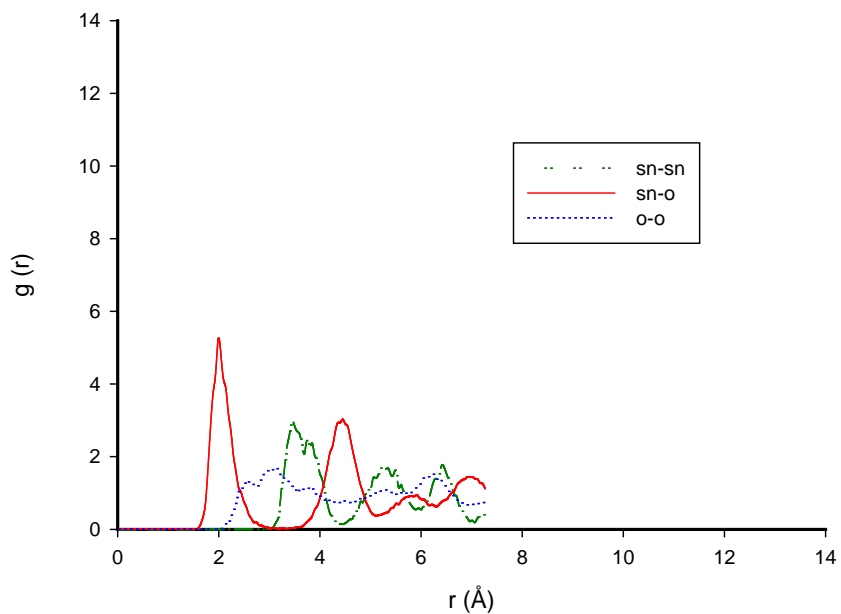


Figure 4.6: RDF plots for Sn-Sn, Sn-O and O-O coordination in anatase SnO_2 at 3000 K.

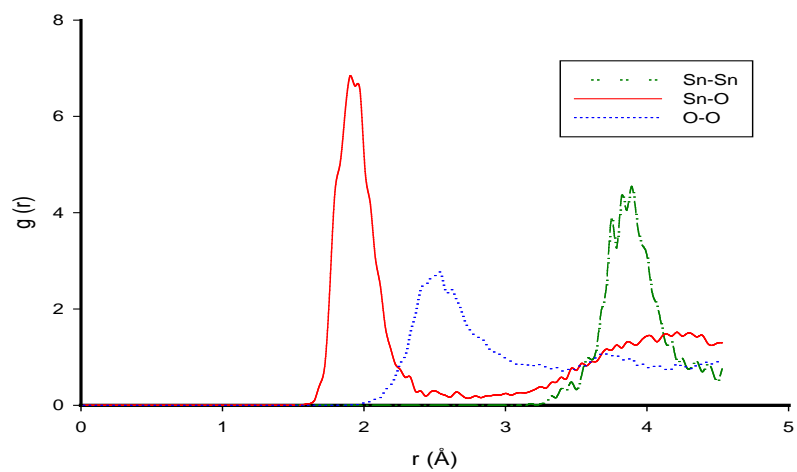


Figure 4.7: RDFs plots for Sn-Sn, Sn-O, O-O coordination for rutile SnO₂ at 300 K.

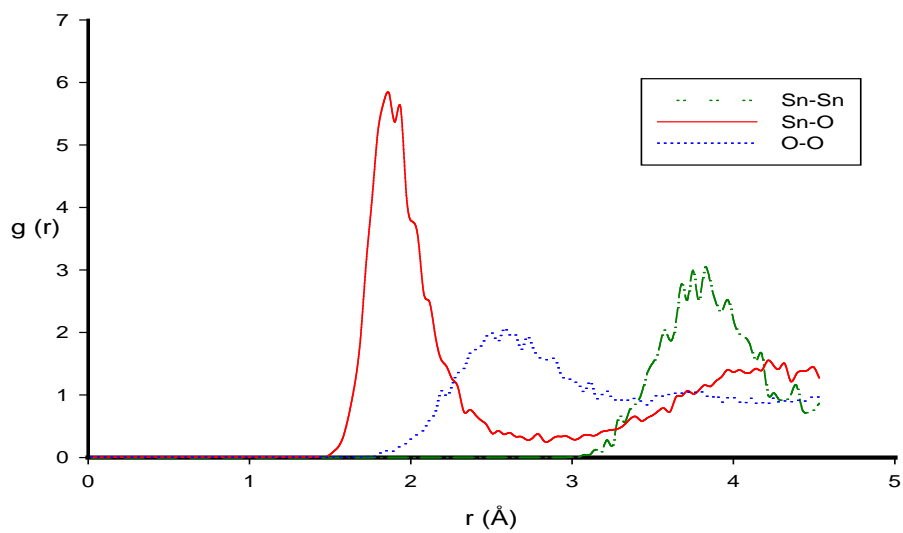


Figure 4.8: RDFs plots for Sn-Sn, Sn-O, O-O coordination for rutile SnO₂ at 3000 K.

The behaviour of Sn-O and Sn-Sn bond-lengths peaks of the rutile SnO₂ at both temperatures 300 K and 3000 K are more or less the same. The slight shift of RDFs' peaks of the material from 300 K to 3000 K, show that temperature has a slight effect on the stability of the rutile SnO₂. Table 4.3 and 4.4 below show the bond-lengths at 300 K and the bond-lengths at 3000 K in both anatase and rutile SnO₂ respectively, which were deduced from Figures 4.5, 4.6, 4.7 and 4.8. It can be observed that Sn-O bond-length of anatase SnO₂ remain constant as the temperature increases whereas for rutile SnO₂ decreases considerably.

Table 4.3: The bond-lengths in angstroms (Å) of anatase and rutile SnO₂ at 300 K.

SnO ₂	Sn-O(Å)	Sn-Sn(Å)	O-O(Å)
Anatase	2.01	3.41	2.48
Rutile	1.92	3.83	2.54

Table 4.4: The bond-lengths in angstroms (Å) of anatase and rutile SnO₂ at 3000 K.

SnO ₂	Sn-O(Å)	Sn-Sn (Å)	O-O (Å)
Anatase	2.01	3.47	2.55
Rutile	1.86	3.66	2.52

At 300 K it can be seen that the Sn-O of rutile is smaller than that of anatase. The size of the bond-lengths tells about the strength or weakness of the structure. From the results, considering the size of Sn-O bond-length it is concluded that rutile is stable than anatase. At 3000 K there is a decrease of O-O bond-lengths for rutile and an increase of Sn-Sn and O-O bond-lengths for anatase. Comparing the two phases of SnO₂, it is found that at higher temperatures, anatase Sn-Sn bond-length has increased whereas rutile Sn-Sn bond-length has decreased. The increase in bond-lengths of anatase SnO₂ indicates that the structure is unstable. The rutile SnO₂ bond-length of Sn-O is strong and has small value, as compared to the other bond-lengths of the material. The increase in temperature from 300 K to 3000 K does not affect Sn-O bond-length in anatase. However Sn-O bond-length in rutile SnO₂ gets affected possibly due to reduction of oxygen vacancies at higher temperature [158]. In rutile SnO₂, the interaction between O and Sn can be altered by increasing temperature which results in modifying the material structure. Ozkinder et al., [42] found that O bonding with Sn (Sn-

O) causes a strong coulomb force and it is not affected by the temperature, which is in agreement with Sn-O bond of anatase SnO₂.

4.5 Thermodynamic properties

In this section the thermodynamic properties of anatase and rutile SnO₂ from 600 K to 3000 K is considered. Quantum mechanical properties effects are very important in understanding the thermodynamic properties below the Debye temperature. Since molecular dynamics treats the motion of the atoms classically, only thermodynamic properties above the Debye temperature of 570 K by Tuerkes et al. [159] and 620 K by Bachmann et al. [156] are considered, where quantum mechanical effects can be neglected. So the average of the two, Debye temperature was estimated at 595 K. All the plots for evaluating thermodynamic properties are functions of temperature. Thermal expansion is of both practical and theoretical importance when calculating the equation of state of the material.

4.5.1 Volume thermal expansion coefficient of SnO₂

The volume thermal expansion coefficient is given by [160]

$$\alpha_v = \frac{1}{V} \left(\frac{dV}{dT} \right), \quad (4.1)$$

where α is the thermal expansion coefficient, V is the volume of the material, and dV / dT is the rate of change of volume with temperature, T is the temperature of the system. Figure 4.9 below shows the volume of anatase and rutile SnO₂ as a function of temperature from 600 K to 3000 K. The simulation data was fitted to the polynomial functions of temperature as

$$V(T) = 2.198 \times 10^{-8} T^2 + 0.0001T + 13.859 \quad (4.2)$$

and $V(T) = 3.293 \times 10^{-8} T^2 + 0.0004T + 10.193,$ (4.3)

for anatase and rutile SnO₂ respectively. The volume thermal expansion coefficient for both anatase and rutile SnO₂ were determined from equation (4.1) together with (4.2) and (4.3) to be $9.1195 \times 10^{-6} \text{ K}^{-1}$ and $4.3118 \times 10^{-5} \text{ K}^{-1}$ respectively. For anatase SnO₂, the volume thermal expansion coefficient differs by a few orders from the measured value

of $11.7 \times 10^{-6} \text{ K}^{-1}$ by Peercy and Morosin [161]. It should also be noted that Peercy and Morosin carried out Raman measurements on a rutile SnO_2 structure. It has also been seen that the volume-temperature data for anatase SnO_2 is quite ordered and the volume is directly proportional to temperature. For rutile SnO_2 the value is far much less than the value of Peercy and Morosin who measured the volume thermal expansion of SnO_2 from 93 to 700 K using Raman spectroscopy to be $11.7 \times 10^{-6} \text{ K}^{-1}$. It has also been seen that the volume-temperature data for rutile SnO_2 is quite disordered although it is far below that of anatase SnO_2 .

4.5.2 Specific heat capacity of SnO_2

The specific heat of rutile and anatase SnO_2 is obtained from the temperature derivative of the total energy of the system

$$C_v = \left(\frac{\partial E}{\partial T} \right)_v, \quad (4.4)$$

where C is the specific heat, E is total energy, $\frac{\partial E}{\partial T}$ is the rate of change in energy and T is the temperature of the system. Figure 4.10 shows the total energy as a function of temperature for anatase and rutile SnO_2 . The specific heat of anatase and rutile SnO_2 is obtained from equation (4.4) to be 3.48 k_B and 3.48 k_B , respectively with the increasing temperature. The results of anatase and rutile SnO_2 seem to differ considerably from the measured value of 6.32 k_B [196] but is in agreement with the Dulong-Petit's law of solids at high temperatures. Table 4.5 below shows the calculated values for volume thermal expansion coefficient and specific heat capacity from Figures 4.9 and 4.10 and literature [196].

Table 4.5: The volume thermal expansion coefficient and specific heat capacity of anatase and rutile SnO_2 .

SnO_2	Volume thermal expansion coefficient (K^{-1})	Specific heat capacity (k_B)
anatase	9.120×10^{-6}	3.48
rutile	4.312×10^{-5}	3.48
Other work[196,161]	11.700×10^{-6}	6.32

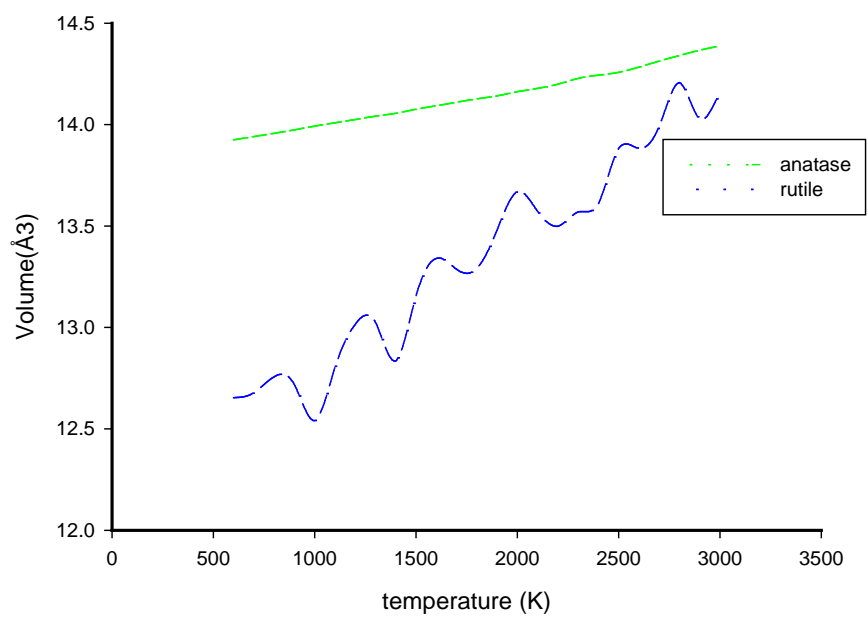


Figure 4.9: Volume as a function of temperature for anatase and rutile SnO_2 .

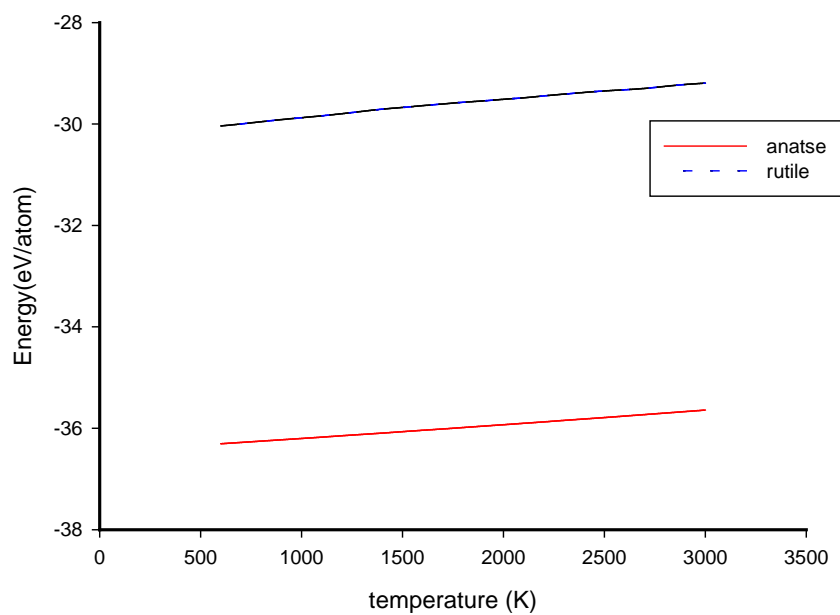


Figure 4.10: Energy as a function of temperature for anatase and rutile SnO_2 .

4.6 Conclusion

In summary, anatase and rutile SnO₂ have been modelled successfully with molecular dynamics simulation using the Buckingham potential to investigate their stability and thermodynamic properties (volume thermal expansion coefficient and specific heat capacity). The radial distribution functions curves suggest phase transformation at high temperatures. The Sn-O bond-length in anatase SnO₂ appears rigid and constant at 2.01 Å whereas Sn-O in rutile SnO₂ decreases from 1.92 Å to 1.86 Å with the increasing temperature. The temperature has no effect on the Sn-O bond-lengths of anatase SnO₂ structures. The effect of temperature to the crystal structure of the material is small. The structure of rutile SnO₂ is very stable at higher temperatures as compared to the anatase structure. Anatase SnO₂ has the lowest energy and high volume compared to rutile SnO₂. The volume thermal expansion coefficient of anatase underestimates the measured value whereas the rutile overestimates it. The specific heat capacities of both anatase and rutile SnO₂ are not in agreement with the measured value although they are in the region of the theoretical Dulong-Petit law of solids at high temperatures. The energy of both materials is directly proportional to the temperature.

Chapter 5

The role of Ti and Y defects in Anatase SnO₂

5.1 Introduction

Doping tin dioxide (SnO₂) with metal impurities has proved to enhance its properties, both electrically and mechanically. The combination of these properties can also enhance the sensing properties of this material. SnO₂ is a kind of material that come from nature being doped, because even if it is not doped it is still favoured for many useful technological applications such as gas sensors, catalyst and many more [162] as mentioned in the general introduction of the first chapter. It is reported that when it is undoped, SnO₂ has a problem of grain growth at higher temperature and cross sensitivity [163] which results in poor performance. Furthermore application of dopants on the material minimizes some of the material draw backs. Many studies have shown that the reduction of grain growth can be achieved and also the performance of SnO₂ can be significantly enhanced by introduction of defects or dopants. There are so many defects that the material can undergo such as interstitial defect, substitutional defect, oxygen vacancy and many more, but in this study the focus is directed to substitutional defects on the tin (Sn) site.

The aim of introducing dopants in most cases is to create or enhance desirable properties, while others are to eliminate or reduce undesirable effects. It is found that different dopants yield different results. The influence of dopants on the material differs by their nature and size of their ionic radii. Their degree of effect on the material is determined by their location on SnO₂. The increasing temperature which the doped material were subjected to, together with the influence of transition metal Ti and Y impurities in anatase SnO₂ are discussed. Thereafter, these impurities will be constantly compared with the defect free anatase and rutile SnO₂ from the previous chapter. As in the previous chapter, the bond-lengths of the doped SnO₂ were determined by Radial Distribution Function. The stability of the material is determined by comparing the bond-

length between 300 K and 3000 K temperatures. Correspondingly, NPT hoover ensemble will be used to study thermodynamic properties.

5.2 Equilibrium properties

The Buckingham potential parameters for Ti and Y in SnO₂ were extracted from the literature by Dushanov and co-workers [164] and Lewis [165]. These were incorporated to the defect free potentials as discussed in Table 4.2 of chapter 4. The revised Buckingham potentials are as they appear in Table 5.1. Ti and Y defects are introduced only in the anatase phase of SnO₂ so as to also investigate their possible role in transforming anatase to rutile SnO₂. From the anatase SnO₂ configuration of section 4.3, a doped supercell now has 191 atoms of Sn, 384 atoms of O, and either Ti and Y atom to make a 576 atom supercell in the original 141\amd space group [56]. All other starting parameters remain the same as in the defect free anatase SnO₂. There is a likelihood that different temperature RDFs would be able to suggest the effect of Ti and Y in transforming anatase to rutile SnO₂. The strategy is to compare the RDFs with and without the O-Ti and O-Y bond-lengths relative to the analysis as reviewed in section 4.4. The materials resulting from doping will be referred to as Ti-anatase SnO₂ and Y-anatase SnO₂ respectively for Ti and Y defects.

Table 5.1: Buckingham potential parameters used for Ti and Y in SnO₂, where A, ρ , and C are parameters in the equation for the Buckingham potential [77,78,164,165].

interaction	A (eV)	ρ (Å)	C (eV)
Sn-Sn	0.0	0.1	0.0
Sn-O	938.7	0.3813	-
O-O	22764.3	0.149	27.88
Ti-O	391049	0.194	290.331
Y-O	1345.1	0.3491	0.0

5.2.1 RDF's analysis for doped anatase SnO₂

5.2.1.1 Ti-anatase SnO₂

The RDFs of Ti-anatase SnO₂ are shown in Figure 5.1 (a) and (b) for 300 K and Figure 5.2 (a) and (b) for 3000 K with and without O-Ti bonds respectively. Comparing the RDFs of free defect anatase and rutile SnO₂ and Ti-anatase SnO₂ at 300 K, it is observed that Sn-O bond-length of the doped material is higher than that of a free defect SnO₂. The bond-lengths Sn-Sn and O-O have increased in relation to the defect free anatase SnO₂, although still lower than those for the defect free rutile SnO₂. It can be seen that the bond-length O-Ti is shorter than Sn-O and the rest of the bond-lengths in Ti-anatase SnO₂. This suggest that the Ti atom tend to shorten the Sn-O bond in anatase SnO₂, thus triggering transformation to rutile SnO₂. From the results it is evident that the Ti dopant has effect on the crystal structure of the material. The increase of the Sn-O bond-length indicates that the stability of the material has been altered. The peaks' behaviour is more or less the same, except their size. At 3000 K, the bond-length Sn-O of Ti-anatase SnO₂ is equal to the bond for free defect anatase SnO₂ but greater than rutile SnO₂. The increase of Sn-Sn and O-O bond-lengths reflect the crystal growth being influenced by the Ti defect. From the results, it can be concluded that doped material have smaller crystals at higher temperature than undoped. Figure 5.2 (b) shows the RDF of SnO₂ without the O-Ti bonds at 3000 K. This shows a transition process from anatase to rutile SnO₂, as the RDFs for rutile are shown in Figure 4.7 and 4.8 from chapter 4.

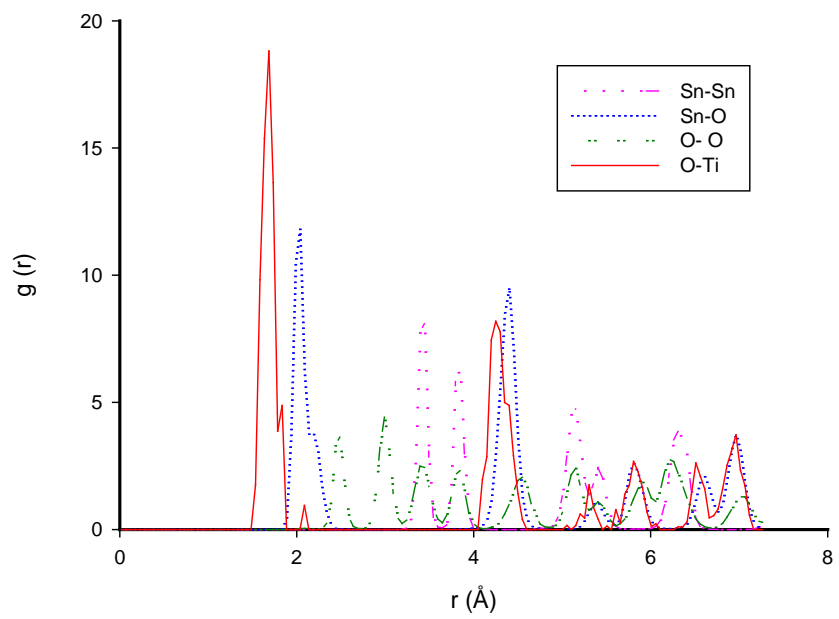


Figure 5.1(a): RDF of Ti-anatase SnO₂ at 300 K.

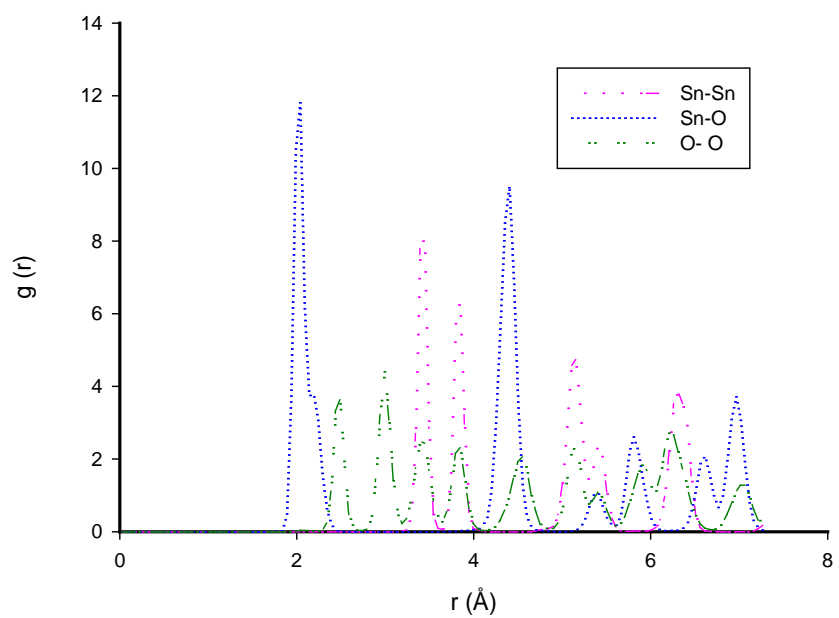


Figure 5.1 (b): RDF of Ti-anatase SnO₂ at 300 K without O-Ti bonds.

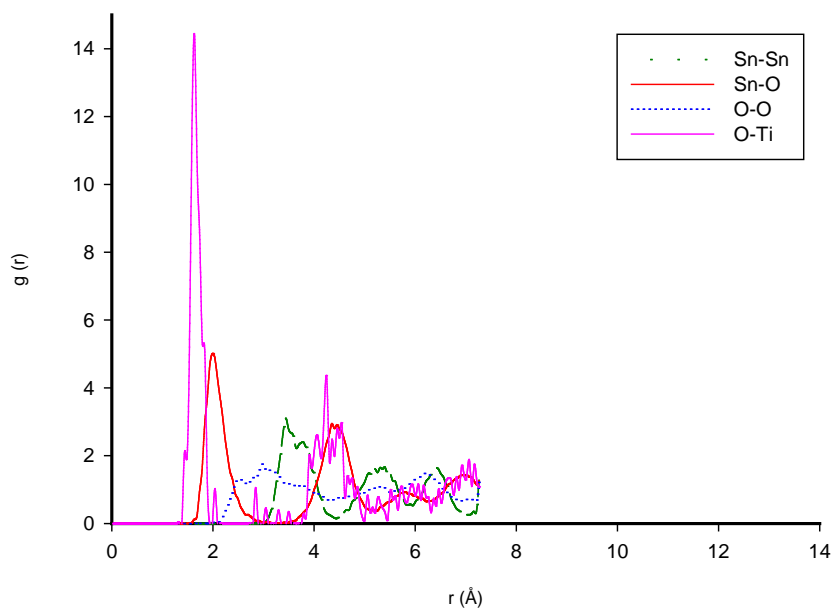


Figure 5. 2 (a): RDF of Ti-anatase SnO₂ at 3000 K.

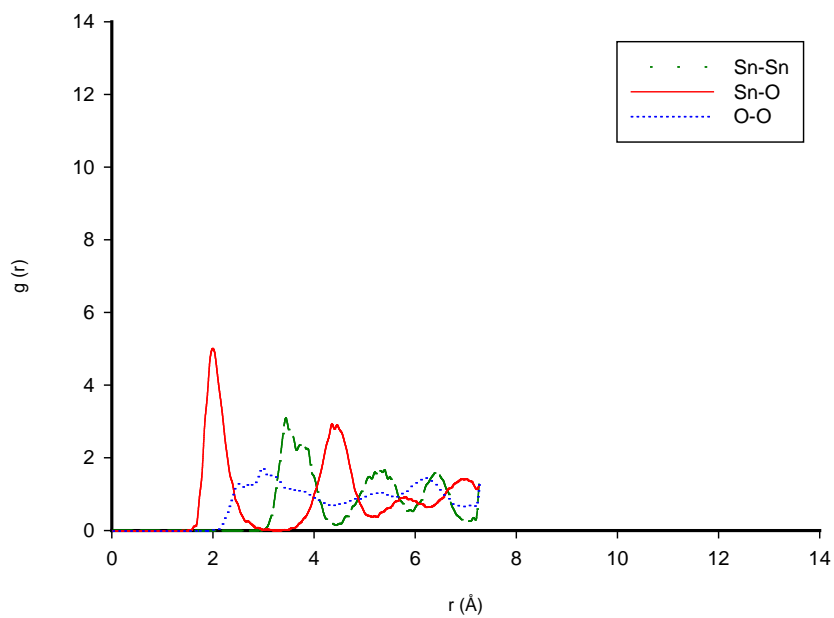


Figure 5. 2 (b): RDF of Ti-anatase SnO₂ at 3000 K without O-Ti bonds.

Figure 5.3 and 5.4 show the crystal structure of Ti-anatase SnO₂ at 300 K and 3000 K respectively. The Titanium (Ti), Tin (Sn), Oxygen (O) atoms are associated with silver, grey and red colours respectively. At 300 K, the Ti and Sn have 6 O nearest neighbours. The incorporation of Ti atom in the SnO₂ crystal structure does not show much change since the ionic radius of the defects Ti (0.68 Å) is close to that of the host atoms (Sn)(0.71 Å). At 3000 K, it can be seen that Ti has 5 O coordination, although Sn has 5 and 6 O coordination. The atoms of the structure are scattered as compared to the one at 300 K. This is due to the freedom of movement that caused by the higher temperature. At this temperature (3000 K) the crystal structure behave more like rutile structure, which indicate that at higher temperature, anatase phase transform to rutile phase. The arrangements of atoms for Ti-anatase SnO₂ at 300 K are ordered whereas at 3000 K are disordered. The deformation of the structure shows that anatase is not a stable phase of SnO₂. This can be explained clearly by the breakage of bonds at higher temperature. The bond-length of Ti-O in both temperature 300 K and 3000 K appear shorter than Sn-O bond-lengths as it has been mentioned above in the previous section. The results are in agreement with the results of the RDFs on the fact that crystal growth influenced by the Ti-defects.

5.2.1.2 Y-anatase SnO₂

The RDFs of Y-anatase SnO₂ are shown in Figure 5.5 (a) and (b) for 300 K and Figure 5.6 (a) and (b) for 3000 K with and without O-Y bonds respectively. In a similar fashion, the Y-anatase SnO₂ and undoped anatase SnO₂ at 300 K will be compared. The bond-length Sn-O for Y-anatase SnO₂ is higher than that of defect free anatase and rutile SnO₂. The size of the other bond-lengths, Sn-Sn and O-O, are between that of anatase and rutile SnO₂. It is clear that addition of dopants has the influence on the stability of crystal structure. The peak's behaviour of free defect anatase SnO₂ is more or less the same with Y-anatase SnO₂. The only difference is their peaks' size. Furthermore for Y-anatase SnO₂ at 3000 K, the Sn-O and Sn-Sn bond-lengths are between that of free defect anatase and rutile SnO₂. The O-O bond-length is less than that of both defect free anatase and rutile SnO₂. At higher temperature (3000 K), the peak's behaviour is more or less the same. In the case of Y-anatase SnO₂ the O-Y bond-length is larger than the Sn-O bond-length.

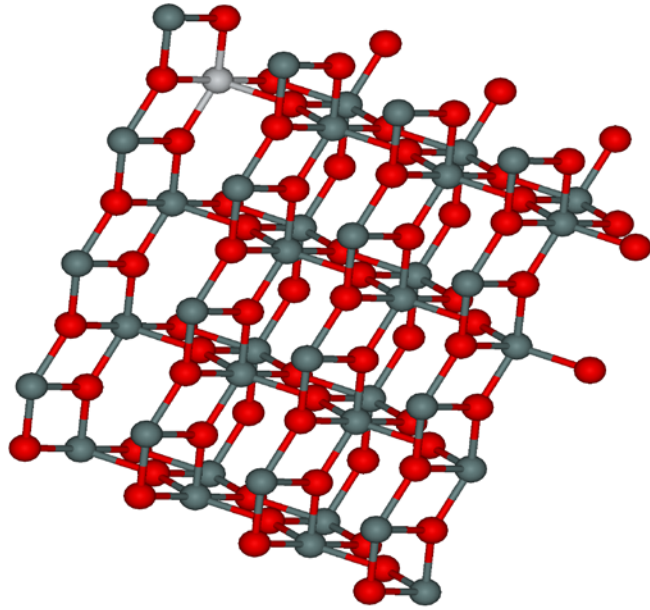


Figure 5.3: The crystal structure of Ti-anatase SnO₂ at 300 K.

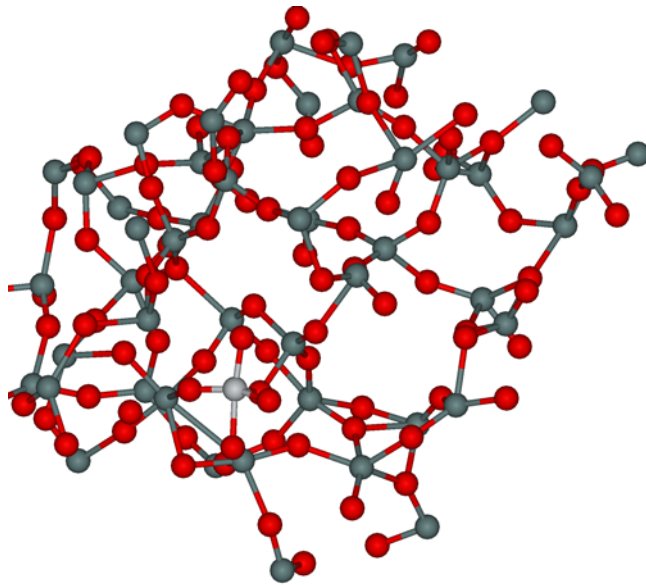


Figure 5.4: The crystal structure of Ti-anatase SnO₂ at 3000 K.

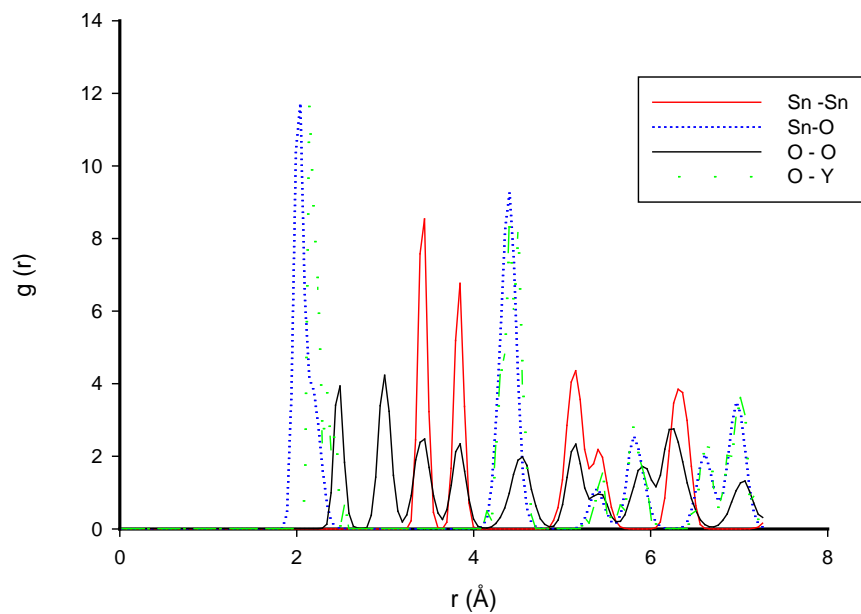


Figure 5.5 (a): RDF of Y-anatase SnO_2 at 300 K.

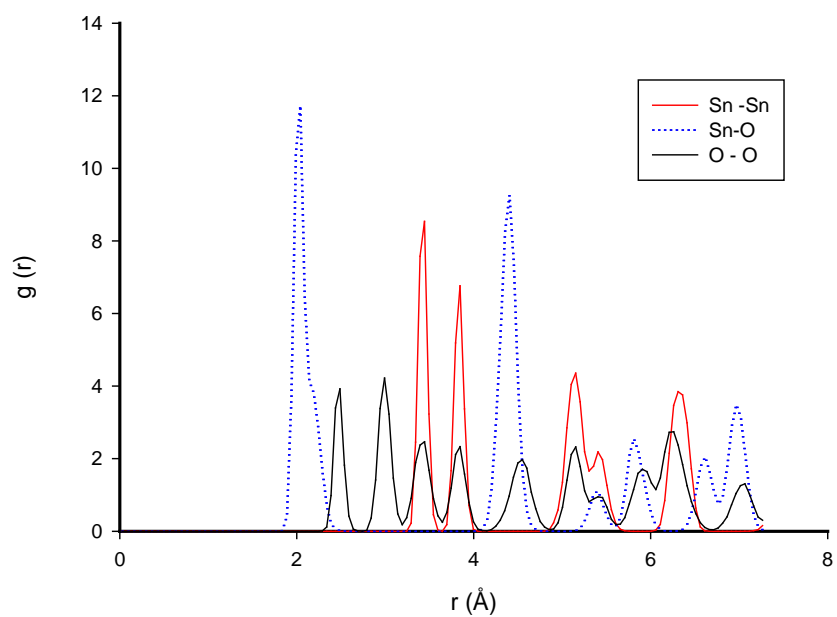


Figure 5.5 (b): RDF of Y-anatase SnO_2 at 300 K without O-Y bonds.

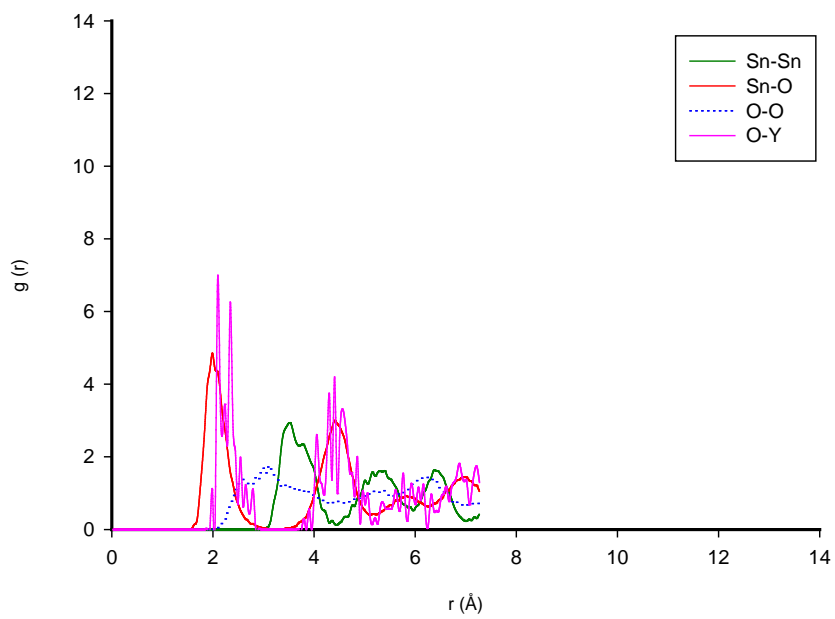


Figure 5. 6 (a): RDF of Y-anatase SnO₂ at 3000 K.

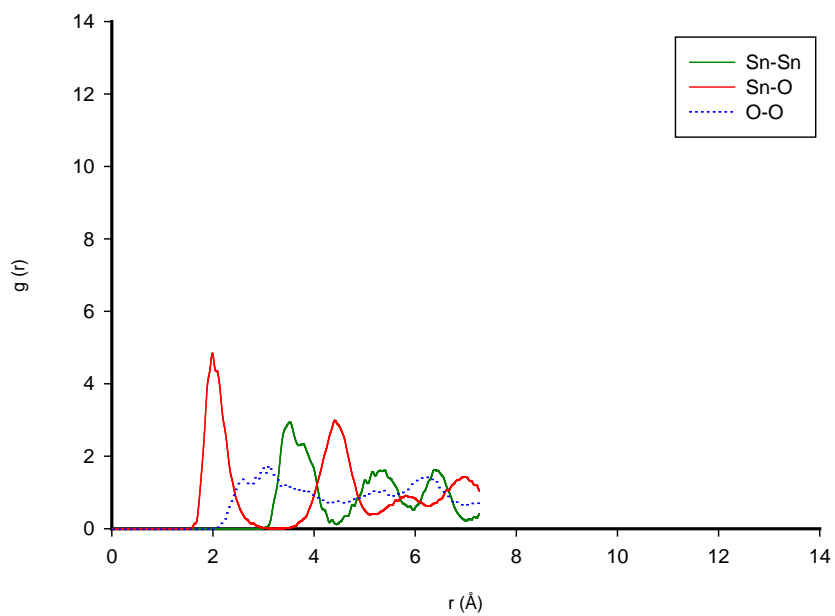


Figure 5. 6 (b): RDF of Y-anatase SnO₂ at 3000 K without O-Y bonds.

This indirectly shows that the Y defect plays no significant role in anatase-rutile transformation. Table 5.2 and 5.3 below show the bond-lengths at 300 K and 3000 K for both Y-anatase and Ti-anatase SnO₂ respectively, which were deduced from the results of Figure 5.1(a and b), 5.2(a and b), 5.5(a and b) and 5.6(a and b). Figure 5.7 and 5.8 show the crystal structure of Y-anatase SnO₂ at 300 K and 3000 K respectively. Yttrium (Y), Tin (Sn), Oxygen (O) atoms are associated with pure cyan, grey and red colours respectively. At 300 K, Y defect is bonded to 10 atoms (4 Sn and 6 O atoms). This indirectly demonstrates the strain that the Y defect exerts in the anatase SnO₂ lattice. As with Ti defect in anatase SnO₂ at lower temperature the structural atoms appear ordered, indicating that the atoms are restricted to their positions. At 3000 K the structure is disordered indicating that the atoms are highly mobile and not limited to their location. The structure now appears to have a coordination of 6, 4, and 3 O atoms respectively. This can be explained as an amorphous SnO₂ structure.

Table 5.2: The bond-lengths (Å) of Y-anatase SnO₂ and Ti-anatase SnO₂ at 300 K.

Materials	Sn-O(Å)	Sn-Sn(Å)	O-O(Å)	O-Ti(Å)	O-Y(Å)
Ti-anatase SnO ₂	2.03	3.45	2.49	1.69	-
Ti-anatase SnO ₂ (without O-Ti)	2.03	3.45	2.49	-	-
Y-anatase SnO ₂	2.03	3.45	2.49	-	2.13
Y-anatase SnO ₂ (without O-Y)	2.03	3.47	2.49	-	-

Table 5.3: The bond-lengths (Å) of Y-anatase and Ti-anatase SnO₂ at 3000 K.

Materials	Sn-O(Å)	Sn-Sn(Å)	O-O(Å)	O-Ti(Å)	O-Y(Å)
Ti-anatase SnO ₂	2.01	3.46	2.51	1.63	-
Ti-anatase SnO ₂ (without O-Ti)	2.01	3.46	2.49	-	-
Y-anatase SnO ₂	1.98	3.52	2.49	-	2.10
Y-anatase SnO ₂ (without OY)	1.98	3.52	2.58	-	-

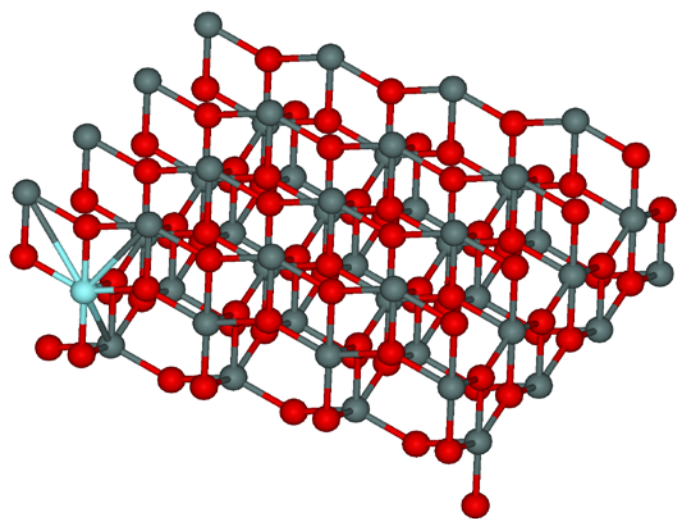


Figure 5.7: The crystal structure of Y-anatase SnO_2 at 300 K.

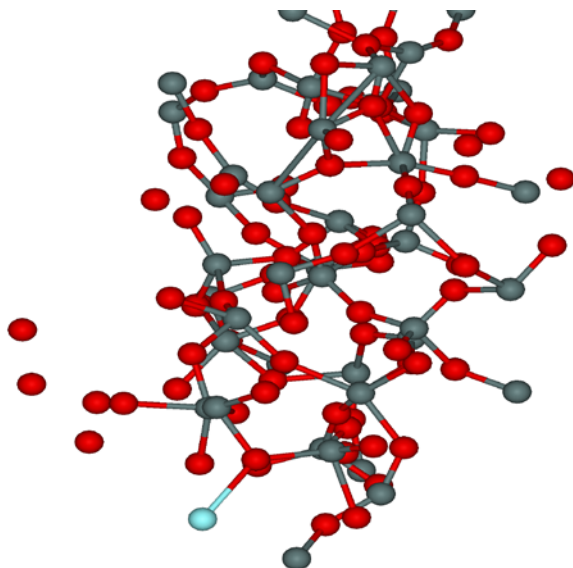


Figure 5.8: The crystal structure of Y-anatase SnO_2 at 3000 K.

5.3 Y- anatase SnO₂ and Ti - anatase SnO₂

The bond-lengths varied with increasing temperature but some remain constant, especially O-O bond-length for Y-anatase SnO₂. The effect of the change in the bond-lengths is attributed to the introduction of dopants and increasing in temperature. It is reported that the effect of change in bond-length is attributed to higher electro-negativity of Sn (1.8) compared to Ti (1.5) atoms [166] which causes a smaller distance between Ti and O than between Sn and O atoms and leads to an irregular arrangement of atoms. Their findings [166] are in reasonable agreement with this study. Comparing the ionic radius of Ti⁴⁺ (0.68Å) and Sn⁴⁺ (0.71Å) it has been found that they are close in size, therefore it is easy for Ti⁴⁺ to be doped into the crystal lattice of SnO₂ and occupy the substitutional positions [167]. At a higher temperature of about 1000 K, it favours the solid solution of SnO₂ [7]. However, this substitutional solid solution is formed by the incorporation of Ti⁴⁺ into SnO₂.

Similarly, comparing the ionic radius of Y³⁺ (0.95Å) and Sn⁴⁺ (0.71Å), it is found that the radii of dopants are slightly bigger than the host material. Therefore it is not easy for Y³⁺ ion to be doped into the crystal lattice of SnO₂ and occupy the substitutional positions. Since Y³⁺ has bigger radius, it is found that the dopants migrated towards the surface of the material [89,168]. In a previous study it was found that at a temperature below 1000 K, Y doped SnO₂, formed a solid solution [89, 168]. Comparing the electronegativity of Sn (1.8) and Y (1.2), it is found that they are not in agreement with what has been mentioned above. The distance between Y and O is bigger than the distance between Sn and O atoms at both temperatures 300K and 3000K, as seen in the results, it is believed to be caused by the size of ionic radius.

5.4 Thermodynamic properties

In this section the thermodynamic properties of Ti-anatase SnO₂ and Y-anatase SnO₂ were determined using the procedure in chapter 4 together with its equations.

5.4.1 Volume thermal expansion coefficient of doped anatase SnO₂

The volume thermal expansion coefficient for Ti-anatase SnO₂ and Y-anatase SnO₂ respectively is obtained using equation (4.1). Figure 5.9 shows the volume of Ti-anatase SnO₂ and Y-anatase SnO₂ as a function of temperature from 600 to 3000 K. The simulation data of Ti-anatase SnO₂ and Y-anatase SnO₂ respectively has been fitted to polynomial function of temperature as

$$V(T) = 1.3556 \times 10^{-8}T^2 + 2 \times 10^{-4}T + 13.7722 \quad (5.1)$$

$$\text{and } V(T) = 1.2287 \times 10^{-8}T^2 + 1 \times 10^{-4}T + 13.8550, \quad (5.2)$$

respectively. The volume thermal expansion coefficient for Ti-anatase SnO₂ and Y-anatase SnO₂ were determined from equations (5.1) and (5.2) together with (4.1) and found to be $1.5703 \times 10^{-5} \text{ K}^{-1}$ and $8.2818 \times 10^{-6} \text{ K}^{-1}$, respectively. The behaviour of the graphs indicates that the dopants have a noticeable effect on the material. The graph of volume as function of temperature for Y-anatase SnO₂ behaves the same way as that of Ti-anatase SnO₂ but its volume is higher than that of Ti-anatase SnO₂. From figure 5.9 below, it can be observed that the volume is increasing with increasing temperature.

5.4.2 Specific heat of doped anatase SnO₂

The specific heat for Ti-anatase SnO₂ and Y-anatase SnO₂ respectively, is obtained from the temperature derivative of the total energy of the system. Figure 5.10 shows energy as a function of temperature for Ti-anatase SnO₂ and Y-anatase SnO₂ at 600 to 3000 K. The specific heat is calculated using equation (4.4) to be $3.48 k_B$ in all the material at higher temperature. The results of Ti-anatase SnO₂ and Y-anatase SnO₂ are in agreement with the Dulong-Petit's law of solids at higher temperature ($>3.0 k_B$) and considerably lower than measured value of $6.32 k_B$ [196]. From the plot of energy as the function of temperature it is observed that energy is directly proportional to the temperature. The Ti-anatase SnO₂ has lower energy than Y-anatase SnO₂ throughout the range. Unfortunately there are no results from literature to compare with this work.

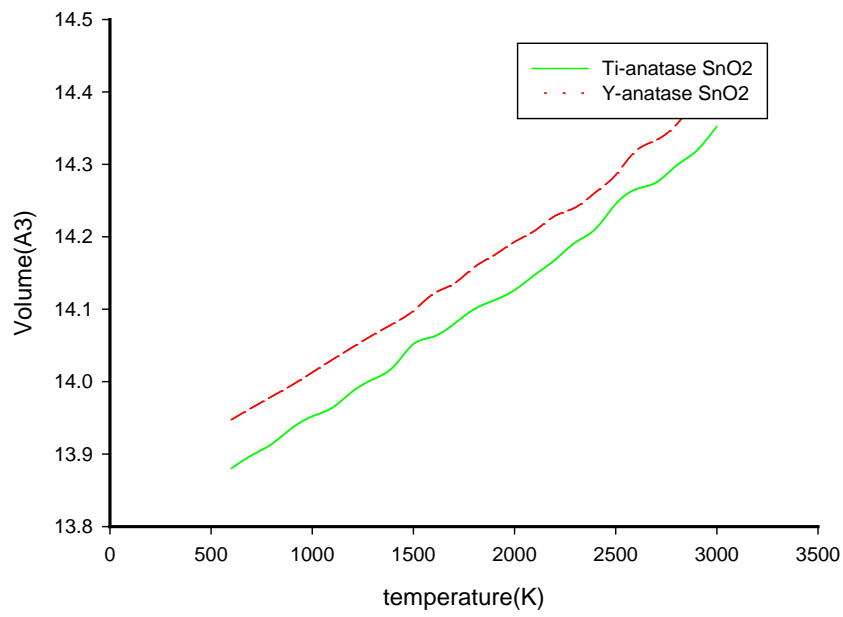


Figure 5.9: Volume as a function of temperature for Ti-anatase SnO₂ and Y-anatase SnO₂.

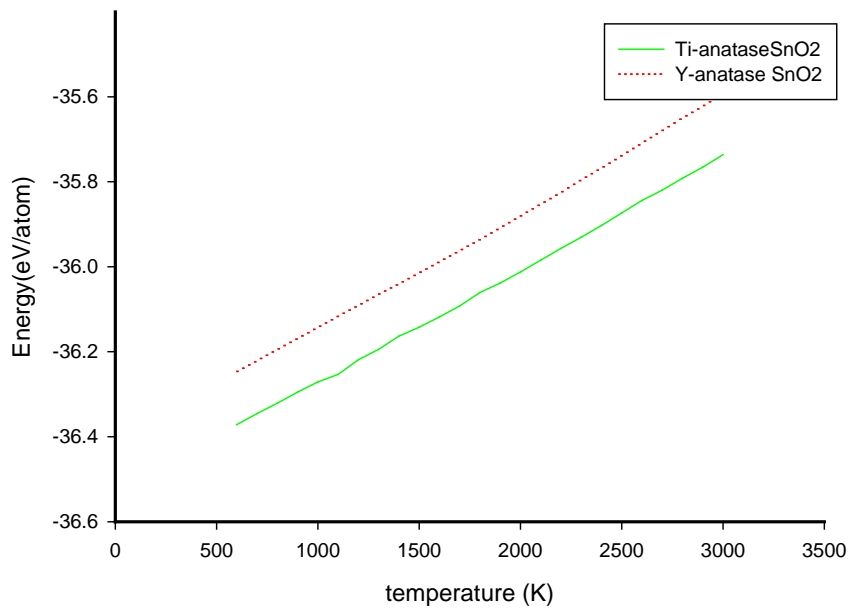


Figure 5.10: Energy as a function of temperature for Ti-anatase SnO₂ and Y-anatase SnO₂.

Table 5.4: The values for volume thermal expansion coefficient and specific heat capacity for doped anatase SnO₂ and undoped SnO₂.

Material	Volume thermal expansion coefficient(K ⁻¹)	Specific heat capacity (k _B)
Ti-anatase SnO ₂	1.5703x10 ⁻⁵ K ⁻¹	3.48
Y-anatase SnO ₂	8.2818x10 ⁻⁶ K ⁻¹	3.48
Dulong-Petit law of solids	-	3.00
Other[196]	-	6.32

5.5 Conclusion

In summary, anatase SnO₂ doped with (Ti and Y) has been successfully modelled using the procedure as in chapter 4. The radial distribution functions give the detailed information about bonding of the SnO₂ structure and also enable researchers to understand and analyse bonding of the material. The radial distribution functions curves suggest structural deformation and phase transformation at higher temperature when anatase SnO₂ is doped with Ti. This has been noted to be accompanied by crystal growth. In the case of Y in anatase SnO₂ a strained lattice is experienced in the neighbourhood of the defect at ambient temperatures. An amorphous material is obtained at high temperatures.

The Ti defect can influence the transformation of anatase to rutile SnO₂ at a lower temperature than the defect free process. The Y defect triggers an amorphous SnO₂. The decrease in bond-lengths of Ti-anatase SnO₂ indicates that the introduction of Ti as dopants in the matrix of the material can improve its performance. The location of the dopants in the material is determined by the size of their radii. The volume increase affects the volume thermal expansion coefficient. Only the volume thermal expansion coefficient for Y-anatase SnO₂ is of the same order as the measured results, whereas for Ti-anatase SnO₂ is not in agreement with the measured results. The material containing Ti as dopants has the lowest energy and volume. The specific heat capacity of the material was found to be the same in all the material.

Chapter 6

Experimental Studies of Aluminum (Al) and Yttrium (Y) doped SnO₂ powder

6.1. Introduction

In this chapter, the experimental results i.e. X-ray powder diffraction (XRD), Raman spectroscopy, Scanning electron microscopy (SEM) and UltraViolet-visible spectroscopy (UV-vis) will be presented. Sample preparation methods and characterization experiments will be described. The analysis of experimental measurements will be presented and discussed.

6.2. Sample Preparations

The samples were prepared in the laboratory using the chemical method i.e. solution-gelation (sol-gel). To synthesise yttrium and aluminium co-doped nanocrystalline tin dioxide, sol-gel method was used due to its number of advantages such as low cost, low temperature processing, molecular level of homogeneity, safety and simplicity etc., [46, 169]. To prepare the sample, appropriate amounts of tin chloride octahydrate and water soluble metal salts (yttrium and aluminium) were dissolved in 40 ml of distilled water to prepare a 0.1 M solution. In this solution, 0.5 ml of aqueous ammonia was slowly added and the resulting white precipitates recovered by evaporation. The by-product of this reaction is ammonium chloride which was removed by extensive washing with distilled water. The material was then oven dried at 100 °C overnight and thoroughly ground in an agate pestle and mortar to make fine nanoparticles. The absence of ammonium chloride peaks in the XRD patterns confirmed the successful removal of all the ammonium chloride. The samples were prepared with dopant concentrations of 10% for each dopant i.e. yttrium and aluminium. The samples were subjected to different temperatures as follows: 100 °C (as-prepared), 200 °C, 400 °C, 600 °C, 800 °C and 1000 °C, and then put in different containers.

6.3 Characterisation Techniques

6.3.1 X-ray Powder Diffraction (XRPD) Studies

The X-Ray diffraction experiments were carried out using Panalytical X'pert Pro PW 3040/60 X-Ray diffractometer equipped with Cu K α ($\lambda=0.154$ nm) monochromatic radiation source. The measurements were extracted at 45.0 KV and 40.0 mA, and the experimental procedure shows good reproducibility of results. Figure 6.1 shows a diagram of a usual X-ray powder diffractometer. The average crystallite size was determined using Scherrer equation [170]

$$D = \frac{K\lambda}{\beta \cos\theta}, \quad (6.1)$$

where D is the crystallite size, K is the constant ($K = 0.89$), λ is the x-ray wavelength ($\lambda = 1.541$ Å) used, β is the full-width at half-maximum (FWHM) of XRPD peaks and θ is the Bragg's angle. The samples were analysed over the range of 20° - 80° at the scanning speed of $0.109^\circ/\text{min}$. XRPD is known to be the most reliable technique in structural characterization (determining crystalline phase and particle size) of the nanomaterials.

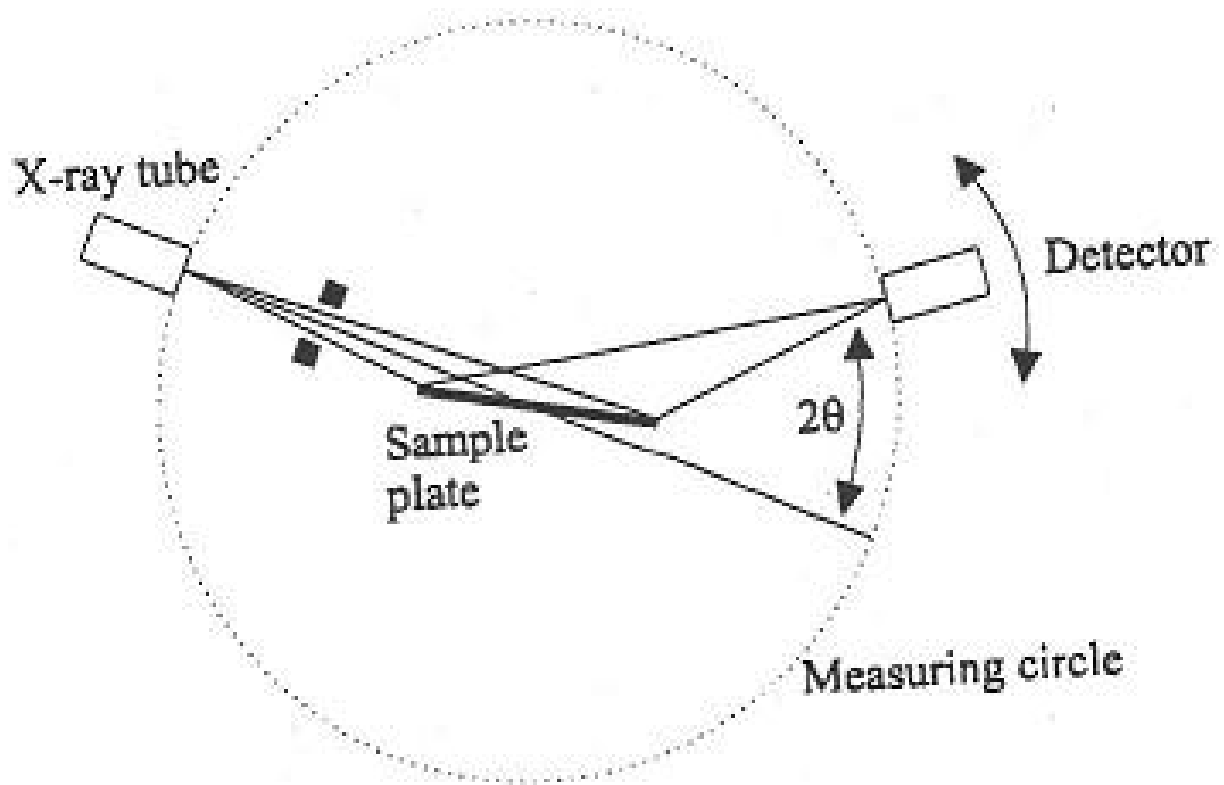


Figure 6.1: The diagram of a usual x-ray powder diffractometer.

6.3.2 Raman Spectroscopy Studies

When light is distributed from a molecule, it is scattered elastically or inelastically. Inelastic scattering is termed Raman scattering. Raman scattering occurs when a photon is incident on a molecule and interacts with the electric dipoles of the molecule. The different sizes of arrows in the figure 6.2 represent the energy differences between the incident and scattered photons. Raman scattering occurs in two forms: Stokes scattering and anti-stokes scattering. Figure 6.2 shows Raman scattering events [171]. Stokes scattering is what is normally seen in Raman spectroscopy. It occurs when the molecule is excited from the ground state (V_0) and results in a molecule at higher energy state (V_1) [172]. Raman anti-stokes scattering can be used when stokes scattering is not observable due to poor detector response to lower frequencies. This takes place when a molecule in an excited state (V_1) gains energy from the incident photon and it is known to be weaker than the stokes scattering but at room temperature it is observed to be strong enough to be useful for vibrational frequencies less than about 1500 cm^{-1} [172]. The equation below is used to calculate, the Raman shift in wavenumber (cm^{-1}) [173]

$$\bar{\nu} = \frac{1}{\lambda_{\text{incident}}} - \frac{1}{\lambda_{\text{scattered}}}, \quad (6.2)$$

where λ is the wavelength (cm) of the incident and Raman scattered photons, respectively. Raman scattering is used to analyse the molecular structure of materials. In the present work, the Raman scattering experiments were carried out using the HORIBA Jobin Yvon T64000 spectrometer housed at the University of Pretoria. The spectrometer was operated in a single spectrograph mode (see figure 6.3) with a holographic filter and fitted with a cooled charge coupled device (CCD) detector. Liquid nitrogen was used to cool the detector. The advantage of using a single monochromator is that there is less loss of light and that one can analyse innumerable samples in a short space of time. The CCD was preferred because it offers rapid analysis of a spectrum and is ideal for most analytical purposes. The Raman spectra were excited using a 514.5 nm line from an argon ion laser. All the experiments were carried out at room temperature. Calibration of the monochromator was done using a silicon sample. This is done after every change of the set-up, such as changing the grating and at the start of every session. The silicon has a Raman peak at 521 cm^{-1} . This peak can be used to correct any changes in the calibration.

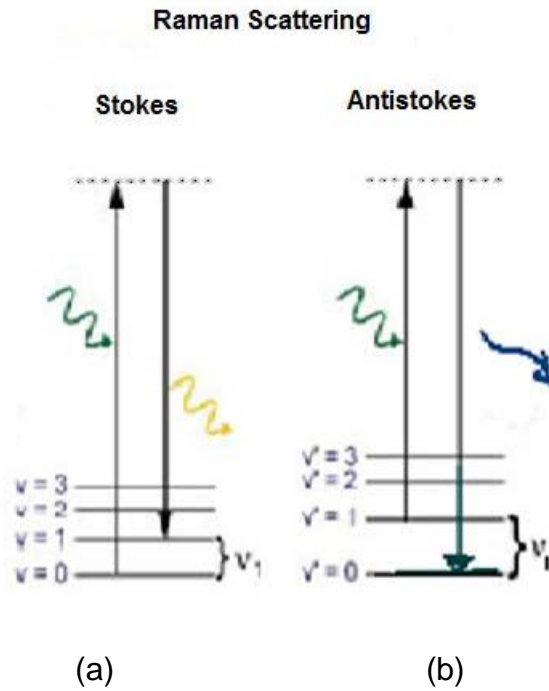


Figure 6.2: Raman events: (a) Stokes scattering (b) Anti-stokes scattering [171].

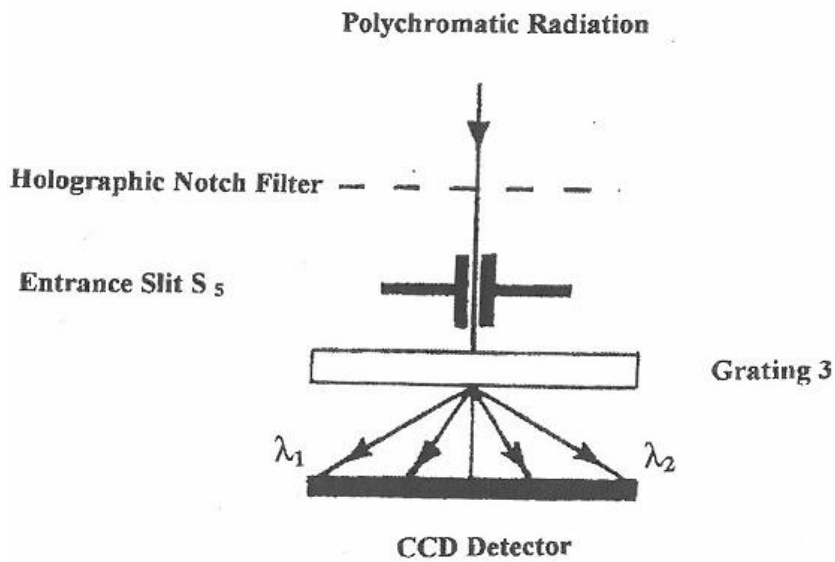


Figure 6.3: The single monochromator (spectrograph) mode. (After the operator manual for the Jobin Yvon model T64000 spectrometer)

6.3.3 Scanning Electron Microscopy (SEM) Studies

Scanning Electron Microscopy (SEM) is a kind of microscope that uses electrons rather than light to form an image [174]. The electrons interact with the atoms of the sample producing signals that contain information about the samples' surface topography, composition and other properties [175]. Magnification can be controlled over a range of up to 6 orders of magnitude from about 19x to 300,000x [175]. The samples to be scanned have to be electrically conductive, otherwise they would be overcharged with electrons during radiation. The electrons in SEM are accelerated at voltages in the range of 2 to 40 kV. A typical diagram of a scanning electron microscope is shown in figure 6.4 [176]. In this section the analysis of Al/Y co-doped SnO₂ nanomaterial for as-prepared and those annealed at various temperatures were performed using the Auriga cobra fib emission scanning electron microscope housed at the Council for Scientific and Industrial Research (CSIR). Samples were coated with carbon before characterization to prevent them from charging. The morphologies of the materials were characterized using SEM at an incrementing voltage of 2 kV. The samples were analysed under the voltage of 2 kV, because it is the maximum voltage which they can withstand, otherwise the samples would burn.

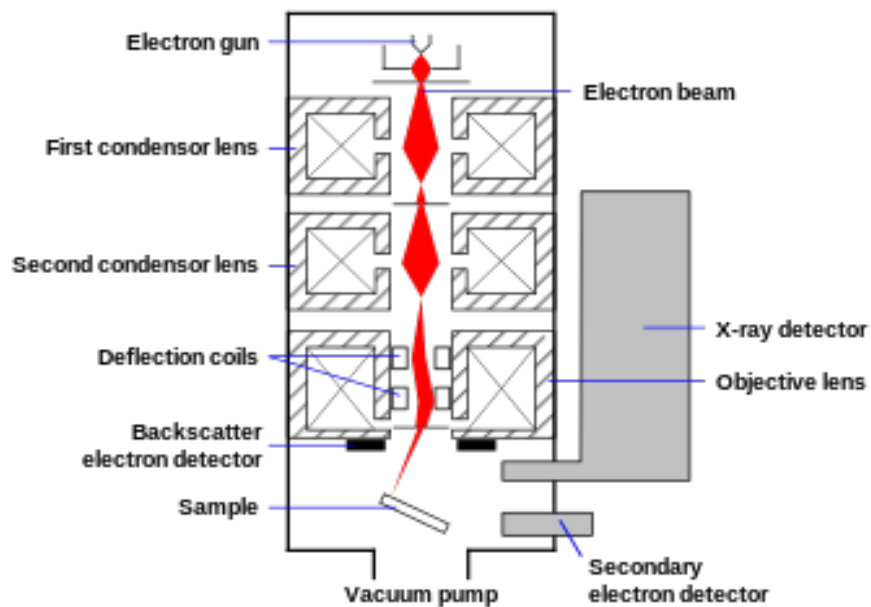


Figure 6.4: A diagram of typical SEM [176].

6.3.4 UV –vis Spectroscopy Studies

UV-vis spectroscopy is a type of instrument that uses light in the UV (200-400 nm) and visible (400-800 nm) range of electromagnetic radiation to investigate the interaction of light radiation and matter [177]. In this range of electromagnetic radiation the molecules undergo electron transition. In many cases the analysis is carried out in solution but solids and gases may also be studied. Table 6.1 shows the range of the electromagnetic radiation utilized in UV-vis spectroscopy.

Table 6.1: Electromagnetic radiation used in the UV-vis spectroscopy [177].

Radiation	nm	Å	cm ⁻¹
	Vis	400-750	4000-7500
Near Uv	200-400	2000-4000	50 000- 25 000
Far Uv	< 200	<2000	>50 000

This technique is known to be useful in analysing the absorption, transmission and reflectivity of different compounds and technologically important materials [178]. The Beer-Lambert law is often used to determine the concentration of an absorbing species in solution, using the equation [178]

$$A = \log_{10} \left(\frac{I_0}{I} \right) = \epsilon \cdot c \cdot l, \quad (6.3)$$

where A is the measured absorbance, in absorbance units (a. u), I_0 is the intensity of the incident light at a given wavelength. I is the transmitted intensity, l is the path length through the sample and c is concentration of the absorber spaces, ϵ is a constant known as molar absorptivity or extinction coefficient. Using Beer-Lambert law there is accepted theory that must be met experimentally for it to apply otherwise there is a possibility of deviation from the law to observant [179]. For example, the chemical makeup and physical environment of the sample can change the extinction coefficient. The chemical and physical condition of a test sample therefore must be in line with the reference measurement for conclusions to be valid. Figure 6.5 shows the diagram of the components of a typical UV-vis spectroscopy sketch.

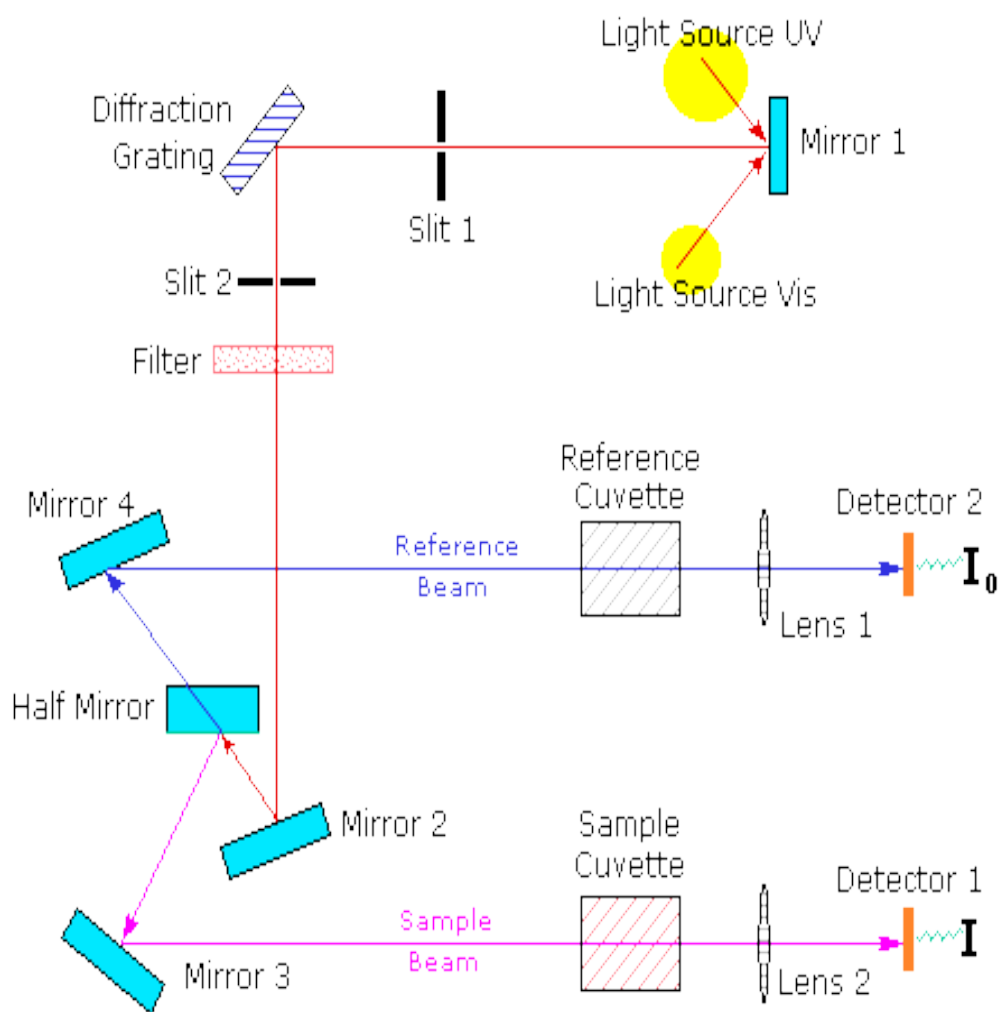


Figure 6.5: A typical sketch of UV-vis spectroscopy [178].

6.4. Experimental Results

6.4.1 XRD Results

The characterisation of sol gel prepared undoped tin dioxide nanoparticles has been previously reported (Zhang et al., [180], Sarmah et al., [181] and Bagheri-Mohagheghi et al., [182]). The patterns were indexed to the tetragonal cassiterite rutile structure of tin oxide with lattice parameters of $a = b = 4.745 \text{ \AA}$ and $c = 3.1293 \text{ \AA}$. It is now well established that SnO_2 has diffraction peaks at $2\theta = (26.58^\circ), (33.76^\circ), (37.79^\circ), (51.72^\circ), (54.318^\circ), (57.88^\circ)$ and (61.891°) , associated with the following planes (110), (101), (200), (211), (220), (002) and (310), respectively as can be seen in the figure 6.6 by Arham et al., [46].

In the present work, focus is on the characterisation of Al/Y co-doped SnO_2 nanoparticle. The XRD profile of the as prepared Al/Y co-doped SnO_2 is shown in figure 6.7. The peaks at $2\theta = 26^\circ, 34^\circ, 54^\circ$ and 65° are associated with the tetragonal cassiterite SnO_2 structure. This is consistent with the values in the standard card (JCPDS 77-0452). The peaks are broad, showing that grain sizes are very small and the Debye-Scherrer equation yields the average particle sizes of 2-3 nm. Only the peaks of SnO_2 are clearly visible. Figure 6.8 shows the XRD profiles for Al/Y co-doped SnO_2 at different temperatures. At 200°C only peaks at $2\theta = 26^\circ, 34^\circ, 54^\circ$ and 65° associated with SnO_2 are observed. The profile is similar to the as prepared one. At 400°C , the XRD profile peaks shows more SnO_2 peaks i.e. those observed at 200°C as well as the new ones at $2\theta = 38^\circ$ and 62° . The peaks are narrower as compared to those of the as prepared sample and the one heated at 200°C .

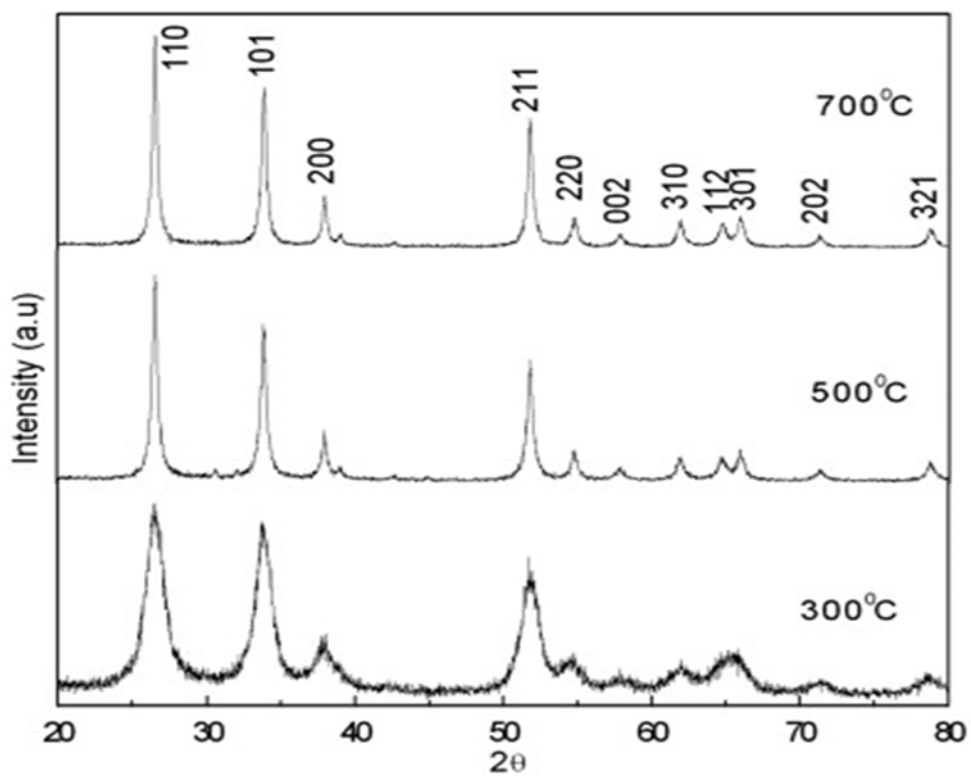


Figure 6.6: XRD patterns of SnO₂ nanoparticles sintered at different temperatures [46].

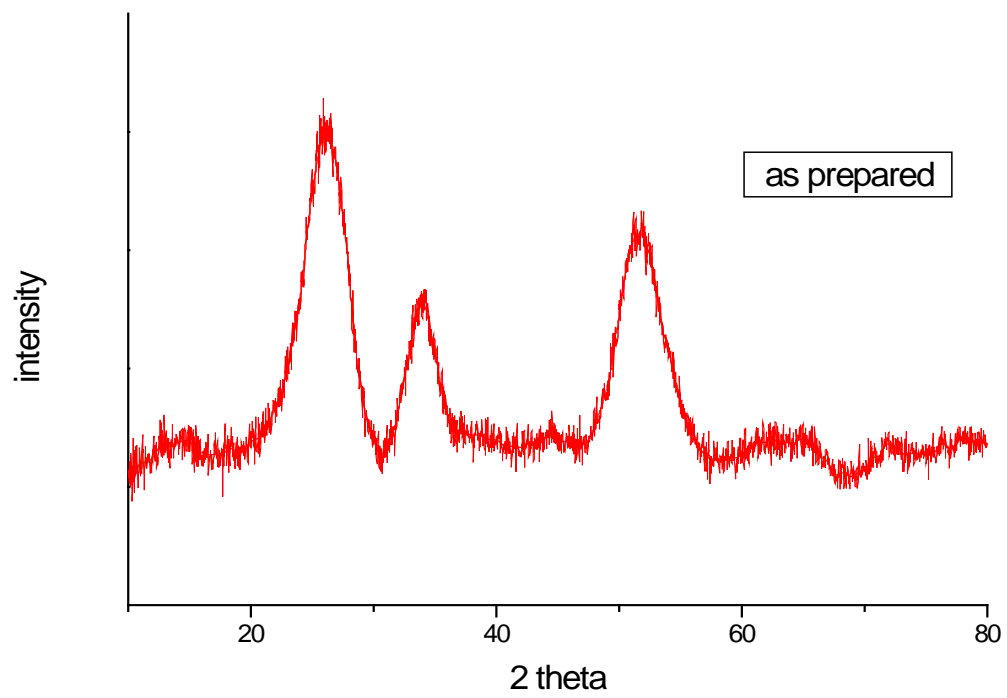


Figure 6.7: The XRD profile of the as prepared Y/Al co-doped SnO₂.

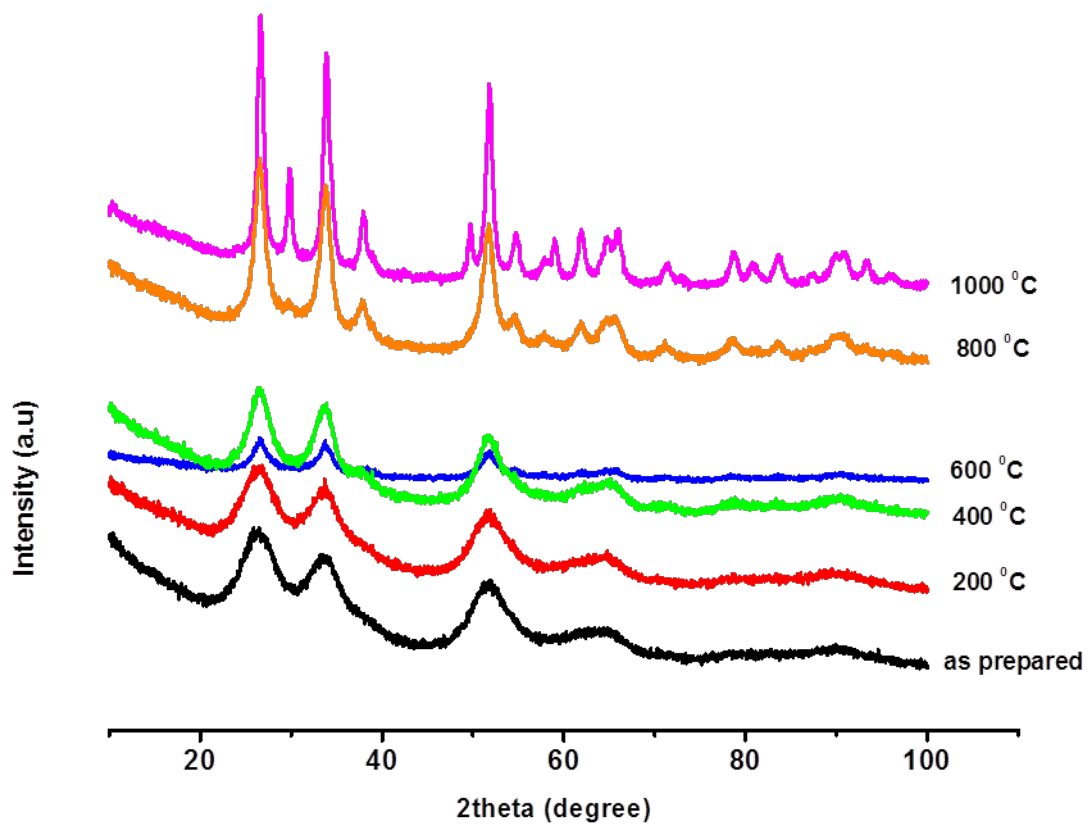


Figure 6.8: XRD profiles for tin oxide Y/Al co-doped SnO₂ at different temperatures.

The results show that there is a decrease in the full width at half maximum (FWHM) of the peaks as the temperature increases i.e. the FWHM of the SnO₂ peaks are inversely proportional to the grain size. This indicates that there is a grain growth as the temperature rises. This behaviour has been displayed also by the undoped sample as can be seen in figure 6.6. As the temperature rises more peaks associated with SnO₂ become evident indicating the improvement in crystallinity. The results show no peaks associated with impurities or additional phases for all samples below 600 °C. At 800 °C there is a development of new peaks at 2θ = 30° and 58° and at 1000 °C the new peaks are intense. These new peaks are associated with yttrium stannate (Y₂Sn₂O₇) phase [89, 183, 184]. This means that at higher temperatures tin dioxide reacts with yttrium to form yttrium stannate. At 1000 °C, the sample is composed of SnO₂ and yttrium stannate.

SnO₂ singly doped with Y has been investigated using extended x-ray absorption fine structures (EXAFS) [1] in the temperature range 200-1000 °C. The fourier transforms (ft's) of the EXAFS spectra for all the samples, except the one annealed at 1000 °C displayed a clear evidence for only one shell around 2.3 Å associated with the Y-O correlation. The lack of a second peak (shell) in the EXAFS spectra is interpreted as the evidence that the Y has not entered the SnO₂ lattice. From the results it was concluded that samples consist of nanocrystals of SnO₂ with Y in the surface layers. The spectrum for the sample annealed at 1000 °C showed an excellent fit to the crystallographic data for Y₂Sn₂O₇ [89, 183, 184] resulting from a high temperature solid-state reaction. This is consistent with what was found in the present co-doped Al/Y doped SnO₂. The effect of Al doping in SnO₂ has been investigated by various researchers in the past [20, 92, 185, 186]. Like with the present co-doped sample, no peaks associated with Al metal or alumina were found. This clearly shows that Al substitutes Sn in the SnO₂. Also there were no changes in the peak positions of the XRD indicating that there was no alloying. The experimental lattice parameters, strain and grain size of Al/Y co-doped SnO₂ nanoparticles are shown in Table 6.2. The lattice parameters for the pure SnO₂ sample are included for comparison purposes. The lattice parameters were calculated using the following relations

$$d_{hkl} = \frac{\lambda}{2\sin\theta}, \quad (6.4)$$

$$\frac{1}{d_{hkl}^2} = \frac{h^2}{a^2} + \frac{k^2}{b^2} + \frac{l^2}{c^2} , \quad (6.5)$$

where d is lattice spacing, $a = b \neq c$ are lattice parameters and h, k, l are miller indices. The X-ray diffraction peaks of crystal plane $[101]$ at $2\theta = 26.42^\circ$ and $[110]$ at $2\theta = 33.42^\circ$ were used to determine the lattice parameters of the Al/Y co-doped SnO_2 nanoparticles samples. The average particle sizes of the samples were calculated using equation (6.1). From the results, it can be seen that the calculated values show that the size increases faster in the range of $600 - 1000^\circ\text{C}$ compared to as prepared to 400°C . The following equation together with equation 6.1, were used to calculate lattice strain.

$$B(2\theta) = 4\varepsilon \frac{\sin \theta}{\cos \theta} , \quad (6.6)$$

where $B(2\theta)$ is the peaks broadenings, ε is the lattice strain, $\sin \theta$ and $\cos \theta$ are the angles. XRD patterns for the samples heated at different temperatures do not show significant peak shifts. This indicates the presence of microstrain rather than macro-strain. As seen from table 6.2, the microstrain is higher for the sample prepared at low temperature and decreases as the temperature rises indicating that the broadening is due to grain size.

Table 6.2: Lattice parameters of pure [181] and calculated lattice parameters, strain and grain size Al/Y co-doped SnO_2 annealed at different temperatures.

Sample	Temperature ($^\circ\text{C}$)	Strain	Grain size nm	Lattice parameters (\AA)		
				a	b	c
Pure SnO_2 [181]	ambient	-	-	4.745	4.745	3.193
Al/Y- SnO_2	100	2.762	2.4	4.830	4.830	3.239
	200	2.5669	2.6	4.810	4.810	3.158
	400	1.6544	3.2	4.810	4.810	3.198
	600	1.76304	4.5	4.747	4.747	3.080
	800	0.86998	6.0	4.747	4.747	3.065
	1000	0.52668	8.0	4.706	4.706	3.012

As seen in table 6.2, the addition of dopants caused no significant change in the lattice parameters confirming that Y (with a larger ionic radius than the host ion) has not entered in the matrix. Introduction of the heat also did not cause the lattice parameter to change that much.

6.4.2 Raman Results

Raman scattering (RS) as well as Infra-red (IR) vibration modes are sensitive to the fluctuations in the crystal and the local arrangements of atoms. The single crystalline SnO₂ belongs to space group D_{4h}^{14} and has six atoms per unit cell. It has 18 vibrational modes in the Brillouin zone ($3n$ modes and, $n = 6$), of which 2 are IR active (the single A_{2u} and the triply degenerate E_u), 4 are Raman active (three non-degenerate modes, A_{1g} , B_{1g} , B_{2g} and a doubly degenerate E_g), and 2 are silent (A_{2g} and B_{1u}) [31, 32]. The three main Raman bands, A_{1g} (630 cm^{-1}), B_{2g} (774 cm^{-1}) and E_g (472 cm^{-1}) are expected as predicted by group theory [187]. A_{1g} and B_{2g} are related to the expansion and contraction vibration mode of the Sn-O bonds whereas the E_g is associated with vibration of oxygen in the oxygen plan. The Raman spectra of Al/Y co-doped nanocrystalline SnO₂ are shown in figure 6.9. The Raman spectra of the as-prepared sample and the one heated at $200\text{ }^\circ\text{C}$ show a broad Raman band at 572 cm^{-1} and this is ascribed to the amorphous tin(IV)-hydrous oxide. This peak is close to the Raman band observed at 571 cm^{-1} for SnO₂ powder [188] and at 566 cm^{-1} for SnO₂ film [189]. For the sample heated at $400\text{ }^\circ\text{C}$, the band associated with the amorphous phase is still observed but new peaks start to develop at 630 cm^{-1} and 774 cm^{-1} . At $600\text{ }^\circ\text{C}$ the 572 cm^{-1} peak is no longer visible and at $800\text{ }^\circ\text{C}$ the three Raman active modes i.e. A_{1g} , B_{2g} and E_g are observed although only the A_{1g} band is clearly visible due the particle size being small. For the sample heated at $1000\text{ }^\circ\text{C}$, all the three bands are clearly visible with the A_{1g} being the most intense. In addition to those associated with SnO₂, more bands at 508 cm^{-1} , 412 cm^{-1} and 311 cm^{-1} are observed. These bands resemble the Raman vibrational modes of yttrium stannate ($Y_2Sn_2O_7$) [190]. These results show that at $1000\text{ }^\circ\text{C}$, SnO₂ reacts with yttrium (Y) to form $Y_2Sn_2O_7$. There were no Raman peaks associated with aluminium or alumina observed in the spectra. The line width of the Raman peaks decreases with the increase in temperature. These results are consistent with the XRD results.

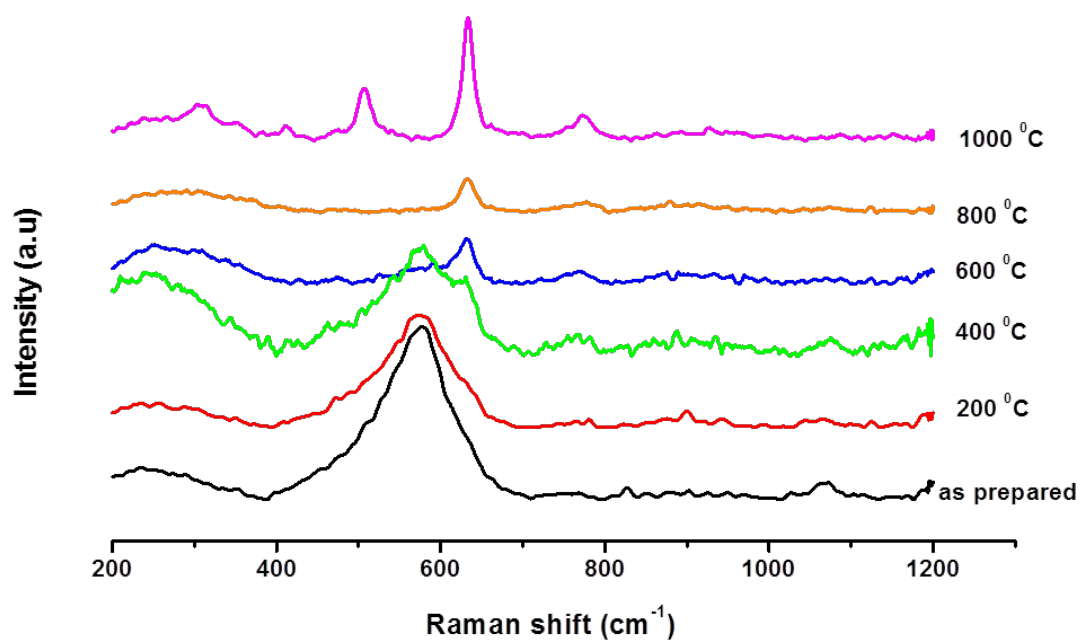


Figure 6.9: Raman shift spectra of Al/Y SnO₂ at different temperatures.

6.4.3 SEM Results

Figures 6.10 (a – c) shows the SEM micrographs for the Al/Y co-doped SnO₂ nanoparticles annealed at different temperatures (200, 600 and 1000 °C). The morphologies of the powders are almost spherical in shape. The micrographs of the as-prepared and of that heated at 200 °C are almost similar and reveal that the powder is amorphous. As the heat treatment temperature increases the amorphous phase decreases and completely disappears at 600 °C (see figure 6.10 (b)), when the crystallinity of the material greatly improves. The 600 °C micrograph also reveals that the particles are agglomerated. Agglomeration could be due to strong hydrogen bonding in the gel network, which is then difficult to remove in the subsequent stages. At very high temperatures, the degree of crystallinity as well as agglomeration further increases considerably. The results are consistent with what is observed using both XRD and Raman in that the low temperature sample contains mostly an amorphous phase and as the temperature increases crystallinity improves.

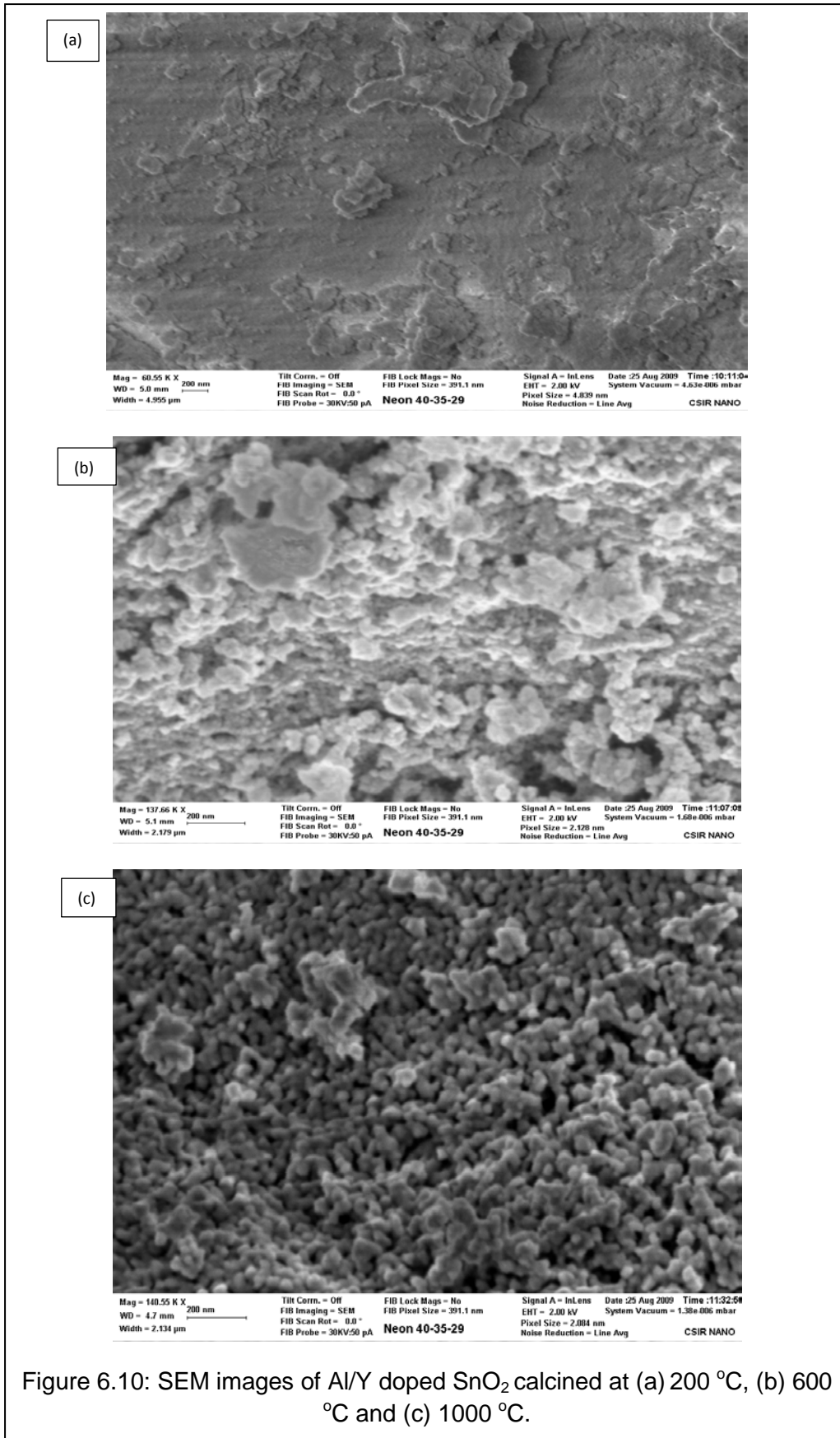
6.4.4 UV-vis Results

6.4.4.1 Optical properties

The optical band gap of nanocrystalline Al/Y co-doped SnO₂ powders were investigated using UV-vis absorption spectroscopy technique at room temperature in the wavelengths ranging from 200–700 nm. The optical band gap (E_g) of the samples was calculated using the following equation [191-193]

$$E = h \cdot C / \lambda, \quad (6.7)$$

where E is the band gap energy, h is the plank constant, C is a speed of light, λ = cut off wavelength. The cut off wavelength is determined by extrapolating the straight line portion of the plot to wavelength axes. The intercept on wavelength axis gives the value of cut-off wavelength. These cut-off wavelengths are associated with the absorption edges. The basic absorption, which associates to electron excitation from the valence band to the conduction band, can be used to calculate the nature and value of the optical band gap [181]. Generally, the nanosized semiconductor particles exhibit three-



shold energy in the optical measurements because of the size-specific band gap structures. These are reflected by the blue shift of the absorption edge as the particle size decreases. Figure 6.11 shows UV-visible absorption spectra of the Al/Y co-doped SnO₂ samples annealed at different temperatures. The absorption edges and the associated optical band gaps of Al/Y co-doped SnO₂ calcined at different temperatures are shown in table 6.3. A number of authors have reported the band gap of pure nanosized SnO₂ to be in the range of 3.5–3.8 eV [6, 194]. The Al/Y co-doped SnO₂ sample calcined at 200 °C exhibits lower band gap energy of 3.31 eV. Similar decreases in the band gap of SnO₂ have been reported for doping with other transition metals like Zn, Mg, Co, and In [195]. The observed decrease in band gap energy can be attributed to the charge-transfer transitions between the dopants and the SnO₂ conduction or valence bands.

Table 6.3: The absorption edges and the associated optical energy band gaps of Al/Y co-doped SnO₂ calcined at different temperatures.

Sample	Temperature (°C)	Wavelength (nm)	Energy band gap (eV)
Bulk SnO ₂ [6]	-	-	3.6
Pure nano SnO ₂ [194]	-	-	(3.5 – 3.8)
Al/Y- SnO ₂	200	375.170	3.31
	400	354.921	3.51
	600	346.124	3.59
	800	328.641	3.79
	1000	311.286	3.99

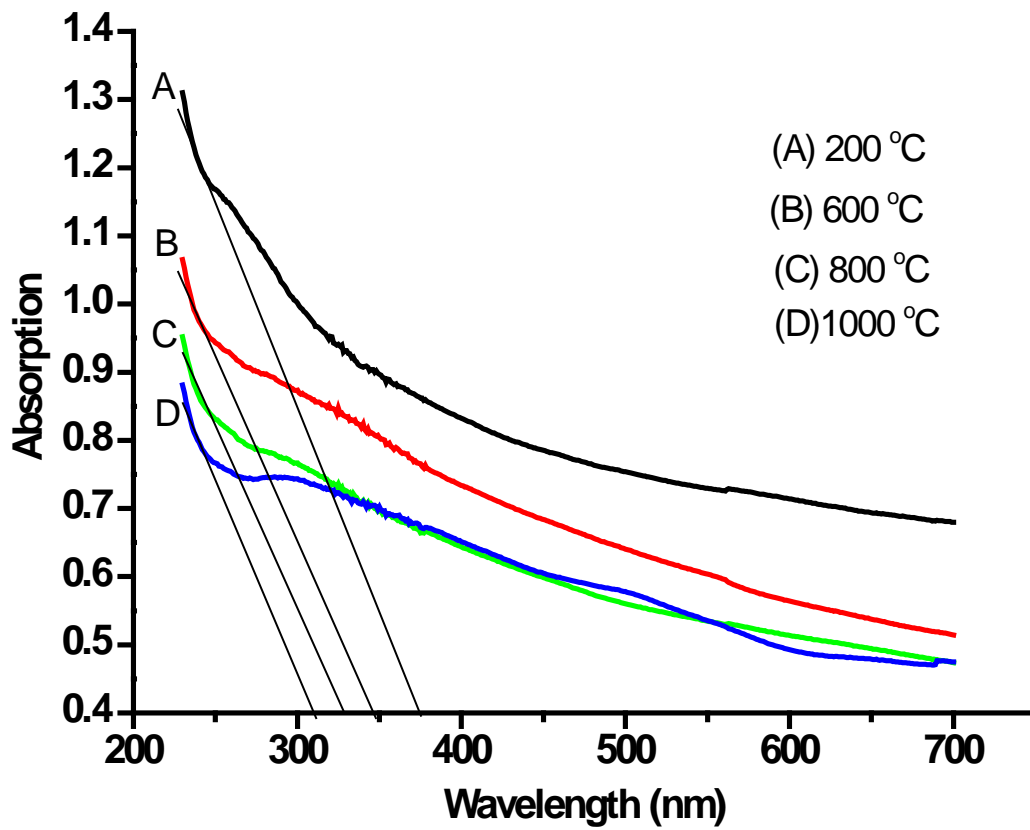


Figure 6.11: Absorption spectra of Al/Y co-doped SnO₂ at different temperatures.

6.5 Conclusion

Nanomaterial Al/Y co-doped SnO₂ were synthesised by sol-gel method. The samples were characterised by XRD, Raman, SEM and UV-vis techniques. The Raman and SEM results show that at lower temperatures there is an amorphous phase although not clearly shown by XRD. Crystallinity is shown to improve with an increase in temperature.

The results reveal that double doping significantly reduces the grain growth of SnO₂. Strain decrease with increase in temperature indicating that peak broadening is due to grain growth. There was no evidence of an Al metal or alumina in the sample indicating that Al may have substituted for Sn atom in the SnO₂. Y is probably on the surface layers. Both XRD and Raman results agree that at high temperatures SnO₂ chemically reacts with Y to form yttrium stannate (Y₂Sn₂O₇).

7. References

- [1] K. E. Rammutla, A. V. Chadwick, J. Harding, D. C. Sayle and R. M. Erasmus, EXAFS and Raman scattering studies of Z and Zr doped nano-crystalline tin oxide, *J. Physics, Conference Series* 249, 012054 (2010).
- [2] M. P. Allen and D. J. Tildesley, *Computer Simulation of Liquids*, Oxford: Clarendon Press, (1989).
- [3] M. Batzill and U. Diebold, The surface and materials science of tin oxide, *Progress in Surface Science* 79, 47-154 (2005).
- [4] V. S. Senthil Srinivasan, M. K. Patra, V. S. Choudhary, M. Mathew and A. Pandya, Phase-change annealing effects on electrical and optical properties of tin oxide thin films, *Journal of optoelectronics and advanced materials* Vol. 12(7), 1485-1489 (2010).
- [5] J. Haines and J. M. Leger, X-ray diffraction study of the phase transitions and structural evolution of tin dioxide at high pressure: Relationships between structure types and implications for other rutile-type dioxides, *Physical Review* B55, 11144(1997).
- [6] W. Fliegel, G. Behr, J. Werner and G. Krabbes, Preparation, development of microstructure, electrical and gas-sensitive properties of pure and doped SnO₂ powders, *Sensors and Actuators B Chemical* Vol.19(1-3), 474-477(1994).
- [7] X. M. Liu, S. L. Wu, P. K. Chu, J. Zheng and S. L. Li, Characteristics of nano Ti-doped SnO₂ powders prepared by sol-gel method, *Material Science and Engineering A* 426, 274-277(2006).
- [8] J. Mizusaki, H. Koinuma, J. I. Shimoyama, M. Kawasaki and K. Fueki, High temperature gravimetric study on nonstoichiometry and oxygen adsorption of SnO₂, *Journal of Solid State Chemistry* Vol. 88, 443-450(1990).
- [9] H. Haitjema and J. Elich, Fluorine-doped tin dioxide films, *Solar Energy Materials* 16, 79-90(1987).

- [10] Y. Li, W. Fan, H. Sun, X. Cheng, P. Li, X. Zhao, J. Hao and M. Jiang, Optical properties of the high pressure phases of SnO₂: First principles calculation, *J. Phys. Chem. A* 114, 1052–1059(2010).
- [11] H. T. Ng, J. Li, M. K. Smith, P. Nguyen, A. Cassell, J. Han and M. Meyyappan, Growth of epitaxial nanowires at the junctions of nanowalls, *Science* 300, 1249(2003).
- [12] S. Shukla, S. Seal, L. Ludwig and C. Parish, Nanocrystalline indium oxide-doped tin oxide thin film as low temperature hydrogen sensor, *Sensors and Actuators B: Chemical* 97(2), 256-265(2004).
- [13] J. Robertson, P.W. Peacock, M. D Towler and R. Needs, Electronic structure of p-type conducting oxides, *Thin Solid Films* 411, 96-100(2002). ISSN 0040-6090
- [14] V. P. Ananikov and I. P. Beletskaya, New approach to stereochemical structure determination of bis-selenium-substituted alkenes, *Rus. Chem. Bull., Int. Ed.*52, 811-816(2003).
- [15] N. T. Miura, T. Raisen, G. Lu and N. Yamazoe, Highly selective CO sensor using stabilized zirconia and a couple of oxide electrodes, *Sens. Actuators B Chem.* 47, 84–91(1998).
- [16] G. Sakai, N.S. Baik, N. Miura and N. Yamazoe, Gas sensing properties of tin oxide thin films fabricated from hydrothermally treated nanoparticles, *Sens. Actuators B* 77, 116(2001).
- [17] G. B. Barbi, J. P. Santos, P. Settini, P.N. Gibson, M.C. Horrillo and L. Manes, Ultrafine grain-size tin-oxide films for carbon monoxide monitoring in urban environments, *Sens. Actuators B* (24–25), 559–563(1995).
- [18] R. Tan, Y. Guo, W. Shen, K. Jiang and W. Song, Surfactant-free hydrothermal synthesis and sensitivity characterization of Pd-doped SnO₂ nanocrystals on multi-walled carbon nanotubes, *Trans. Nonferrous Met. Soc. China.* 21, 568-1573(2011).
- [19] M. Boshta, F. A. Mahmoud and M. H. Sayed, Characterization of sprayed SnO₂: Pd thin films for gas sensing applications, *Journal of Ovonic Research* Vol. 6(2), 93–98(2010).

- [20] R. Padmavathy and D. Sridevi, Influence of s, p, d Block dopant on PEG mediated SnO₂ nanoparticles and nanorods, Archives of Physics Research Vol. 1(4),104-110(2010).
- [21] D. Kohl, The role of noble metals in the chemistry of solid-state gas sensors, Sensors and Actuators B: Chemical Vol. 1(1–6), 158–165(1990).
- [22] N. Yamazoe, Sens. Actuators B 6, 9(1992).
- [23] I. Matko, M. Gaidi, B. Chenevier, A. Charai, W. Saikaly and M. Labeau, Pt doping of SnO₂ thin films a transmission electron microscopy analysis of the porosity evolution, J. Electrochem. Soc. 149, H153(2002).
- [24] V. Brinzari, G. Korotcenkov, V. Golovanov, J. Schwank, V. Lantto and S. Saukko, Morphological rank of nano-scale tin dioxide films deposited by spray pyrolysis from SnCl₄.5H₂O water solution, Thin Solid Film 408, 51-58(2002).
- [25] A. Cabot, J. Arbiol, J. R. Mornate, Y. Weimar, N. Barson and W. Gopel, Analysis of the noble metal catalytic additives introduced by impregnation of as obtained SnO₂ sol-gel nanocrystals for gas sensors, Sens. Actuator B 70, 87-100(2000).
- [26] M. S. Tong, G. R. Dai and D. S. Gao, Gas-sensing properties of PdO-modified SnO₂-Fe₂O₃ double-layer thin-film sensor prepared by PECVD technique, Vacuum 59, 877-884(2000).
- [27] C. A. Papadopoulos and J. N. Avaristsiotis, A model for the gas sensing properties of tin oxide thin films with surface catalysts, Sens. Actuator B 28,201-210(1995).
- [28] E. Comini, A. Vomiero, G. Della Mea and G. Sberveglieri, Influence of iron addition on ethanol and CO sensing properties of tin oxide prepared with RGTO technique, Sens. Actuator B 115, 561-566(2006).
- [29] K. L. Chopra, S. Major and D. K. Pandya, Transparent Conductors - A Status Review, Thin Solid Films 102, 1 - 46(1983).
- [30] C. Kilic and A. Zunger, Origins of coexistence of conductivity and transparency in SnO₂, J. Phys. Rev. Lett. Vol. 88(9), 095501(2002).

- [31] Z. W. Chen, J. K .L. Lai and C. H. Shek, Insights into microstructural evolution from nanocrystalline SnO₂ thin films prepared by pulsed laser deposition, Phys. Rev. B 70,165314(2004).
- [32] A. Dieguez, A. Romano-Rodriguez, A. Vila and J. R. Morante, The complete Raman spectrum of nanometric SnO₂ particles, J. Appl. Phys. 90, 1550(2001).
- [33] T. Arai, The study of the optical properties of conducting tin oxide films and their interpretation in terms of a tentative band scheme, J. Phys. Soc. Jpn. 15, 916 (1960).
- [34] M. P. Singh, P. S. Chandi and R. C. Singh, Synthesis of nano-crystalline tin-oxide powder through fine crystallization in liquid phase, Optoelectronics and advanced materials-Rapid Communications Vol. 1(10), 500-502(2007).
- [35] Z. M. Jarzebsky and J. P. Marton, Physical properties of SnO₂ materials: III. Optical properties, J. Electrochem. Soc. Vol. 123(10), 333-346(1976).
- [36] F. J. Yusta, M. L. Hichman and H. Shamlan, CVD preparation and characterization of tin dioxide films for electrochemical application, J. Mater. Chem. Vol. 7(8), 1421-1427(1997).
- [37] S. R. Dhage, S.P. Gaikwad, V. Sameul and V. Ravi, Synthesis of nanocrystalline SnO₂ powder at 100°C, Bull. Mater. Sci. 27(3), 221-222(2004).
- [38] S. C. Gadkari, V. R. Katti, K. P. Mutthe, A. K. Debnath, A. K. Dua, S. K. Gupta and V. C. Sahni, Asian Journal of Physics 10 (1), 1-7(2003).
- [39] N. N. Greenwood and A. Earnhaw, Chemistry of the Elements, Oxford: Pergamon, 447-448(1984). ISBN 0-08-022057-6.
- [40] G. Zhang and M. liu, Effect of particle size and dopant on properties of SnO₂-based gas sensors, Sensors and Actuators B 69, 144-152(2000).
- [41] E. F. Keskenler, G. Turgut, S. Aydin, R. Dilber and U. Turgut, Investigation of Boron and Yttrium Doping effect on structural, electrical and optical properties of sol-gel spin coated SnO₂ thin films, Journal of Ovonic Research Vol. 9(2), 61-71(2013).

- [42] O. M. Özkendir and Y. Ufuktepe, Electronic and structural properties of SnO and SnO₂ thin films studied by X-ray-absorption spectroscopy, *Journal of optoelectronics and advanced materials* Vol. 9(12), 3729-3733(2007).
- [43] D. J. Goyal, C. Agashe, B. R. Marather, M. G. Takwale and V. G. Bhide, Effect of dopant incorporation on structural and electrical properties of sprayed SnO₂: Sb films, *J. Appl. Phys.* 73, 7520 (1993).
- [44] H. Kim, S. W. Lee, D. W. Shin and C. G. Park, Effect of Antimony Addition on electrical and optical properties of tin oxide film, *J. Amer. Ceramic Soc.* Vol. 77(4), 915-921(1994).
- [45] A. E. Rakhshani, Y. Makdisi and H. A. Ramazaniyan, Electronic and optical properties of fluorine-doped tin oxide films, *J. Appl. Phys.* 23, 1049(1998).
- [46] A. S. Arham, A. Ameer, S. M. Muhamed, M. Chaman and S. Tabassum, Temperature dependent structural and optical properties of tin dioxide nanoparticles, *J. Phys and Chem of Solids* 73, 943-947(2012).
- [47] M. N. Romyantseva, O. V. Safonova, M. N. Boulova, L. I. Ryabova and A. M. Gas'kov, Dopants in nanocrystalline tin dioxide, *Russian Chemical Bulletin, International Edition* Vol. 52(6), 1217-1238(2003).
- [48] S. R. Shieh, A. Kubo, T. S. Duffy, V. B. Prakapenka, and G. Shen, High-pressure phases in SnO₂ to 117 GPa, *Phys. Rev. B* 73, 0141051-0141057(2006).
- [49] L. Gracia, A. Beltrán and J. Andrés, Characterization of the high-pressure structures and phase transformations in SnO₂: A Density Functional Theory Study, *J. Phys. Chem. B* 111 (23), 6479–6485(2007).
- [50] P. Türkes, Ch. Plunkte and R. Heilberg, Thermal conductivity of SnO₂ single crystals, *J. Phys. C: Solid St. Phys* 13, 4941-4951(1980).
- [51] K. N. P. Kumar, D. J. Fray, J. Nair, F. Mizukami and T. Okubo, Enhanced anatase-rutile phase transformation without exaggerated particle growth in nanostructured titania-tin oxide composites, *Scripta Materialia* 57, 771-774(2007).

- [52] C. Agashe, R. B. Marathe, G. M. Takwale and G. V. Bhide, Structural properties of SnO₂: F films deposited by spray pyrolysis technique, Thin Solid Films 164, 261-264(1988).
- [53] C. Sevik and C. Bulutay, High-dielectric constant and wide band gap inverse silver oxide phases of the ordered ternary alloys of SiO₂, GeO₂ and SnO₂, Phys .Rev. B 74, 193-201(2006).
- [54] L. A. Errico, Ab initio FP-LAPW study of the semiconductors SnO and SnO₂ Physica B 389, 140(2007).
- [55] A. Bolzan, C. Fong, B. Kennedy and C. Howard, Structural studies of rutile-type metal dioxides, Acta Crystallogr. B 53, 373(1997).
- [56] M. Dou and C. Persson, Comparative study of rutile and anatase SnO₂ and TiO₂: Band-edge structures, dielectric functions and polar on effects, J. Appl. Phys 113, 083703(2013).
- [57] R. Rai, Study of Structural and electrical properties of pure and Zn-Cu doped SnO₂, Adv. Mat.lett. 1(1), 55-58(2010).
- [58] A. R. Shien, High-pressure phases in SnO₂ to 117 GPa, Physical Review B 73, 014105(2006).
- [59] P. S. Patil, R. K. Kwar, S. B. Sadale and P. S. Chigare, Properties of spray deposited tin oxide thin films derived from tri-*n*butyltin acetate, Thin Solid Films 437, 34(2003).
- [60] C. Agashe and R. C. Aiyer, High-yield synthesis of nanocrystalline tin dioxide by thermal decomposition for use in gas sensors, Int. J. Appl. Ceram. Technol. 5(2), 181(2008).
- [61] B. Hariprakash, A. U. Mane, S. K. Martha, S. A. Gaffoor and S. A. Shivashankar, A low-cost high energy-density lead /acid battery, Electrochemical and Solid-State Letters 7, A66-A69(2004).
- [62] J. Z. Jiang, L. Gerward and J. S. Olsen, Pressure induced phase transformation in nanocrystal SnO₂, Scr. Mater. 44, 1983(2001).

- [63] C. H. Shek, J. K. L. Lai and G. M. Lin, Nanomicrostructure, chemical stability and abnormal transformation in ultrafine particles of oxidized tin, *J. phys. Chem. Solids* 58, 13(1997).
- [64] P. Bai, P. P. Wu, Z. F. Yan and X. S. Zhao, A reverse cation-anion double hydrolysis approach to the synthesis of mesoporous γ -Al₂O₃ with a bimodal pore size distribution, *Micropor. Mesopor. Mater.* 118, 288(2009).
- [65] R. Garro, M. T. Navarro, J. Primo and A. Corma, Lewis acid-containing mesoporous molecular sieves as solid efficient catalysts for solvent-free Mukaiyama-type aldol condensation, *J. Catal.* 233, 342(2005).
- [66] E.R. Leite, I. T. Weber, E. Longo and J. A. Varela, A new method to control particle size and particle size distribution of SnO₂ nanoparticles for gas sensor applications, *Adv. Mater.* 12, 965(2000).
- [67] J. Zhu, B. Y. Tay and J. Ma, Synthesis of mesoporous tin oxide on neutral surfactant templates, *Mater. Lett.* 60, 1003(2006).
- [68] J. Ba, J. Polleux, M. Antonietti and M. Niederberger, Nonaqueous synthesis of tin oxide nanocrystals and their assembly into ordered porous mesostructures, *Adv. Mater.* 17, 2509(2005).
- [69] Y. C. Du, S. liu, Y. L. Zhang, C. Y. Yin, Y. Di and F. S. Xiao, Mesostructured sulfated tin oxide and its high catalytic activity in esterification and friedel–crafts acylation, *Catal. Lett.* Vol. 108(3-4), 155-158(2006).
- [70] L. G. Liu, A fluorite isotype of SnO₂ and a new modification of TiO₂: Implications for the earth's lower mantle, *Science* 199, 422(1978).
- [71] J. Muscat, V. Swamy and N. M. Harrison, First principles calculations of the phase stability of TiO₂, *Phys. Rev. B* 65, 224112(2002).
- [72] P. Serrini, V. Briois, M. C. Horillo, A. Traverse and L. Manes, Chemical-composition and crystalline-structure of SnO₂ thin-films used as gas sensors, *Thin Solid films* 304, 113(1997).

- [73] S. C. Tsang, R. Burch, S. Nishiyama, D. Gleeson, N. A. Cruise, A. Glidle and V. Caps, Nanoscopic tin oxide films on mesoporous silica as novel catalysts for hydrogen transfer reactions, *Nano Structured Materials* 12, 999(1999).
- [74] S. Mishra, C. Ghanshyam, N. Ram, S. Singh, R. P. Bajpai K. K. Bhasin and R. K. Bedi, Effect of calcinations temperature on sensitivity of tin oxide thin film, *Journal of Scientific & Industrial Research* Vol. 62, 1063-1066(2003).
- [75] R. Karshoğlu, A. Alp and H. Akbulut, The effect of substrate temperature on the microstructural properties of nanocrystalline tin oxide coatings produced by APCVD, *J. Coat. Technol. Res.* 7(4), 503-510(2010).
- [76] J. A. Toledo-Antonio, F. Pedraza and X. Bokhimi, The effect of doping low temperature rutile with tin, *Journal of New Materilas for Electrochemical System* 8, 85-90(2005).
- [77] A.V. Bandura, J. O. Sofo and J. D. Kubicki, Derivation of force field parameters for SnO₂-H₂O surface systems from plane-wave Density Functional Theory calculations, *J. Phys. Chem. B* 110, 8386-8397(2006).
- [78] P. Armstrong, C. Knieke, M. Mackovic, G. Frank, A. Hartmaier, M. Göken, and W. Peukert, Microstructural evolution during deformation of tin dioxide nanoparticles in a comminution process, *Acta Materialia* 57, 3060-3071(2009).
- [79] S. Chappel, S. Chan and A. Zaban, TiO₂-coated nanoporous SnO₂ electrodes for dye-synthesized solar cells, *Langmiur* 18, 3336 –3342(2002).
- [80] C. Nayral, E. Viala, V. Colliere, P. Fau, F. Senocq, A. Maisonnat and B. Chaudret, Synthesis and use of novel SnO₂ nanomaterial for gas sensing, *Appl. Surf. Sci.*164, 219-226(2000).
- [81] P. G. Eastwood, T. C. Claypole, J. Watson and G. S. V. Coles, The behaviour of tin dioxide sensors in exhaust environments at low and intermediate temperatures, *Meas. Sci. Technol.* 4, 524-533(1993).

- [82] P. Nunes, E. Fortunato, P. Tonello, F. B. Fernandes, P. Vilarinho and R. Martins, Effect of different dopant element on the properties of ZnO thin films, *Vacuum* 64, 281-285 (2002).
- [83] A. V. Moholkar, S. M. Pawar, K. Y. Rajpure, P. S. Patil and C. H. Bhosale, Properties of highly oriented spray-deposited fluorine-doped tin oxide thin films on glass substrates of different thickness, *Journal of Physics and Chemistry of Solids* 68, 1981(2007).
- [84] A. R. Babar, S. S. Shinde, A. V. Moholkar, C. H. Bhosale, J. H. Kim and K. Y. Rajpure, Structural and optoelectronic properties of antimony incorporated tin oxide thin films, *Journal of Alloys and Compounds* 505(2), 416 (2010).
- [85] A. V. Moholkar, S. M. Pawar, K. Y. Rajpure, S. N. Almari, P. S. Patil and C. H. Bhosale, Solvent-dependent growth of sprayed FTO thin films with mat-like morphology, *Solar Energy Materials and Solar Cells* 92, 1439 (2008).
- [86] Z. Ji, L. Zhao, Z. He, Q. Zhou and C. Chen, Transparent p-type conducting indium-doped SnO₂ thin films deposited by spray pyrolysis, *Materials Letters* 60,1387–1389(2006).
- [87] Z. Ji, Z. He, Y. Song, K. Liu and Z. Z. Ye, Fabrication and characterization of indium-doped p-type SnO₂ thin films, *Journal of Crystal Growth* 259 (3), 282-285 (2003).
- [88] J. Joseph, V. Mathew, and K. E. Abraham, Studies on physical properties and carrier conversion of SnO₂: Nd thin films, *Cryst. Res. Technol.* 41(10), 1020-1026 (2006).
- [89] H. V. Fajardo, E. Longo, L. F. D. Probst, A. Valentini, N. L. V. Carreño, M. R. Nunes, A. P. Maciel and E. R. Leite, Influence of rare earth doping on the structural and catalytic properties of nanostructured tin oxide, *Nanoscale Res Lett.* 3:194-199 (2008).
- [90] H. Zhang, N. Du, B. Chen, T. Cui and D. Yang, Sub-2 nm SnO₂ nanocrystals: A reduction/oxidation chemical reaction synthesis and optical properties, *Mater. Res. Bull.* Vol. 43(11), 3164-3170(2008).

- [91] K. Ravichandran, G. Muruganantham, B. Sakthivel, P. Philominathan, Nano-crystalline doubly doped tin oxide films deposited using a simplified and low-cost spray technique for solar cell applications, *Journal of Ovonic Research* Vol. 5(3), 63-69(2009).
- [92] M. Mageto and M. Mwamburi, The influence of Al doping on optical, electrical and structural properties of transparent and conducting SnO₂: Al thin films prepared by spray pyrolysis technique, *Elixir Chem. Phys.* 53, 11922-11927(2012).
- [93] N. Yamazoe, Y. Kurokawa and T. Seiyama, Effects of additive on semiconductor gas sensor, *Sensors and Actuators* 4, 283(1983).
- [94] Y. Takao, Y. Iwanaga, Y. Shimizu and M. Egashira, Trimethylamine-sensing mechanism of TiO₂-based sensors and effects of metal additives on trimethylamine-sensing properties of TiO₂ sensors, *Sens. Actuators B* 10, 229(1993).
- [95] H. Yamaura, J. Tamaki, K. Moriya, N. Miura and N. Yamazoe, Selective CO detection by using indium oxide-based semiconductor gas sensor, *J. Electrochem. Soc.* 143, L36–L 37(1996).
- [96] R. Botter, T. Aste and D. Beruto, Influence of microstructures on the functional properties of tin oxide-based gas sensors, *Sens. Actuators B* 22, 27–35(1994).
- [97] N. Yamazoe and N. Miura, Some basic aspects of semiconductor gas sensors, in: T. Seiyama Ed., *Chem. Sens. Technol.* Vol. 4, 30(1992), Kodansha, Japan, in cooperation with Elsevier, Amsterdam.
- [98] R. Mukundan, E. Brosha, D. Brown and F. Garzon, Ceria-electrolyte-based mixed potential sensors for the detection of hydrocarbons and carbon monoxide, *Electrochem. Soc. Lett.* 2, 412(1999).
- [99] T. Jinkawa, G. Sakai, J. Tamaki, N. Miura and N. Yamazoe, Relationship between ethanol gas sensitivity and surface catalytic property of tin oxide sensors modified with acidic or basic oxides, *Journal of Molecular catalysis A: Chemical* 155, 193-200(2000).
- [100] F. Lu, Y. Liu, M. Dong and X. Wang, Nanosized tin oxide as the novel material with simultaneous detection towards CO, H₂ and CH₄, *Sensors and Actuators B* 66, 225-227(2000).

- [101] W. Göpel and K. D. Schierbaum, SnO₂ sensors: current status and future prospects, *Sens. Actuators B* 26-27, 1-12(1995).
- [102] J. Calderer, P. Molinàs, J. Sueiras, E. Llobet, X. Vilanova, X. Correig, F. Masana and A. Rodríguez, Synthesis and characterization of metal suboxides for gas sensors, *Microelectron Reliab.* 40, 807- 810(2000).
- [103] I. P. Suzdalev. In: (Nanotechnology: physics and chemistry of nanoclusters, nanostructures and nanomaterial), M. KomKniga, 592(2006).In: Russian.
- [104] N. Kobayashi.In: (Introduction to Nanotechnology). Moscow: Binom, Laboratoria Znani, 134(2005).In: Russian (translated to Japanese).
- [105] V. Lantto, P. Romppainen and S. Leppavuori, A study of the temperature dependence of the barrier energy in porous tin dioxide, *Sens. Actuators* 14, 149-163(1988).
- [106] T. Serin, N. Serin, S. Karadeniz, H. Sari, N. Tuğluoğlu and O. Pakma, Electrical, structural and optical properties of SnO₂ thin films prepared by spray pyrolysis, *Journal of Non-Crystalline Solids* 352, 209-215(2006).
- [107] P. Saikia, A. Borthakur and P. K. Saikia, Structural, optical and electrical properties of tin oxide thin film deposited by APCVD method, *Indian J. Phys.* Vol. 85(4), 551-5589(2011).
- [108] A. A. Yadav, E. U. Masumdar, A. V. Moholkar, M. Neumann-Spallart, K. Y. Rajpure and C. H. Bhosale, Electrical, structural and optical properties of SnO₂: F thin films: Effect of the substrate temperature, *Journal of Alloys and Compounds* 488, 350-355(2009).
- [109] I Mártil and G. González Díaz, Undergraduate laboratory experiment: Measurement of the complex refractive index and the band gap of a thin film semiconductor, *Am. J. Phys.* 60, 83(1992).
- [110] D. Dabajyoti and B. Ratnabali, Properties of electron-beam-evaporated tin oxide films, *Thin Solid Films* 147(3), 321-331(1987).

- [111] M. Fantini and I. Torriani, The compositional and structural properties of sprayed SnO₂:F thin films, *Thin Solid Films* 138(2), 255(1986).
- [112] K. Y. Rajpure, M. N. Kusumade, M. N. Neumann-Spallart and C. H. Bhosale, Effect of Sb doping on properties of conductive spray deposited SnO₂ thin films, *Materials Chemistry and Physics* 64, 184-188(2000).
- [113] J. I. Gittleman, E. K. Sichel and Y. Arie, Composite semiconductors - Selective absorbers of solar energy, *Solar Energy Materials* 1, 93(1979).
- [114] J. Tauc, R. Grigorovici and A. Vancu, Optical properties and electronic structure of amorphous germanium, *Phys Status Solidi (b)* 15, 627-637 (1966).
- [115] W. F. van Gunsteren and H. J. C. Berendsen, Computer Simulation of Molecular Dynamics: Methodology, Applications, and Perspectives in Chemistry, *Angew. Chem. Int. Ed. Engl.* 29, 992-1023(1990).
- [116] M. P. Allen, N. Attig, K. Binder, H.t Grubmüller, K. Kremer (Eds.) and John von Neumann, Introduction to molecular dynamics simulation, Institute for Computing Institute for Computing, Jülich, NIC Series Vol. 23, 1-28(2004). ISBN 3-00-012641-4
- [117] N. Ogbonna and K. Müller-Nedebock, Molecular Dynamics Simulation, African Institute for Mathematical Sciences, Muizenberg, South Africa, May (2004).
- [118] J. Meller, Molecular Dynamics, Cornell University, Ithaca, NewYork, USA Nicholas Copernicus University, Toruń, Poland, (2001).
- [119] G. Sutmann, J. Grotendorst, N. Attig, S. Blugel and D. Marx(Eds.), Molecular dynamics-extending the scale from macroscopic to microscopic. Institute for Advanced Simulation, Forschungszentrum Jülich, NIC Series Vol. 42, 1-49(2009).
- [120] K. Binder and D. W. Heermann, Monte Carlo Simulation in Statistical Physics, Springer, Berlin, (1997).
- [121] D. Frenkel and B. Smit, Understanding molecular simulation from algorithms to applications, Academic Press, San Diego, (1996).
- [122] J. M. Haile, Molecular Dynamics Simulation, Wiley, New York, (1997).

- [123] K. Binder and D. Landau, A Guide to Monte Carlo Simulations in Statistical Physics, Cambridge University Press, Cambridge, (2000).
- [124] A. R. Leach, Molecular Modelling- Principles and Applications, Pearson Education Ltd., Essex, England, (2001).
- [125] T. Schlick, Molecular Modelling and Simulation, Springer, New York, (2002).
- [126] T. Pang, An introduction to computational physics, University of Nevada, Las Vegas, 212(1997).
- [127] http://en.wikipedia.org/wiki/Molecular_dynamics(6/1/2011).
- [128] J. Li and S. Yip(ed), Basic Molecular Dynamics, Handbook of material modelling, 565-588(2005).
- [129] M. Allen and D. Tildesley, Computer simulation of liquids, Clarendon Press, New York, (1987).
- [130] M. Born and K. Huang, Dynamical Theory of Crystal Lattices, 2nd edn., Clarendon Press, Oxford, (1954).
- [131] J. Li, L. Porter, and S. Yip, Atomistic modelling of fine-temperature properties of crystalline beta-SiC-II: Thermal conductivity and effects of point defects, J. Nucl. Mater. 255, 173-177(2003).
- [132] R. Parr and W. Yang, Density-functional Theory of Atoms and Molecules, Clarendon Press, Oxford(1989).
- [133] S. D. Ivanov, A. P. Lyubartsev and A. Laaksonen, Bead-Fourier path integral molecular dynamics, Phys. Rev. E, 67, ART. no. -066710 (2003).
- [134] W. Smith, T. R. Forester and I. T. Todorov, DL_POLY_2 User Manual, STFC Daresbury Laboratory, Daresbury, Warrington WA4 4AD, Cheshire, UK, (2009).
- [135] R. J. Sardus, Molecular Simulation of Fluids: Theory, Algorithms and Object-Oriented, Elsevier, The Netherlands, (1999).

- [136] Y. Liu, N. X. Chen and Y. M. Kang, Virtual lattice technique and the interatomic potentials of zinc-blend-type binary compounds, *Modern Physics Letters B* Vol. 16(5-6), 187-194(2002).
- [137] I. M. Torrens, *Interatomic Potentials*, Academic Press, New York and London, (1972).
- [138] M. Finnis, Interatomic forces in materials, *Progress in Materials Science* 49, 1–18(2004).
- [139] J. J. Cheatum, J. R. Lloyd and Y. W. Kwon, Avalidation of MD simulation in determining the thermal conductivity of LA-ZR PYROCHLORE, 6-7(2008).
- [140] P. S. Ntoahae, P. E Ngoepe and D. G. Petifor, Application of computer simulation method to study of platinum Group minerals, PHD thesis, 148(2005).
- [141] A. R. Al-Derzi, R. L. Johnston, J. N. Murrell and J. A. Rodriguez-Ruiz, Potential energy functions for atomic solids III. Fitting phonon frequencies and elastic constants of diamond structures, *Mol. Phys.* 73, 265-282(1991).
- [142] S. Li, R. L. Johnston and J. N. Murrell, Cluster structures and stabilities from solid-state potentials, Application to silicon clusters, *J. Chem. Soc. Faraday Trans.* 88(9), 1229(1992).
- [143] H. Cox, R. L. Johnston and J. N. Murrell, Empirical potentials for modeling solids, surfaces and clusters, *J. Solid State Chem.* 145 (2), 517-540 (1999).
- [144] A. Chartier, C. Meis, J. P. Crocombete, L. R. Corrales and W. J. Weber, Atomistic Modelling of Displacement Cascades in $\text{La}_2\text{Zr}_2\text{O}_7$ Pyrochlore, *Physical Review B* Vol. 67,1-13(2003).
- [145] U. Diebold, The surface science of titanium dioxide, *Surface Science Reports* 48, 53-229(2003).
- [146] J. F. Wager, Transparent electronics, *Science* 300, 1245-1246 (2003).
- [147] R. E. Presley, C. L. Munsee, C. H. Park, D. Hong, J. F. Wager, and D. A. Keszler, Tin oxide transparent thin-film transistors, *J. Phys. D* 37, 2810-2813(2004).

- [148] F. Alvarez and A. A. Valladares, Atomic topology and radial distribution functions of a-SiNx alloys. Ab initio simulations, arXiv:cond-mat/0110332v1 [cond-mat.mtrl-sci] (2001).
- [149] D. A. Sverjensky, Physical surface complexation models for sorption at the mineral-water interface, *Nature* Vol. 364, 776-780(1993).
- [150] D. T. Cromer and K. Herrington, The structure of anatase and rutile, *J. Am. Chem. Soc.*, Vol. 77, 4708-4709(1955).
- [151] D. Hanaor and C. Sorrell, Review of the anatase to rutile phase transformation, *Journal of Materials science* 46 (4), 855–874(2011).
- [152] R. Hengerer, B. Bollinger, M. Erbudak and M. Grätzel, Structure and stability of the anatase TiO₂ (101) and (001) surfaces. *Surface Science* Vol.460(1-3), 162-169(2000).
- [153] A. Fahmi, C. Minot, B. Silvi and M. Causà, Theoretical analysis of the structures of titanium dioxide crystals, *Phys. Rev. B* 47, 11717-11724(1993).
- [154] J. Oviedo and M. J. Gillan, Reconstructions of strongly reduced SnO₂ (110) studied by first-principles methods, *Surf. Sci.* 513, 26(2002).
- [155] M. Akindeju, V. K. Pareek, A. L. Rohl, D. J. Carter and M. O. Tade, Constant pressure molecular modeling of six optimised titanium oxide polymorphs: metal oxide semiconductors, *International Journal of Chemistry* 2(1), 26-37(2010).
- [156] K. J. Bachmann, F.S.L. Hsu and J. P. Remeika, The low temperature heat capacities of SnO₂ and In₂O₃, *Physica Status Solidi (a)* Vol. 67(1), K39-K42(1981).
- [157] H. Y. Fan and S. A. Reid, Phase transformations in pulsed laser deposited nanocrystalline tin oxide thin films, *Chem. Mater.* 15(2), 564–567(2003).
- [158] L. C. Nehru, V. Swaminathan and C. Sanjeeviraja, Photoluminescence studies on nanocrystalline tin oxide powder for optoelectronic devices, *American Journal of Materials Science* 2(2), 6-10(2012).

- [159] P. Tuerkes, Ch. Pluntke and R. Helbig, Thermal conductivity of SnO₂ single crystals, *Journal of Physics C: Solid St. Phys.* Vol. 13, 4941-4951(1980).
- [160] D. L. Turcotte and G. Schubert, *Geodynamics* (2nd ed.), Cambridge, (2002). ISBN 0-521-66624-4.
- [161] P. S. Peercy and B. Morosin, Pressure and temperature dependences of the Raman-Active phonons in SnO₂, *Phys. Rev. B* 7, 2779–2786(1973).
- [162] I. T. Weber, A. P. Maciel, P. N. Lisboa-filho, E. Longo, E. R. Leite, C. O. Paiva-Santos, Y. Maniette and W. H. Schreiner, Effects of synthesis and processing on supersaturated rare earth-doped nanometric SnO₂ powders, *Nano Lett.* 2 ,970(2002).
- [163] A. Tricoli, M. Righettoni and S. E. Pratsinis, Minimal cross-sensitivity to humidity during ethanol detection by SnO₂–TiO₂ solid solutions, *Nanotechnology* 20, 315 502(2009).
- [164] E. B. Dushanov, K. T. Kholmurodov, K. Yasuoka and E. A. Krasavin, A comparative MD analysis of the structural and diffusion properties of formamide/ water and ethanol/ water Mixtures on TiO₂ and Pt surfaces.(E17-2013-18).
- [165] G. V. Lewis, Computer simulation of the defect structure and PTC properties in BaTiO₃. PHD Thesis, University College, University of London, (1984).
- [166] A. V. Bandura, J. D. Kubicki and J.O. Sofo, Comparisons of multilayer H₂O adsorption onto the (110) surfaces of α-TiO₂ and SnO₂ as calculated with density functional theory, *Journal of Physical Chemistry B* 112 (37), 11616-11624(2008).
- [167] Z. Ji, L. Songlin, D. Fuqi and L. Tonghui, Preparation and microstructure of a nano-sized Ti⁴⁺- doped AgSnO₂ electrical contact material, *Rare Metals*, Vol. 28(1), 19(2009).
- [168] H. V. Fajardo, L. F. D Probst, A. Valentini, N. L. V. Carreño, A. P. Maciel, E. R. Leite and E. Longo, Gas-phase selective conjugate addition of methanol to acetone for methyl vinyl ketone over SnO₂ nanoparticle catalysts. *J. Braz. Chem. Soc.* Vol.16 (3B), 607-613(2005).

- [169] F. E. Ghodsi and H. Absalan, Comparative study of ZnO thin films prepared by different sol-gel route, *Acta Physica Polonica A* 118, 659-664 (2010).
- [170] P. Scherrer, *Göteborgs Berättelse*, 298(1918).
- [171] <http://www.inphotonics.com/technote11.pdf>.
- [172] <http://www.sas.upeun.edu/~crulli/RamanBasics.html>.
- [173] Instructor. physics. isa.umich.edu, Raman Spectroscopy, *Advanced Physics*, 15 (2006).07/12/2013.
- [174] [http://www.mse.iastate.edu/research/laboratories/sem/microscopy/what is the sem/](http://www.mse.iastate.edu/research/laboratories/sem/microscopy/what%20is%20the%20sem/) 8/10/2013.
- [175] <http://emicroscope.blogspot.com/2011/03/scanning-electron-microscope-sem-howt-it.htm>, 2013/08/13.
- [176] http://en.wikipedia.org/wiki/scanning_electron_microscope/2013/08/13.
- [177] <http://www.chem.elte.hu/oktatas/ea/perczel/UV-vis.pdf>/14/10/2013
- [178] <https://www2.chemistry.msu.edu/faculty/reusch/virttxtjml/spectrpy/uv-vis/uvspec.htm> /15/10/2013.
- [179] Mehta, A. Derivation of Beer Lambert law, <http://pharmaxchange.info/press/2012/05/ultraviolet-visible-uv-vis-spectroscopy-limitations-and-deviations-of-beer-lambert-law/>15/10/2013.
- [180] J. Zhang and L. Gao, Synthesis and characterization of nanocrystalline tin oxide by sol-gel method, *Journal of Solid State Chemistry*, Vol. 177(4-5),1425-1430(2004).
- [181] S. Sarmah and A. Kumar, Optical properties of SnO₂ nanoparticles, *Indian J. Phys.* 84(9), 1211-1221(2010).
- [182] M. M. Bagheri-Mohagheghi, N. Shahtahmasebi, M. R. Alinejad, A. Youssefi and M. Shokooch-Saremi, The effect of the post-annealing temperature on the nano-structure and energy band gap of SnO₂ semiconducting oxide nano-particles

synthesized by polymerizing-complexing sol-gel method, *Physica B* 403, 2431-2437(2008).

[183] Z. Lu, J. Wang, Y. Tang and Y. Li, Synthesis and photoluminescence of Eu^{3+} -doped $\text{Y}_2\text{Sn}_2\text{O}_7$ nanocrystals, *Journal of Solid State Chemistry* 177, 3075–3079 (2004).

[184] N. L. V. Carreño, A. P. Maciel, P.N. Lisboa-Filho, E. R. Leite, E. Longo, A. Valentini, L.F.D. Probst, C.O. Paiva-Santos and W. H. Schreiner, The influence of cation segregation on the methanol decomposition on nanostructured SnO_2 , *Sensors and Actuators B* 86, 185-192(2002).

[185] M. Benhaliliba, C. E. Benouis, Y. S. oca and F. Yakuphanoglu, Nanostructured Al doped SnO_2 films grown onto substrate via spray pyrolysis route, *Journal of Nano- and Electronic Physics* Vol. 4 (1), 01011(2012).

[186] R. Alcántara, F. J. Fernández-Madrugal, C. Pérez-Vicente, J. L. Tirado, J. Jean Claude and J. Olivier-Fourcade, Preparation, sintering, and electrochemical properties of tin dioxide and Al- doped tin dioxides obtained from citrate precursors, *Chem. Mater.* 12, 3044-3051(2000).

[187] K. N. Yu, Y. Xiong, Y. Liu and C. Xiong, Microstructural change of nano- SnO_2 grain assemblages with the annealing temperature, *Phys. Rev. B* 55, 2666–2671(1997).

[188] M. Ristić, M. Ivanda, S. Popović and S. Musić, Dependence of nanocrystalline SnO_2 particle size on synthesis route, *Journal of Non-Crystalline Solids* Vol. 303(2), 270–280(2002).

[189] T. Asari and T. Sato, Temperature dependence of raman band of SnO_2 crystal, *J. Phys. Soc. Jpn.* 66, 1360-1363(1997).

[190] K. Li, H. Li, H. Zhanga, R. Yua, H. Wanga and H. Yana, Hydrothermal synthesis of Eu^{3+} -doped $\text{Y}_2\text{Sn}_2\text{O}_7$ nanocrystals, *Materials Research Bulletin* 41, 191–197 (2006).

[191] M. Hoffman, S. Martin, W. Choi and D. Bahnemann, Environmental applications of semiconductor photo catalysis, *Chemical Review* Vol. 95, 69-96(1995).

- [192] J. Wade, An investigation of $\text{TiO}_2\text{-ZnFe}_2\text{O}_4$ Nanocomposites for visible light photo catalysis, A thesis submitted to Department of Electrical Engineering; College of Engineering, University of South Florida, March 24, (2005).
- [193] J. Dharma and A. Pisal, Simple method of measuring the band gap energy value of TiO_2 in the powder form using a UV/Vis/NIR spectrometer, UV/Vis/NIR Spectrometer (2009).www.perkinelmer.com
- [194] R. Summitt, J. A. Marley and N. F. Borrelli, Ultraviolet absorption edge of stannic oxide (SnO_2), J. Phys. and Chem. Solids 25,1465-1469(1964).
- [195] C. Drake and S. Seal, Band gap energy modifications observed in trivalent In substituted nanocrystalline SnO_2 , Appl. Phys. Lett. 90(23), 233117(2007).
- [196] D'Ans-Lax: Taschenbuch für Chemiker und Physiker, Vol. 1, Berlin, Heidelberg, New York: Springer (1967).

8. Publications and conference presentations

8.1 Publications

8.1.1 NJ Ntimane, KE Rammutla and TE Mosuang Effects of Combinational Al and Y Doping on the structural and optical properties of Nanocrystalline SnO₂, Indian Journal of Physics. DOI 10.1007/s12648-014-0633-0,(2014).

8.1.2. JN Ntimane, TE Mosuang and KE Rammutla, Structural and Thermodynamic Properties of Some Defects in SnO₂, Proceedings of the International Conference on Advanced Nanomaterials and Emerging Engineering Technologies (ICANMEET 2013), pp, 295 – 298, ISBN: 978-1-4799-1377-0 IEEE, (2013).

8.1.3. JN Ntimane, TE Mosuang and KE Rammutla, Structural and Thermodynamics properties of point defects in tin-dioxide (SnO₂), SA Institute of Physics, pp.170-174, ISBN:978-1-77592-070-0, (2012).

8.1.4. JN Ntimane, TE Mosuang and KE Rammutla, Computational studies of rutile oxide (SnO₂), SA Institute of Physics, pp. 258 – 261, ISBN: 978-1-86888-688-3, (2011).

8.2 Conference Presentations

8.2.1. JN Ntimane, TE Mosuang and KE Rammutla, Computational study of Ti and Y defects in tin dioxide (SnO₂), India, Brazil and South Africa (IBSA) workshop, St Georges Hotel and Convention Centre, Irene, South Africa, (2013).

8.2.2. JN Ntimane, TE Mosuang and KE Rammutla, (UP), Computational studies of Ti doped SnO₂, The 57th Annual conference of the South African Institute of Physics (UP, RSA, 2012).

8.2.3. JN Ntimane, TE Mosuang and KE Rammutla, Computational studies of rutile oxide (SnO₂), The 56th annual conference of the South African Institute of Physics (UNISA), South Africa, 2011).

8.2.4. JN Ntimane, TE Mosuang and KE Rammutla and Hillie T, XRD Characterisation of SnO₂ doped with both Y and Al, The 55th annual conference of the South African Institute of physics (SAIP), CSIR, Pretoria, (2010).